ADVANCES IN PHYSICS, 1998, VOL. 47, NO. 4, 511–597

Magnetic nanostructures

By F. J. HIMPSEL

Department of Physics, University of Wisconsin Madison
1150 University Avenue, Madison, Wisconsin 53706-1390, USA

J. E. ORTEGA

Departamento de Fisica Aplicada I, Universidad del Pais Vasco,
Escuela de Arquitectura, Plaza de Oñate 2, 20009 San Sebastian, Spain

G. J. MANKEY

Center for Materials for Information Technology, The University of Alabama
Box 870209, Tuscaloosa, Alabama 35487-0209, USA

and R. F. WILLIS

Department of Physics, Penn State University,
University Park, Pennsylvania 16802, USA

[Received 23 September 1996; revised 15 August 1997; accepted 10 September 1997]

Abstract

Magnetic materials have become controllable on the nanometre scale. Such fine structures exhibit a wide range of fascinating phenomena, such as low-dimensional magnetism, induced magnetization in noble metals, electron interference patterns, oscillatory magnetic coupling and 'giant' magnetoresistance. Magnetic multilayers with nanometre spacings are among the first metallic quantum structures to become incorporated into electronic devices, such as reading heads for hard discs. This article is intended to familiarize the reader with the physics and technology of magnetic nanostructures. It starts out with recent progress in nanofabrication, gives a tutorial on the connection between electronic states and magnetic properties, surveys the state of the art in characterization techniques, explains unique phenomena in two-, one- and zero-dimensional structures, points out applications in magnetic storage technology and considers fundamental limits to storage density. Particular emphasis is placed on the connection between magnetism and the underlying electronic states, such as the spin-split energy bands, s, p versus d states, surface states, and quantum well states.

Contents PAGE

0001–8732/98 $12·00

1. Introduction

The advances made during the past decade in the preparation and characterization of thin films and surfaces have brought an intriguing question within reach: is it possible to fabricate 'designer solids' by controlling materials on the atomic scale, that is layer by layer, row by row, and ultimately atom by atom? Engineered molecules are common-place in biochemistry, and the same idea can be brought to bear on solids and electronic materials. Electronic properties of semiconductor devices have been controlled by heterostructures, quantum wells and superlattices. Magnetism as a cooperative phenomenon lends itself to manipulation in small structures, where neighbour atoms can be replaced systematically by species with stronger or weaker magnetism. In fact, a class of magnetic/non-magnetic multilayers termed 'spin valves' has been introduced into magnetic storage devices.

How fine does a solid need to be structured to have an impact on its electronic and magnetic properties? The wavefunction of electrons is going to change when they are confined to dimensions comparable with their wavelength (figure 1). As an estimate we may see the Fermi wavelength of a simple free-electron gas. It decreases with increasing carrier density. Therefore, confinement and quantization phenomena are visible in semiconductors already at dimensions greater than 200 nm (Hansen *et al.* 1992, Kastner 1993), whereas in metals they typically are seen at 1 nm. In fact, the Fermi wavelength of typical metals has atomic dimensions, but beat frequencies with the lattice can be an order of magnitude larger. A related way of reasoning considers the formation of low-dimensional electronic states by quantization. Confining electrons to small structures causes the continuous bulk bands to split up into discrete levels, for example quantum well states in a slab. For N atomic layers in the slab there are N levels. In order to exhibit two-dimensional behaviour there should

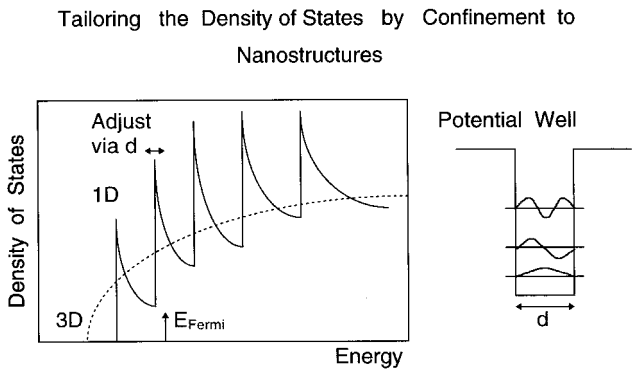

Figure 1. Tailoring electronic properties of materials by nanostructuring. Electrons confined to nanostructures give rise to low-dimensional quantum well states, which modify the density of states. States at the Fermi level trigger electronic phase transitions, such as magnetism and superconductivity (see section 3.2.1). They are also responsible for magnetic coupling and conductivity.

be only a single level within $\pm kT$ of the Fermi level. Several levels within the Fermi cut-off would already approach a three-dimensional continuum. For a coarse estimate of the corresponding slab thickness, one may set the energy E of the lowest level equal to kT. For room temperature ($E = kT = 0.026\,\text{eV}$), one obtains a de Broglie wavelength $\lambda = h/p = h/(2mE)^{1/2} \approx 1.23\,\text{nm}/(E/eV)^{1/2} \approx 8\,\text{nm}$, which is comparable with the spatial extent of the lowest quantum state. Thus, both the high electron density in magnetic metals and the requirement of room-temperature operation for quantum devices point to dimensions of a few nanometres.

This article is intended to provide insight into the phenomena encountered in magnetic structures on the nanometre scale. This fast-moving field was assessed by Falicov *et al.* (1990); major subtopics were addressed by Bader (1990), Gradmann (1991), Shinjo (1991), Siegmann (1992), Heinrich and Cochran (1993), Allenspach (1994) and Prinz and Hathaway (1995). First, we introduce fabrication methods for multilayers, wires, and dots, for example layer-by-layer deposition, step decoration and atom positioning using scanning tunnelling microscopy (STM). Our emphasis will be placed on self-assembly, which produces macroscopic amounts of tailored materials. A survey of characterization techniques for electronic states and magnetic properties follows, particularly those sensitive enough to detect nanostructures. The central part of the article discusses the electronic and magnetic phenomena encountered on the nanometre scale. It starts in three dimensions with metastable epitaxial structures, goes on to two-dimensional surfaces, monolayers and quantum wells, from there to one-dimensional wires and ends up at zero-dimensional particles. Thereby we stress the connections between magnetic properties and the underlying electronic states. The last section branches out into applications of atomically engineered structures in magnetic storage. The physical limits of storage density are considered and an outlook onto the opportunities for tailored magnetic devices is given.

2. Fabrication of nanostructures

This section gives an overview of growth techniques and *in-situ* growth control. Thereby we proceed towards lower dimensionality from multilayers to monolayers, stripes and dots. While most of the methods discussed here are common to many

materials, there is a feature special to ferromagnets; growing a film in the presence of a magnetic field affects the magnetic domain structure, which is critical to many devices. For example, dramatic improvements have been observed in magnetic tunnel junctions, such as a 40 times lower switching field combined with a 30 times sharper transition (Moodera and Kinder 1996). Likewise, the pinning of a magnetic layer by an adjacent antiferromagnetic FeMn layer is obtained by growing in a magnetic field (exchange biasing; see section 8.2). Depositing a permalloy film in a magnetic field produces an easy axis for magnetoresistive sensors (White 1984).

2.1. *Equilibrium growth*

For growing magnetic layers with monolayer control it is important to realize the forces that rearrange the growing surface. A dominant role is played by the *free energies* γ of the surface and interface. They determine the growth modes in thermal equilibrium, which are shown in figure 1. The morphology of material B grown on material A depends on the balance between the free surface energies of substrate, overlayer and interface (Bauer 1958). If

$$\gamma_{\text{substrate}} > \gamma_{\text{overlayer}} + \gamma_{\text{interface}}, \tag{1}$$

the first atomic layer wants to coat the whole surface to provide optimum energy reduction. For subsequent layers the situation has changed; the surface energy of their substrate has already been reduced by the first layer and they do not experience the same interface energy. In addition, they have to absorb the misfit strain energy, which grows with increasing film thickness. Therefore, a continued layer-by-layer mode is rare, and the more common mode is the formation of islands on top of a flat first layer (Stranski–Krastanov growth). For example, Cu on bcc Fe(100) breaks up into large islands after first wetting the surface. This mode leaves as much as possible of the energetically favourable first layer exposed and reduces strain because the islands are able to relax laterally. If the energy balance at the interface is tipped the opposite way, that is for

$$\gamma_{\text{substrate}} < \gamma_{\text{overlayer}} + \gamma_{\text{interface}} \tag{2}$$

the overlayer has a tendency to nucleate three-dimensional islands right away, and leave the low-energy substrate exposed. This situation generally occurs when growing magnetic materials on top of an inert substrate, such as a noble metal or an oxide. If the substrate atoms are mobile enough, they tend to trade places with the deposited magnetic atoms, which blurs the interface.

Magnetic materials exhibit a relatively *high surface energy* (table 1), owing to their partially filled d shell. Noble metal substrates have smaller surface energies, and insulating substrates even less (table 1). They provide tight capping layers for ferromagnetic layer structures but make it difficult to deposit smooth ferromagnetic layers on top. In general, one faces Murphy's law of epitaxy when growing multilayers of two materials A and B with substantial surface energy difference; if A grows on B layer by layer, then B on A will grow in islands, since the surface energies are reversed. To overcome this problem, one has to resort to non-equilibrium growth at low temperatures. A brief anneal recrystallizes the film before surface diffusion begins and islands are formed. This technique has been used to obtain smooth films by suppressing Stranski–Krastanov growth. An example is the deposition of smooth Gd films on W at room temperature with a 530 K post-anneal (Farle *et al.* 1993, Tober *et al.* 1996). For reactive materials, such as rare earths and early transition metals, such epitaxial films have better surfaces than single crystals.

Table 1. Surface energies γ for magnetic and non-magnetic materials, listed with respect to their atomic number (for metals see Mezey and Giber (1982) (compare also Miedema and Dorleijn (1980), Miedema *et al.* (1980) and Tyson and Miller (1977); for semiconductors and insulators see Jaccodine (1963), Gilman (1960), Messmer and Bilello (1981) and Cook (19086); all these are for the low-energy cleavage surface). Note that these are approximate values, which are difficult to measure and dependent on surface orientation and reconstruction.

Magnetic metal	Cr	Mn	Fe	Co	Ni	Gd				
γ ($J\,m^{-2}$)	2.1	1.4	2.9	2.7	2.5	0.9				
Transition metal	Ti	V	Nb	Mo	Ru	Rh	Pd	Ta	W	Pt
γ($J\,m^{-2}$)	2.6	2.9	3.0	2.9	3.4	2.8	2.0	3.0	3.5	2.7
Simple or Noble metal	Al		Cu		Ag		Au			
γ($J\,m^{-2}$)	1.1		1.9		1.3		1.6			
Semiconductor	Diamond		Si		Ge		GaP		GaAs	
γ($J\,m^{-2}$)	1.7		1.2		1.1		1.9		0.9	
Insulator	LiF		NaCl		CaF_2		MgO		Al_2O_3	
γ($J\,m^{-2}$)	0.34		0.3		0.45		1.2		1.4	

This method is applicable to noble metals, too. The smoothest Cu–Co(100) interfaces are obtained that way (Segovia *et al.* 1996, Würsch *et al.* 1997), and atomically flat Ag films have been grown on GaAs in this fashion (Evans *et al.* 1993, Smith *et al.* 1996).

Smooth growth can be promoted by a *surfactant*, that is a coating that floats on top of the growing film without being incorporated into it. Surfactants promote layer-by-layer growth in a variety of ways. Lowering the surface energy is the most obvious, but there are other possibilities, such as lowering of the barrier for diffusion of adatoms down from islands (van der Vegt *et al.* 1992) (see also figure 6 in section 2.4) and introducing a high density of nuclei for growing monolayer islands (Kunkel *et al.* 1990, Rosenfeld *et al.* 1993, Tersoff *et al.* 1994). Several boundary conditions are imposed on a surfactant, for example low surface energy, high mobility and little reactivity with the growing film. Therefore, only a few surfactants are known for use with the highly reactive ferromagnets, for example O, N, CO for Fe (Steigerwald *et al.* 1988), CO for Fe (Wuttig *et al.* 1993a), Au for Fe (Bader and Moog 1987, Himpsel 1991a) and Pb for Co (Camarero *et al.* 1996, Egelhoff *et al.* 1996). Cu and Ag exhibit low surface energy and little miscibility with ferromagnets, for example equilibrium concentrations of less than 1% in Fe and Co and vice versa.

The *interface energy* comes into play when two materials are highly miscible (Massalski 1992). Cr forms alloys with Fe, leading to a strong tendency for Cr to be incorporated into Fe near the interface (Davies *et al.* 1996). The growth of Fe/Cr layers is dominated by the strongly attractive interface energy.

In many metal-on-metal systems, one finds that the first few atomic layers are growing layer by layer but eventually break up into islands owing to *misfit strain*. Strain grows with increasing film thickness and leads to the sudden formation of misfit dislocations at a critical thickness that depends mainly on the lattice mismatch. For a 1–2% mismatch it takes 10 nm or more for this break-up to occur, and for 4–6% mismatch only a couple of atomic layers. Therefore, one is always looking out for lattice-matched materials combinations in order to produce perfect epitaxial

Table 2. Lattice-matched combinations of magnetic materials, substrates and spacer layers. There are two main groups of lattice-matched systems with lattice constants close to 4.0 or 3.6 Å respectively, after taking 45° rotations of the lattice or doubling of the lattice constant into account (compare Prinz 1991).

First group:					
Magnetic metal	Cr (bcc)	Fe (bcc)	Co (bcc)		
$2^{1/2}a$ [Å] (a [Å])	4.07 (2.88)	4.05 (2.87)	3.99 (2.82)		
Simple or noble metal	Al	Ag	Au		
a [Å]	4.05	4.09	4.07		
Semiconductor	Ge	GaAs	ZnSe		
$a/2^{1/2}$ [Å] (a [Å])	3.99 (5.65)	4.00 (5.65)	4.01 (5.67)		
Insulator	LiF	NaCl	MgO		
a [Å] $a/2^{1/2}$ [Å]	4.02 (2.84)	3.99 5.65	4.20 (2.97)		
Second group:					
Material	Fe (fcc)	Co (fcc)	Ni (fcc)	Cu	Diamond
a [Å]	3.59	3.55	3.52	3.61	3.57

films. As shown in table 2, there are two principal groups of lattice-matched materials, one containing bcc Fe, Cr(100), fcc Ag, Au(100), Ge and GaAs(100), and the other based on fcc Fe, Co, Ni and Cu. For some of these materials the match is not 1:1 but $2^{1/2}$:1 which makes it possible to obtain atom-on-atom registry between a fcc(100) surface and a bcc(100) surface that has $2^{1/2}$ smaller lattice constant and is rotated azimuthally by 45°. A more detailed account of the growth modes under the influence of surface energy, lattice mismatch and supersaturation has been given by Bauer and van der Merwe (1986).

2.2. *Non-equilibrium growth*

The thermodynamic laws of film growth are too restrictive for growing the desired variety of magnetic structures. Most of the interesting structures do not occur naturally, and will disintegrate when annealed to temperatures higher than about 200° C. Interfaces become washed out by interdiffusion, surfaces of magnetic layers become coated with noble metal atoms diffusing out from the substrate, continuous films break up into platelets, and metastable phases such as fcc Fe and fcc Co convert to their stable counterparts bcc Fe and hcp Co. A skilled film grower has a variety of non-equilibrium tricks in his bag, and more are being discovered continuously. This is an area where science and art meet.

As a consequence, non-equilibrium growth methods have to be considered which operate at reduced temperature or increased deposition rate. In this growth regime, surface steps are starting to play a dominant role (Burton *et al.* 1951). Figure 2 shows what happens when entering non-equilibrium growth.

At *high temperatures* the adsorbed atoms diffuse to the nearest step, where they find the bonding site with the highest coordination and become incorporated. This is the *step-flow* growth mode.

At *reduced temperatures*, or higher rates, or lower step densities, the arriving atoms do not have enough time to find the nearest step edge and nucleate spontaneously into islands. These islands grow by incorporating atoms that arrive nearby and eventually coalesce into a smooth monolayer. This is a popular growth

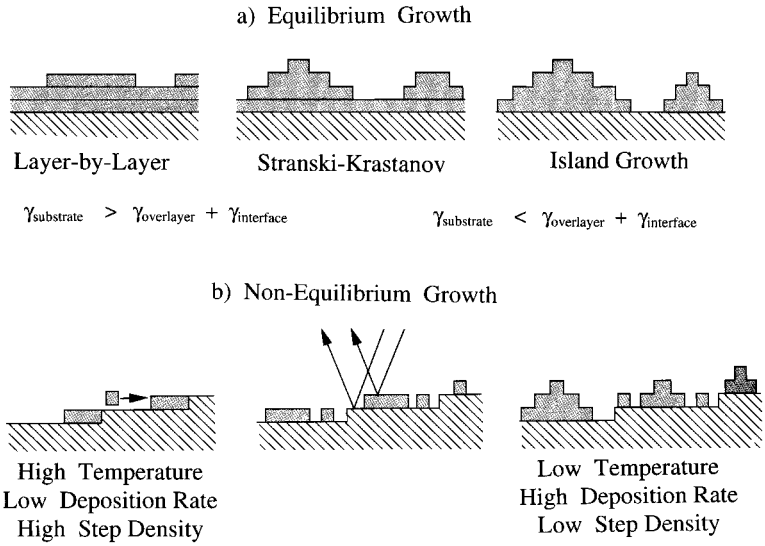

Figure 2. (a) Equilibrium growth modes for different surface and interface free energies of substrate and overlayer. Lattice mismatch is neglected in this picture. (b) Non-equilibrium growth modes at low substrate temperature and high evaporation rate.

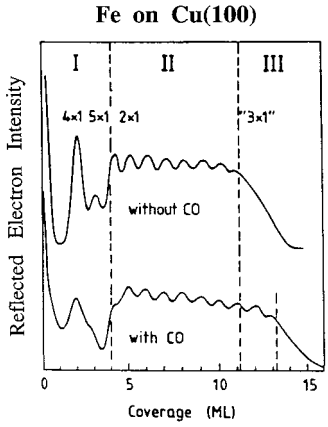

Figure 3. Oscillations in the intensity of a reflected electron beam in reflection high-energy electron diffraction (RHEED). They can be used to calibrate the coverage in monolayers (compare figure 2b, centre, for the mechanism) (Wuttig *et al.* 1993a).

mode, since it makes it easy to count the growing monolayers one by one. The periodic change in surface roughness from smooth at integer-monolayer coverage to rough at half-integer-monolayer coverage gives rise to *oscillations in the diffraction intensity* for electrons, ions and X-rays (Egelhoff and Jacob 1989, Kunkel *et al.* 1990, van der Vegt *et al.*, Henzler 1993). The effect can be enhanced by going to the out-of-phase condition, where the beam reflected from the upper terrace interferes destructively with that from the lower terrace. Ideally, they cancel out to zero at half-integer coverage. Figure 3 gives an example of the epitaxy of Fe on Cu(100) (Wuttig *et al.* 1993a). By following the amplitude of the oscillations, one finds a complex growth behaviour with two abrupt changes at four and 11 monolayers. The

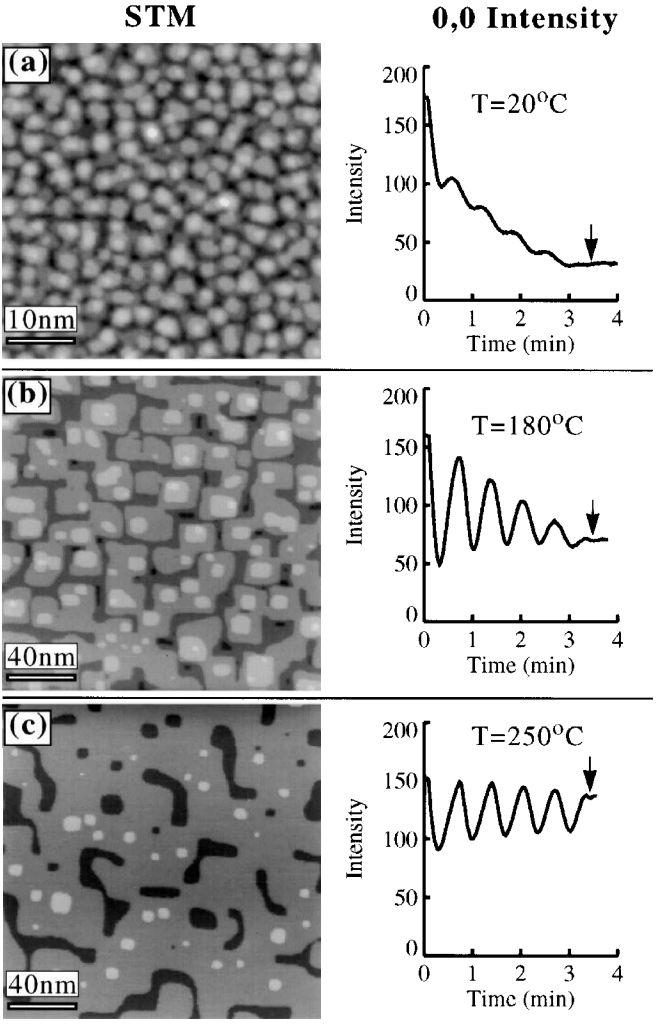

Figure 4. STM picture of Fe growing on Fe(100) in various growth modes at different temperatures. A correlation with RHEED oscillations is made (Stroscio *et al.* 1993).

change at 11 monolayers is due to metastable fcc Fe converting into ordinary bcc Fe. It can be delayed by using adsorbed CO as surfactant.

At the *lowest growth temperatures* the arriving atoms nucleate islands on top of each other, giving rise to rather *rough topographies*, such as that shown in figure 4 for Fe grown on Fe(100) (Stroscio *et al.* 1993). In this regime, diffusion along step edges and across step edges becomes an important parameter, in addition to the diffusion on top of terraces (Bott *et al.* 1992).

A recently developed non-equilibrium technique for growing films with monolayer control is *atomic layer epitaxy*. this 'digital' growth method consists of two reaction steps per layer. First, a monolayer of molecules is adsorbed on the surface under conditions where the second layer does not stick. Then the surface is reactivated by driving passivating ligands off, using a chemical reaction, light or a

temperature pulse. Such processes have been successful for semiconductors. For magnetic materials, one could consider carbonyls or aromatic compounds, such as ferrocene and bis-benzene chromium (Kaplan 1983, Matsui and Mori 1986, Stauf *et al.* 1987, Henderson *et al.* 1991, Zaera 1991, Welipitiya *et al.* 1996). With carbonyls, there is a strong tendency towards incorporating carbon and oxygen into the reactive ferromagnets.

Electrochemical deposition allows deposition at room temeprature under near-equilibrium conditions, which should be ideal for obtaining sharp interfaces. Its application to magnetic layers with monolayer control is just beginning (Schindler *et al.* 1997).

2.3. *Interfaces*

An important aspect of growing magnetic multilayers has been the quality of the interfaces, that is lateral smoothness and vertical sharpness. For example, the formation of quantized electronic states is dependent on interfaces that are smoother than the wavelength of the electrons, just as standing waves in an optical interferometer require mirrors smoother than the wavelength of the light (see section 5.3). The magnetoresistance in magnetic multilayers has been found to depend on the interface roughness, sometimes increasing and sometimes decreasing with increasing roughness. While roughness is mainly determined by the growth modes discussed above, the sharpness of an interface is governed by interdiffusion and chemical reaction (Weaver 1986). Some noble metals and ferromagnets have a large miscibility gap in the phase diagram, such as Fe–Cu, Fe–Ag and Co–Cu. Others form alloys, such as Ni–Cu and Fe–Au. While noble metals have little effect on ferromagnetic properties, other elements have greater effect. Arsenic, for example, diffuses into a growing Fe film on GaAs(100), which is lattice matched to Fe (Prinz 1991). The first 10 nm of Fe lose part of their magnetic moment, and the interface is magnetically dead (McGuire *et al.* 1984, Himpsel 1991c). Thicker epitaxial Fe films on GaAs (in the micrometre range) have excellent magnetic properties, and similarly on the less-reactive ZnSe already at 10 nm thickness (Jonker *et al.* 1987). S passivation of the GaAs surface is able to suppress As outdiffusion and allows high-quality Fe films in the nanometre regime (Anderson *et al.* 1995). Si as a substrate presents similar problems, since it reacts with most magnetic materials to form silicides. On the other hand, semiconductor substrates are highly desirable for magnetic multilayers since they do not short out the current flowing through a magnetic multilayer and are readily available and processed. As a consequence, there has been extensive work on buffer layers that prevent undesirable out-diffusion and reaction with the substrate, for example, S, Ge, Cr, Ag and Au buffers on GaAs and Ge (Ruckman *et al.* 1986, Farrow *et al.* 1988, Lee *et al.* 1989, Sands *et al.* 1990, Sano and Miyagawa 1991, Anderson *et al.* 1995, 1996) and Cu, Cr on Si (Nguyen-Van-Dan 1997, Parkin 1991). Insulators, such as MgO(100), MgO(110) and Al_2O_3(0001) are being used as substrates for epitaxial growth of various low-index surface, using metal seed layers (Lairson *et al.* 1992).

2.4. *Wires*

An entry into the one-dimensional world can be gained by growth at stepped surfaces. Fairly regular step arrays can be produced on vicinal metal and semiconductor surfaces (Wagner 1979, Henzler and Ranke 1993). For obtaining

the straightest possible steps, one needs to select the most stable azimuthal step orientation, usually consisting of close-packed atom rows (Feibelman 1995, Himpsel *et al.* 1994, Jung *et al.* 1995a, 1995b). On silicon, it is now possible to obtain steps with only one kink in 20000 lattice sites (Viernow *et al.* 1998). They form the boundaries of islands during equilibrium growth. Steps provide a template for attaching stripes or wires by step flow growth. Analogues to all the three-dimensional growth modes reappear in lower dimensions, such as layer-by-layer, Stranski–Krastanov and island growth. As shown in figure 5, Cu grows on a stepped Mo(110) surface in parallel stripes that correspond to a row-by-row growth mode, the equivalent of layer-by-layer growth. On W(110), however, only the first row of Cu atoms decorates the step edge (Himpsel and Ortega 1994), and additional Cu grows in monolayer-height islands that are attached to the step edges (Mo and Himpsel 1994), analogous to Stranski–Krastanov growth. The analogue of island growth has been observed for Co on stepped Cu(111), where Co islands nucleate at the step edges and eventually coalesce higher coverage (de la Figuera *et al.* 1995). Such a growth mode can be expected in general when attempting to grow the high-energy ferromagnets on low energy substrates, such as noble metals and insulators.

An additional phenomenon at stepped surfaces is a barrier for crossing steps. This is obvious for an uphill crossing, since the atom incorporated at the step edge would be less coordinated on the terrace, but even in the downhill direction there is a temporary loss of neighbours when crossing the step edge. An atom exchange mechanism can eliminate this barrier during homoepitaxy on certain metals (figure 6) (Lagally 1993, Stumpf and Scheffler 1994, Ehrlich and Hudda 1966). In a heteroepitaxial system, such as Cu/Mo(110) in figure 5, the Cu atom crossing a Mo–Cu boundary trades Mo neighbours for Cu neighbours, which provide less binding energy. Such a barrier is reflected in the width of the Cu stripes on Mo(110) shown in figure 5. The wider the terrace that a Cu stripe resides on, the wider is the stripe (Jung *et al.* 1995b, Petrovykh *et al.* 1997). Apparently, the Cu atoms are swept towards the uphill edge of an individual terrace. It requires higher annealing temperatures to let atoms travel across step edges and obtain a uniform stripe width, independent of terrace width. The existence of such a uniform stripe width despite non-uniform terrace width indicates that the binding energy increases towards the step edge in this case. In order to make step decoration a widely applicable technique it has been proposed to use a two-step process (Jung *et al.* 1995b, Himpsel *et al.* 1997). In the first step, a template of inert stripes is grown by step decoration. In the second step, the desired material is grown by selective chemical vapour deposition on the remaining parts of the reactive substrate.

In addition to step decoration there are various other mechanisms that lead to spontaneous formation of wires and stripes, for example growth on anisotropic surfaces. Deposited atoms diffuse parallel to atom rows at the fcc (110) surface, but not perpendicular (Röder *et al.* 1993, figure 7b). Adsorbates have been found to self-organize into stripes on such surfaces (Kern *et al.* 1991). An unusual patterning method uses the interference field of an intense laser to focus a beam of Cr atoms into a regular grating with line widths down to the 40 nm range (Celotta *et al.* 1996). Lithographic patterning and side evaporation onto lithographic steps have been used to produce sawtooth-shaped Si substrates for the deposition of magnetic stripes (Prober *et al.* 1980, Ono and Shinjo 1995, Oepts *et al.* 1996). Magnetic wires perpendicular to the surface have been obtained by filling pores in a polymer film with electroplated metals (Blondel *et al.* 1994, Piraux *et al.* 1994, Liu *et al.* 1995).

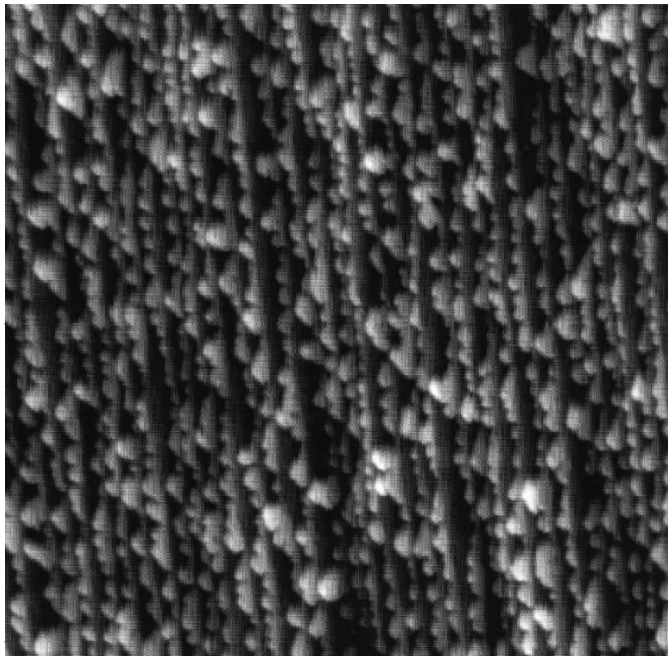

(*a*)

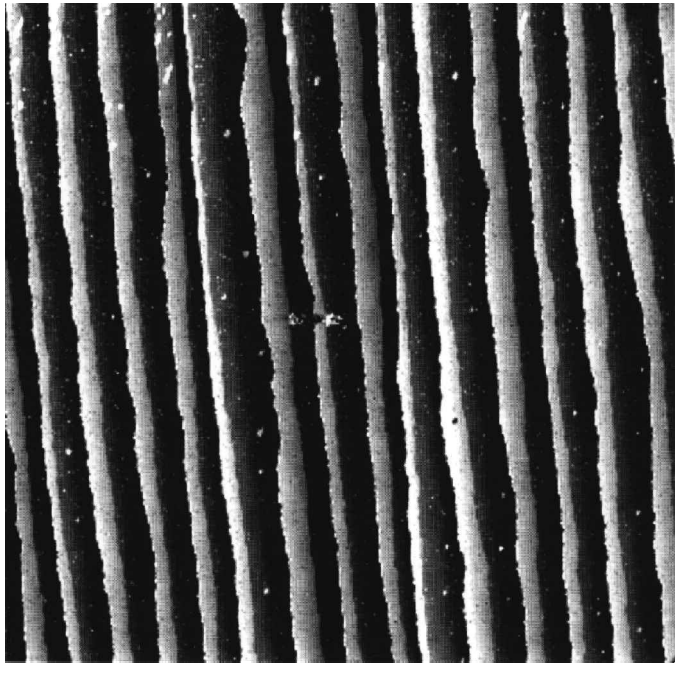

(*b*)

Figure 5. Growth modes in two dimensions. Cu (*a*) on stepped W(110) and (*b*) on Mo(110) displays the analogue of Stranski–Krastanov and layer-by-layer growth (compare figure 2) (Jung *et al.* 1995b).

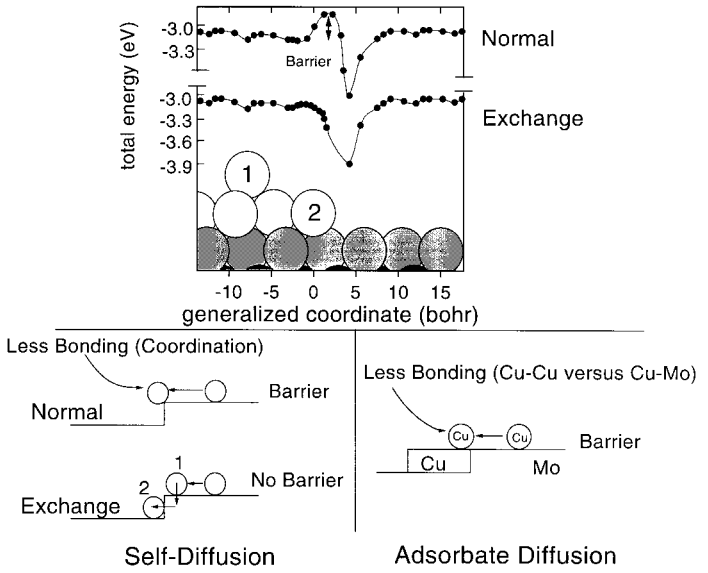

Figure 6. Diffusion across step edges. The energy barrier for diffusion is due to the reduced coordination on top of the step. It can be reduced by exchanging atoms at the step edge (Stumpf and Scheffler 1994). A new barrier appears for diffusion onto a stripe with weak bonding to the adatom, such as in figure 5.

Both of these structures are designed to achieve higher magnetoresistance than in planar multilayers.

2.5. *Particles*

For growing zero-dimensional magnetic structures, that is fine particles with uniform size, one may either consider the processing methods for particles in magnetic tapes or emulate the fabrication of 'quantum dots' on semiconductors. Dots are expected to exhibit the most singular behaviour among low-dimensional structures (see section 3), but they also present the highest difficulty in connecting them to the macroscopic world, for example by nanometre-sized electrical contacts, by optical read-out or by remotely sensing an electric or magnetic field.

The processing of magnetic particles for magnetic tapes has experienced a long development of ever more sophisticated processing methods (Mallinson 1987, chapter 3). In order to achieve high coercive fields, that is high stability, these particles are grown needle-shaped (acicular) with a typical length of 0.5 μm and width of 0.1 μm. Initially, seed particles 10 nm long of $Fe(OH)_2$ are precipitated from a $FeSO_4$ solution by adding NH_4. Controlled ripening and reduction–oxidation cycles eventually produce particles consisting of Fe_2O_3 or Fe with special coatings that serve as chemical protection and shape the magnetic properties. With semiconductors, highly homogeneous nanocrystals have been obtained by seeding in a supersaturated solution, followed by controlled ripening with passivation layers and size-selective precipitation. The size distribution is better than 4%, which is close to monolayer control (Alivisatos *et al.* 1989, Murray *et al.* 1993). The surface analogue of seeding plus ripening consists of nucleating seeds with the critical nucleus size by deposition at low temperature, where atoms are immobile. The size of these critical nuclei can then be very uniform, for example Ag dimers on Pt(111) in the experiment

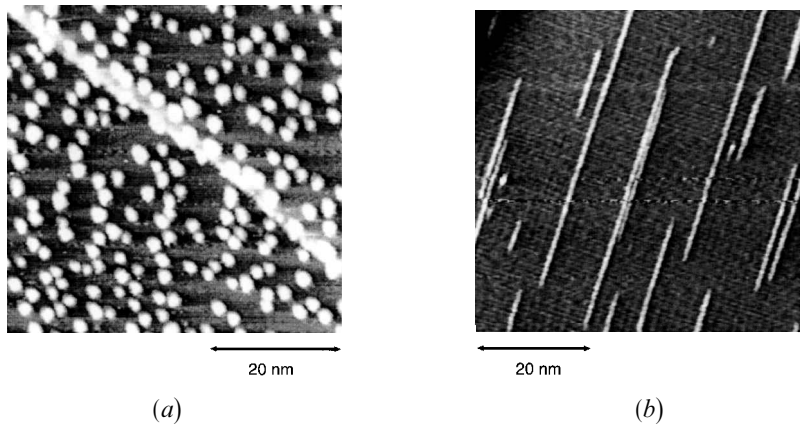

Figure 7. Growth of particles and wires at metal surfaces (Röder *et al.* 1993). Homogeneous particles are grown on Pt(111) by nucleation of Ag dimers at a low temperature and subsequent ripening. Monatomic Cu wires are formed along the atomic rows of a Pd(110) surface via anisotropic diffusion.

by Röder *et al.* (1993) shown in figure 7a. The size of these seeds is increased in controlled fashion at somewhat higher temperature, where they sweep in adatoms within a diffusion length.

The step decoration method discussed in section 2.4 can be extended to zero-dimensional structures by letting adatoms diffuse to kinks, which nucleate a regular array of dots. This has been tried successfully for semiconductors. Likewise, a regular array of misfit dislocations can serve as a template for nucleation of dots (Nötzel *et al.* 1994, Tersoff *et al.* 1996). A similar nucleation has been found on reconstructed metal surfaces with dislocations, built in either by an intrinsic reconstruction (Chambliss *et al.* 1991) or by a mismatched adsorbate layer (Condon *et al.* 1995).

On the low end of the particle size spectrum we have clusters of a few atoms and magnetic molecules. Cluster research has brought about several techniques for obtaining microscopic quantities of mass-selected clusters. For example, an iron target is vaporized by a laser, injecting hot Fe atoms and ions into a He carrier gas, where they condense and ripen into clusters of a few atoms in size. Supersonic expansion of the carrier gas produces a cold cluster beam that can be mass selected (Klots *et al.* 1991, Wang *et al.* 1996a). Interesting magnetic molecules, such as the 'ferric-wheel' or ferritin proteins can be synthesized directly (Gatteschi *et al.* 1994, Awschalom *et al.* 1995). Small magnetic particles are also encountered in biological systems, for example Fe stored in the spleen and magnetic field sensors in fish and bacteria (Blakemore and Frankel 1981, Awschalom *et al.* 1992, 1995).

2.6. *Writing of structures*

All the growth methods discussed so far rely on parallel processing or self-assembly. For example, decorating step edges of a vicinal surface produces 10^6 wires per cm^2 simultaneously. This is the economical way to produce a macroscopic amount of material. However, there are limitations. It is impossible to write custom patterns, and one has to cope with a finite size distribution, for example in the width of wires or the diameter of dots. For writing structures down to a scale of about

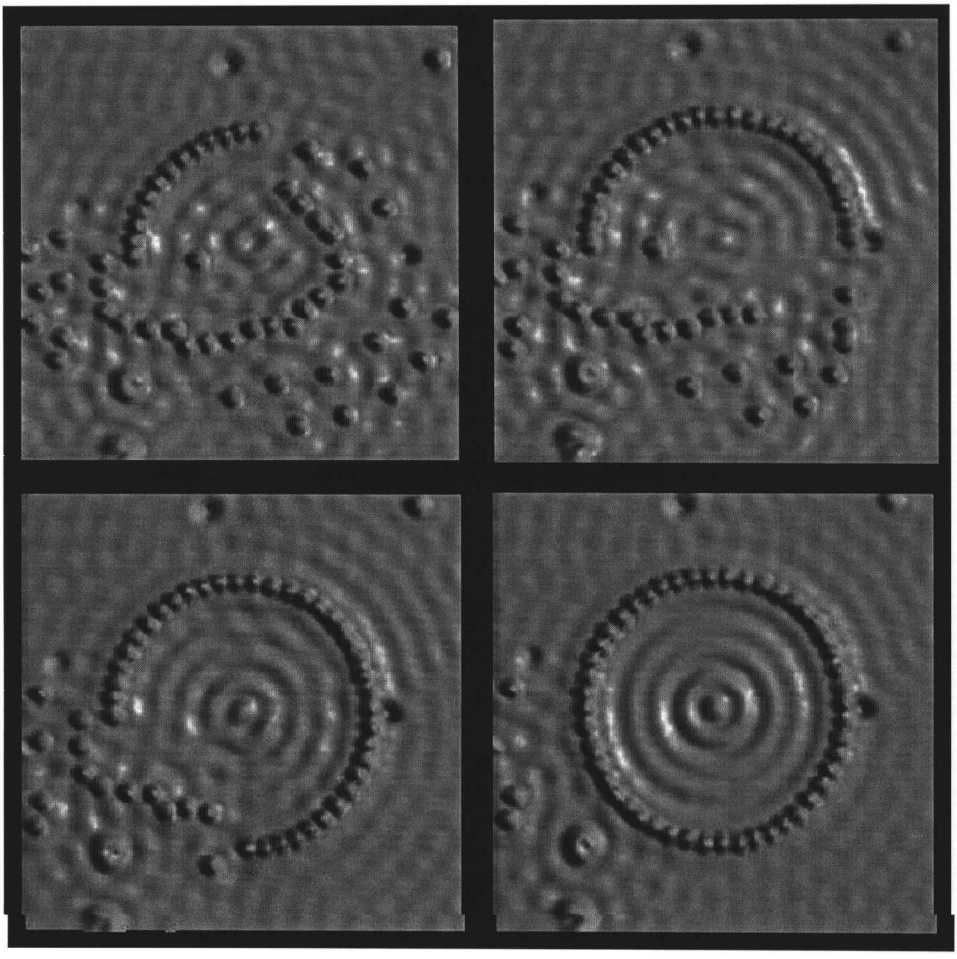

Figure 8. Construction of a quantum corral from single Fe atoms on a Cu(111) surface. The STM tip is used to drag evaporated Fe atoms across the surface. The ripples inside the ring of Fe atoms are due to charge-density waves of electrons confined to the corral (see section 6) (Crommie *et al.* 1993b).

200 nm it is feasible to use optical lithography. Electron-beam lithography reaches 15 nm (Chou *et al.* 1996). Such techniques have been used to produce magnetic wires (Chou *et al.* 1994, Ono and Shinjo 1995, Oepts *et al.* 1996), as well as dots (Lederman *et al.* 1994, Chou *et al.* 1994, New *et al.* 1995a, b, Chou *et al.* 1996, Hehn *et al.* 1996, Levy *et al.* 1996, Runge *et al.* 1996, O'Barr *et al.* 1997).

For writing structures with atomic perfection there is the possibility of moving atoms or molecules with the tip of a scanning tunnelling microscope (STM). Crommie *et al.* (1993b) arranged Fe atoms into a corral on a Cu(111) surface (figure 8). The idea is to approach the adatom close enough that the force holding it to the tip overcomes the lateral forces when moving across surface corrugations. On the other hand, the tip force should be weaker than the bond to the surface, such that the atom does not end up on the tip. Such controlled atom movement has been achieved only at low temperatures so far. There have been successful efforts to move larger entities, such as organic molecules at room temperature (Jung *et al.* 1996). STM has

also been used on a much larger scale to produce 50 nm lines and dots by cracking Ni and Fe carbonyls with the electrons emitted from an STM tip (Ehrichs *et al.* 1992, Kent *et al.* 1993).

3. Characterization

This section defines the fundamental parameters that characterize electronic structure and magnetic properties. Among the wide variety of techniques that are available to measure these quantities we illustrate the most common methods by examples involving the elemental ferromagnetic materials Fe, Co, Ni and Gd. Photoemission and inverse photoemission are the standard techniques for probing occupied and unoccupied electronic states respectively. To determine magnetic properties, on the other hand, a much larger arsenal of techniques is required. Conventional bulk-sensitive techniques, such as neutron scattering, have difficulties detecting the small amount of magnetic material encountered in nanostructures. To improve surface sensitivity it is useful to utilize probing particles with a short penetration depth, such as low-energy electrons. For reaching nanometre spatial resolution in all dimensions there are a number of innovative magnetic microscopies under development.

3.1. *Electronic structure*

Electrons in a solid are completely characterized by a set of *quantum numbers*. These are energy E, momentum $\mathbf{k}$, point-group symmetry (i.e. angular symmetry) and spin. This information can be summarized by plotting $E(\mathbf{k})$ band dispersions with the appropriate labels for point-group symmetry and spin. Disordered solids (e.g. random alloys) can be characterized by average values of these quantities, with disorder introducing a broadening of the band dispersions. Localized electronic states exhibit flat $E(\mathbf{k})$ band dispersions, for example in ionic compounds or in the 4f levels of rare earths. In the following we shall focus on band-like or itinerant magnetism, which is characteristic of s, p and d levels in transition metals and rare earths. These materials have been used in most studies of magnetic nanostructures.

A complete set of quantum numbers is obtainable from photoemission and its time-reversed counterpart, that is, inverse photoemission (figure 9). The former probes occupied states, and the latter unoccupied states). For reviews on photoemission see Plummer and Eberhardt (1982), Himpsel (1983) and Kevan (1992) and for inverse photoemission see Dose (1985), Himpsel (1986) and Smith (1988b). At kinetic energies of 1–100 eV the electron's mean free path is only a few atomic layers (figure 10), making it possible to detect surface states as well as bulk states in thin-film structures. The local electronic states in nanostructures can be approached by scanning tunnelling spectroscopy which gives up momentum resolution to gain spatial resolution.

3.1.1. *Energy bands*

How are energy band dispersions determined? A first look at the task reveals that photoemission (and inverse photoemission) provides just the right number of independent measurable variables to establish a unique correspondence to the quantum numbers of an electron is a solid. The energy E is obtained from the kinetic energy of the electron. The two momentum components $\mathbf{k}^{\parallel}$ parallel to the surface are derived from the polar and azimuthal angles of the electron. The third momentum component $k^{\perp}$ is varied by tuning the photon energy $h\upsilon$. A complete

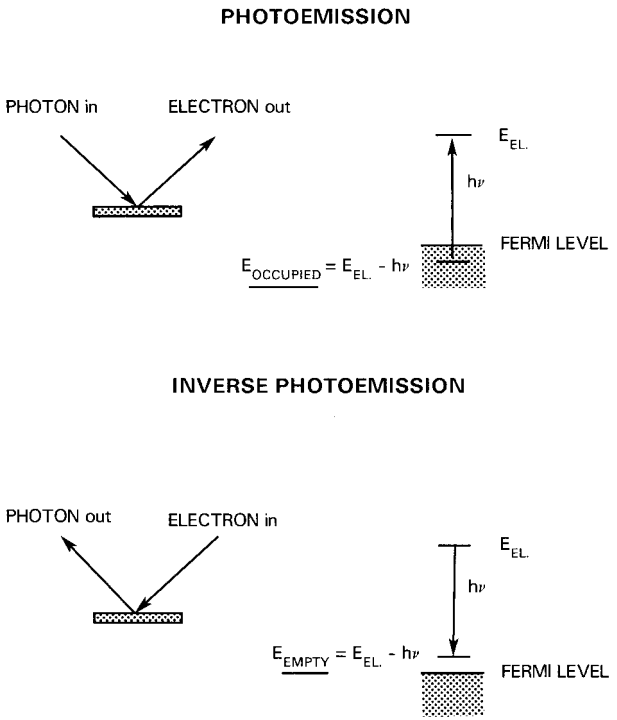

Figure 9. Photoemission and inverse photoemission as probes of occupied and unoccupied electronic states respectively. All the quantum numbers of an electron can be determined.

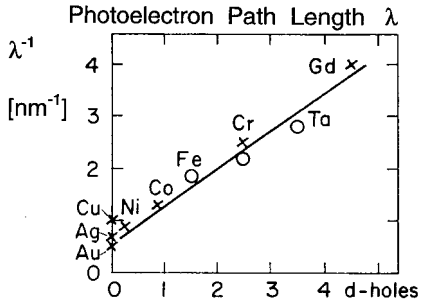

Figure 10. Probing depth in photoemission and inverse photoemission, represented by the mean free path λ of electrons at an energy of about 5 eV above the Fermi level. Transition metals with more d holes scatter electrons more strongly (Schönhense and Siegmann 1993).

band-structure determination requires a tunable photon source, such as synchrotron radiation, or a tunable photon detector in inverse photoemission. The polarization of the photon provides the point-group symmetry, and the spin polarization of the electron the spin quantum number.

For two-dimensional states in thin films and at surfaces the determination of energy bands is almost trivial since only E and $\mathbf{k}^{\|}$ have to be determined. These quantities obey the conservation laws

$$E_{\mathrm{l}} = E_{\mathrm{u}} - h\upsilon \tag{3}$$

and

Table 3. Empirical potential parameters for the band structures of the elemental ferromagnets Fe, Co, Ni and Gd in figure 11, using the combined interpolation scheme. See Slater and Koster (1954) for the 3d bands, Smith and Mattheis (1974) and Smith *et al.* (1982) for the fcc plane waves, Smith (1988a) for bcc plane waves, and Papaconstantopoulos (1986) for the hcp bands.

	Potential (eV)					Potential (eV)	
	Fcc Ni	Fcc Co	Fcc Fe	Bcc Fe		Hcp Co	Hcp Gd
Plane waves					s_0p_0	- 2.65	- 0.2
α	12.5	12.5	12.5	0.3	p_0	16.05	9.7
V_{000}	- 8.8	- 8.3	- 8.0	- 8.15	$d_0\uparrow$	- 1.6	1.9
V_{200}	1.65	1.7	1.4	1.2	$d_0\downarrow$	- 0.5	2.9
V_{111}	1.47	1.51	1.19	—	$d_1\uparrow$	- 1.3	1.9
V_{110}	—	—	—	1.0	$d_1\downarrow$	- 0.2	2.9
V_{211}	—	—	—	1.2	$d_2\uparrow$	- 1.6	1.7
3d bands					$d_2\downarrow$	- 0.5	2.7
$d_0\uparrow$	- 1.241	- 1.871	- 1.450	- 1.338	pd_0	0.0	- 0.04
$d_0\downarrow$	- 0.941	- 0.671	- 0.250	0.762	$ss\sigma_1$	- 0.475	- 0.2
$dd\sigma_1$	- 0.367	- 0.483	- 0.517	- 0.600	$sp\sigma_1$	0.9	- 0.4
$dd\pi_1$	0.200	0.275	0.250	0.167	$sd\sigma_1\uparrow$	0.2	0.34
$dd\delta_1$	- 0.011	- 0.005	0.011	- 0.001	$sd\sigma_1\downarrow$	0.1	0.25
$(dd_x)_2$:$(dd_x)_1$	0.052	0.020	0.0	0.220	$pp\sigma_1$	2.2	0.6
Hybridization					$pp\pi_1$	0.03	- 0.18
R	3.28	3.28	3.28	4.48	$pd\sigma_1$	0.33	0.34
S	18.8	12.2	13.4	13.0	$pd\pi_1$	- 0.1	- 0.75
$B_t = B_e$	13.5	18.7	17.0	19.0	$dd\sigma_1$	- 0.41	- 0.95
					$dd\pi_1$	0.21	0.38
					$dd\delta_1$	- 0.03	- 0.01
					x_2:x_1	0.11	0.12
					x_3:x_1	0.02	0.03

$$\mathbf{k}_l^{\parallel} = \mathbf{k}_u^{\parallel} - \mathbf{g}^{\parallel}, \tag{4}$$

where $\mathbf{g}^{\parallel}$ is a vector of the reciprocal surface lattice, u denotes the upper state and l the lower state. These conservation laws can be derived from the invariance of the crystal with respect to translation in time and in space (by a surface lattice vector). For the photon, only its energy $h\upsilon$ appears in the balance because the momentum of an ultraviolet photon is negligible compared with the momentum of the electrons. The subtraction of a reciprocal lattice vector simply corresponds to plotting energy bands in a reduced surface Brillouin zone, i.e. within the unit cell in $\mathbf{k}^{\parallel}$ space. These are the rules of band-mapping in a nutshell. An in-depth discussion of the practical aspects and capabilities of these methods is given in several reviews (Plummer and Eberhardt 1982, Himpsel 1983, Kevan 1992).

The *experimental bulk bands* of the elemental ferromagnets Fe, Co, Ni and Gd are shown in figure 11. They are characterized by a region of flat d bands embedded into a steep s, p band. The d bands are narrower than the s, p band because d states are more localized, giving less overlap between adjacent atoms and a smaller energy spread between bonding and antibonding combinations of d states. As the atomic number increases from Fe to Co and Ni, the d bands become increasingly filled and move down below the Fermi level. Gd exhibits additional f states, which are so localized that they do not exhibit any measaurable band dispersion. Since the f shell

is half-filled and fully polarized in Gd, one has an occupied f level with majority spin, as well as an unoccupied f level with minority spin. The seemingly complex set of d bands can be fitted by a rather small set of parameters by combined interpolation schemes, which combine a tight-binding approach for the d bands with plane waves for the s, p bands (Smith *et al.* 1982). The parameters given in table 3 describe the energy bands in figure 11, which are obtained from a best fit to photoemission and

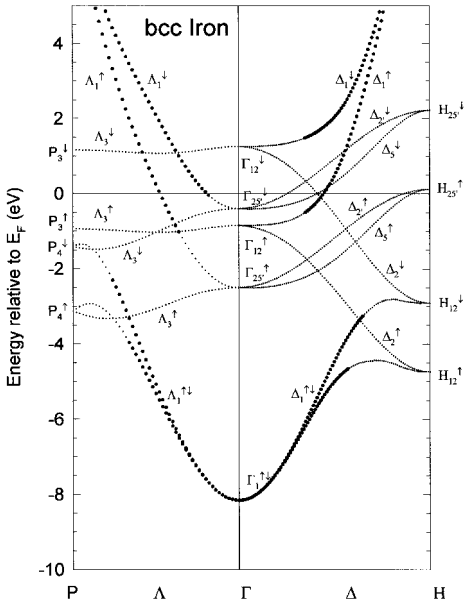

11(*a*)

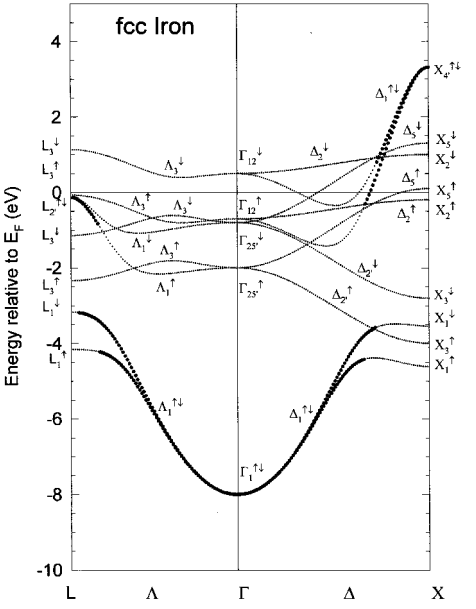

11(*b*)

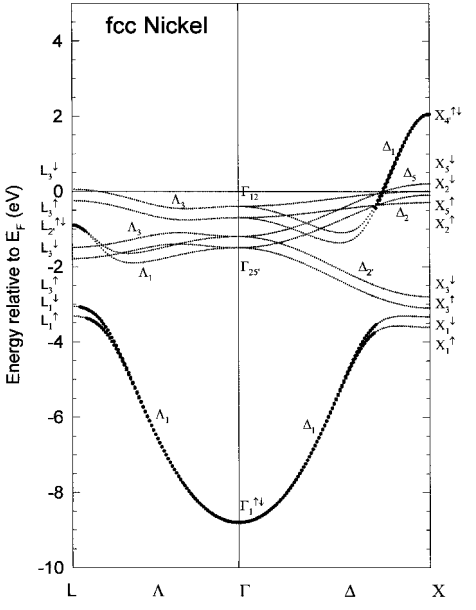

11(*c*)

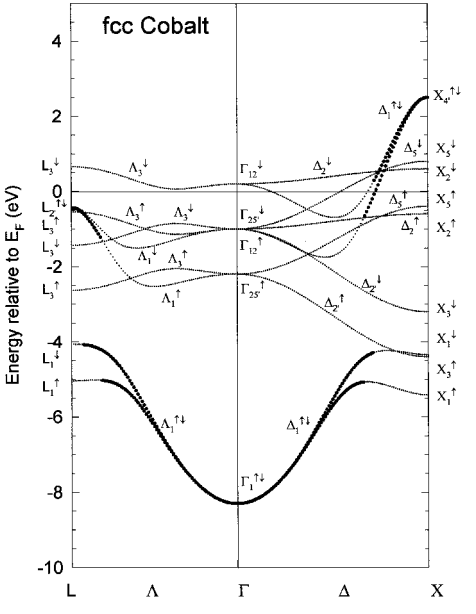

11(*d*)

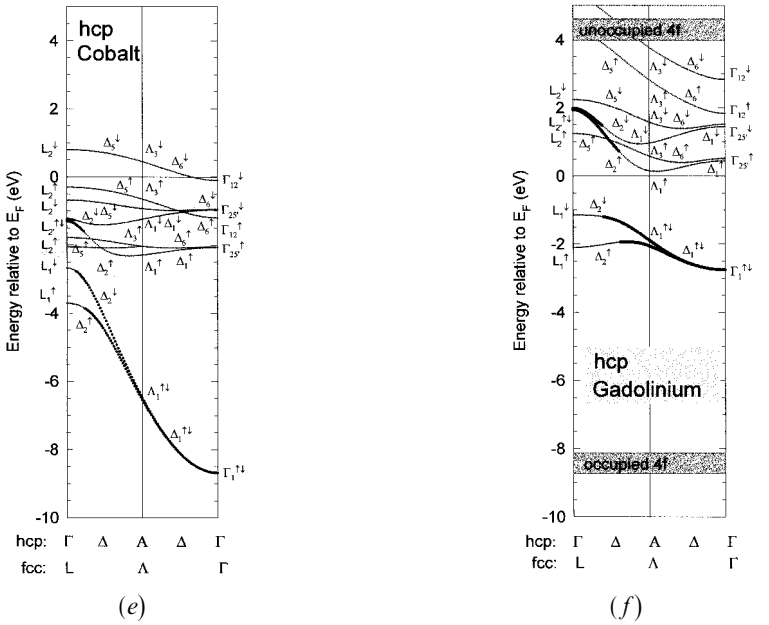

Figure 11. Empirical bulk band structures of the elemental ferromagnets Fe, Co, Ni and Gd, obtained from a fit to photoemission and inverse photoemission data (see table 3). Included are metastable phases, such as fcc Fe and fcc Co. Bands with s, p character are highlighted by bold symbols (50% or more plane-wave character for fcc, and 40% or more for bcc).

inverse photoemission data. For bcc Fe, see Turner *et al.* (1984), Kisker *et al.* (1985), Santoni and Himpsel (1991) and references therein, for hcp Co see Himpsel and Eastman (1980) and Mankey *et al.* (1993a), for fcc Ni see Himpsel *et al.* (1979), Eberhardt and Plummer (1980), Heimann *et al.* (1981), Smith *et al.* (1982), Raue *et al.* (1983) and Donath (1989), for hcp Gd see Li *et al.* (1994a), for metastable fcc Fe and Co see Mankey *et al.* (1993b) and for metastable bcc Ni see Brookes *et al.* (1992).

There exist first-principles *band calculations* using local density theory (Moruzzi *et al.* 1978, Papaconstantopoulos 1986), but they compute $E(\mathbf{k})$ relations for the ground state, a quantity that is not accessible to any experiment. In order to measure the energy of an electron it is necessary to excite it above the Fermi level. Such an excitation produces a response from the surrounding electrons, for example multi-electron excitations and screening. Two-electron excitations lead to a narrowing of the 3d band and reduce the magnetic exchange splitting, for example as much as 30% band narrowing and a factor of $\frac{1}{2}$ in the magnetic splitting (Himpsel *et al.* 1979, Liebsch 1979). The two-electron excitations show up directly as satellites below the single-electron bands, for example the 6 eV satellite in Ni (Guillot *et al.* 1977). These excited-state effects are strongest in Ni, weaker in Co and barely perceptible in Fe. Theoretical methods do exist that take excited-state effects into account systematically from first principles. Such quasiparticle calculations have been very successful for semiconductors (Hybertsen and Louie 1986) but are just becoming feasible for d and f electrons in magnetic materials (Steiner *et al.* 1992). In the absence of such first-principles calculations we provide empirical band structures as a starting point for describing electronic states at surfaces, thin films and nanostructures.

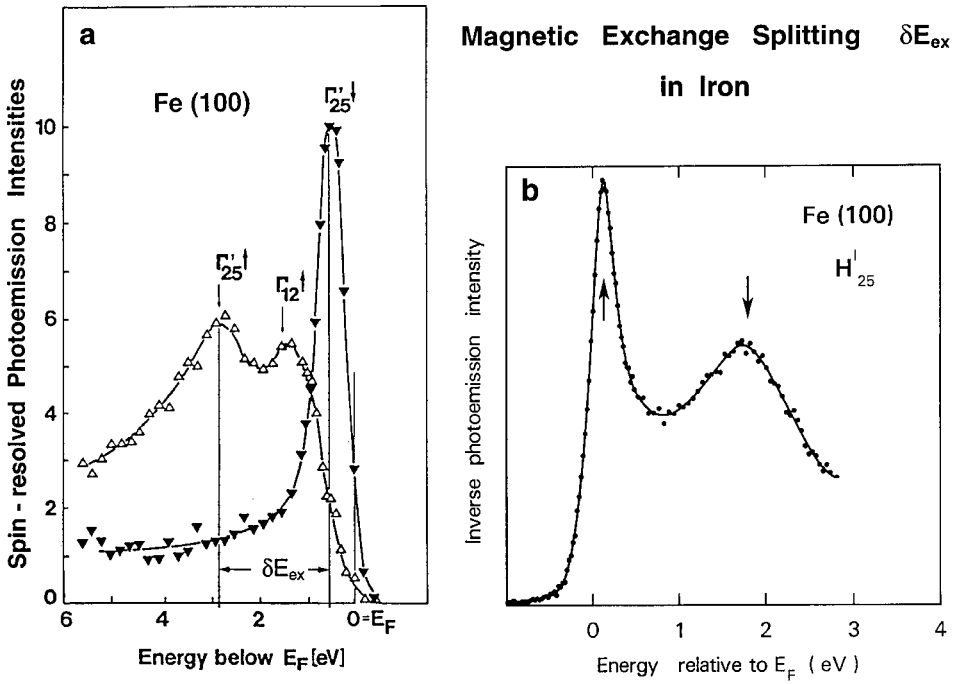

Figure 12. Ferromagnetic exchange splitting between majority and minority spin bands in Fe. (a) Probed by spin-polarized photoemission at Γ_{25} (Kisker *et al.* 1985). (b) Probed by inverse photoemission at H_{25} (Santoni and Himpsel 1991, compare also Kirschner *et al.* 1984).

3.1.2. *Magnetic exchange splitting*

For *ferromagnets* the bands are split into two subsets: one with majority spin, and the other with minority spin. The *magnetic exchange splitting* δE_{ex} between majority and minority spin bands is the key to magnetism. Owing to the exchange splitting the minority spin band is filled less than the majority band, thus creating the spin imbalance that produces the magnetic moment. Therefore, one might expect the moment to increase with the exchange splitting (Gunnarson 1976). For example, the values of δE_{ex} in Fe, Co and Ni are 1.8–2.4 eV, 0.93–1.05 eV and 0.17–0.33 eV respectively (Himpsel 1991b). The corresponding moments are 2.2 μ_B, 1.7 μ_B and 0.6 μ_B respectively. Most of the moment is carried by the 3d electrons (about 110%), whereas the s, p electrons are weakly polarized in the opposite direction (about - 10% of the total moment). For Gd, one has a total moment of 7.6 μ_B carried mostly by the 4f electrons (7μ_B), with the 5d electrons contributing 0.6 μ_B. The exchange splitting is δE_{ex} = 12.4 eV for the 4f states (Ortega *et al.* 1994) and δE_{ex} = 0.8 eV for the 5d states (Kim *et al.* 1992, Li *et al.* 1995a). Results for δE_{ex} of Fe from spin-resolved photoemission and from inverse photoemission are shown in figure 12. There is some variation in δE_{ex} with momentum **k**, which appears to be mainly tied to the symmetry of the bands. Bands with t_{2g} (Γ_{25}, X_5) symmetry have a larger splitting than those with e_g (Γ_{12}, X_2) symmetry, for example 0.33 eV as against 0.17 eV in Ni (Liebsch 1979, Heimann *et al.* 1981). This variation blurs the expected correlation between δE_{ex} and the magnetic moment. Nevertheless, the momentum- and symmetry-averaged value of δE_{ex} turns out to be an indicator of the local magnetic moment for 3d transition metals, not only for ferromagnets but also for

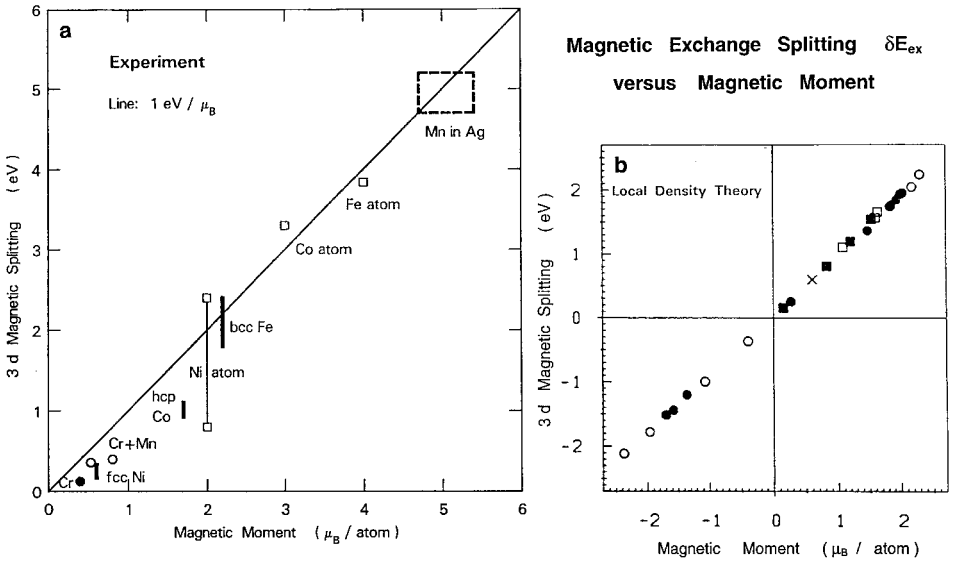

Figure 13. Approximate relation of 1 eV per Bohr magneton between magnetic exchange splitting δE_{ex} and local magnetic moment μ for 3d electrons. (a) Experimental data compiled by Himpsel (1991b). (b) Calculation for various alloys by Turek *et al.* (1992). For a connection between the $\delta E_{ex}/\mu$ ratio and the Stoner parameter I determining ferromagnetism in figure 17 and equation (5) see Gunnarson (1976) and Pettifor (1980).

antiferromagnets and, in the absence of long-range order, for spin glasses and free atoms (figure 13). As an empirical rule of thumb, the 3d moment is about 1 μ_B per electron volt exchange splitting. This trend provides a quick first look at the size of the local moments in thin-film and monolayer systems (Himpsel 1991b, Hopster 1994). It is interesting to note that the $\delta E_{ex}/\mu_B$ ratio in figure 13 is connected to the exchange integral I that determines ferromagnetism—see equation (5) and the Stoner model below (Gunnarson 1976, Janak 1977, Pettifor 1980).

Antiferromagnets exhibit magnetic splittings, too. For delocalized band-like states, such as in Cr, the splittings occur around the points in momentum space that correspond to the reciprocal-lattice vectors of the antiferromagnetic spin ordering. For example, along the direction of the alternating spins the antiferromagnetic splitting occurs half-way out to the Brillouin zone boundary of the atomic lattice. The doubling of the unit cell in real space by the spin lattice halves the unit cell in momentum space, and the magnetic interaction opens up bandgaps at the magnetic Brillouin zone boundary. The upper state corresponds to a spin-down electron at a spin-up site and vice versa, and the lower state to a spin-up electron at a spin-up site and vice versa. The situation is similar to that in a ferromagnet when considering the spin polarization at a particular atom; local minority states are at higher energy than local majority states. Optical data give a magnetic splitting of 0.13 eV for pure Cr which exhibits a slightly incommensurate magnetic period (compare figure 39). The splitting increases to 0.36 eV when the antiferromagnetism becomes commensurate by 1% Mn or Re doping (Bos and Lynch 1970). In antiferromagnets with localized states the bands have little $E(\mathbf{k})$ dispersion and the splitting extends throughout most of the Brillouin zone.

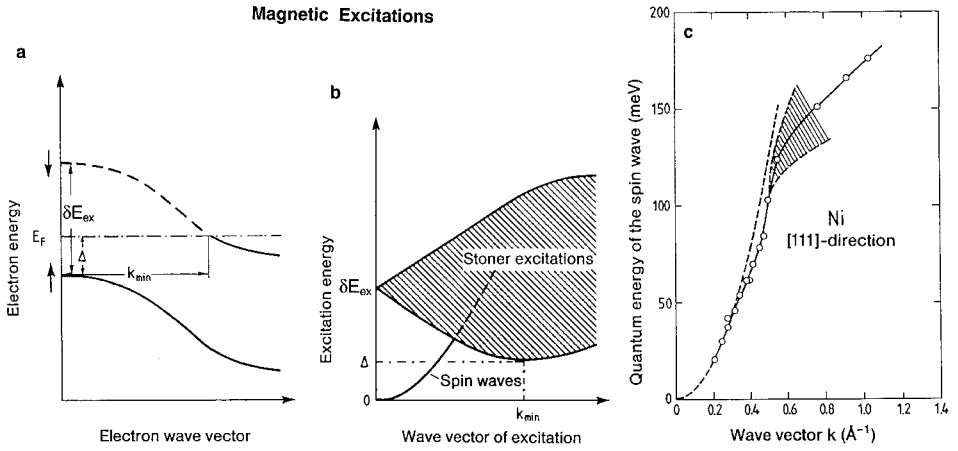

Figure 14. Magnetic excitations (adapted from Ibach and Lüth 1993). (a) Spin-split bands crossing the Fermi level. A spin flip can occur via a single electron excitation by lifting an electron from the majority band into the unoccupied part of the minority band (- - -). Such excitations require a minimum energy transfer equal to the Stoner gap Δ. (b) Schematic $E(\mathbf{k})$ diagram of magnetic excitations. One can distinguish between single-electron (Stoner) excitations and many-electron excitations (equivalent to spin waves or magnons). (c) Neutron scattering results for a spin wave merging into the continuum of Stoner excitations (Mook and Paul 1985).

Magnetic excitations can also be described by an $E(\mathbf{k})$ diagram, where E and $\mathbf{k}$ are energy and momentum transfer respectively (figure 14). One may classify them into single- and many-electron excitations. The fundamental single-electron excitation is a transition between bands of opposite spin (figure 14(a)). It requires a minimum energy Δ in ferromagnets with a filled majority spin band, such as Co and Ni ('strong ferromagnets'). This *Stoner gap* Δ can be read off the band structures in figure 11. It is 0.35 eV in Co—from E_F to L_3, Γ_5 (Himpsel and Eastman 1980) and 0.11 eV in Ni—from E_F to X_5 (Heimann *et al.* 1981, Raue *et al.* 1983). Fe lacks such a gap since the top of the majority spin band lies above the Fermi level—0.12 eV for H_{25} (Santoni and Himpsel 1991). At zero momentum transfer the energy of the spin-flip excitations corresponds to the magnetic exchange splitting δE_{ex}. That can be probed by spin-polarized electron-energy loss spectroscopy (Hopster 1994).

The fundamental many-electron excitation is a *spin wave* (equivalent to a *magnon* —see figure 14(b)). Spin waves are low-energy excitations. They start out with a parabolic $E(\mathbf{k})$ dispersion at $\mathbf{k} = \mathbf{0}$ and broaden out when they begin to overlap with single-electron excitations above the Stoner gap. Many of these single- and many-electron excitations become thermally accessible near the Curie temperature, making finite-temperature calculations of the band structure and of the Curie temperature rather challenging (Uhl and Kübler 1996). Special spin-wave modes develop at surfaces and in multilayers owing to the altered boundary conditions (Camley *et al.* 1983, Kueny *et al.* 1984).

3.2. *Magnetism*

Magnetism reflects the underlying band structure. The magnetic moment is given by the difference between the filling of majority and minority spin bands, which is directly related to the ferromagnetic exchange splitting between the bands. Total

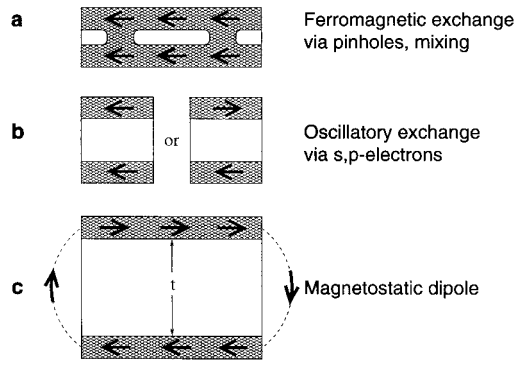

Figure 15. Coupling between magnetic layers (▒) via non-magnetic spacers of varying thickness t (□). (a) In the near-contact region, direct exchange dominates (usually ferromagnetic). (b) For spacer of a few nanometres, an oscillatory coupling is mediated by s, p electrons (RKKY interaction; see section 5.4 and figures 38–40). (c) At the largest distances, magnetic dipole interaction orients the layers antiparallel, like macroscopic bar magnets.

energy minimization over all occupied band states yields crystal structure and magnetic ordering. Magnetic coupling and magnetic moment are sensitive functions of the interatomic spacing and the atomic volume respectively, as illustrated in figures 15 and 16. Both are dominated by the Coulomb and/or exchange interactions at small distances. In a somewhat oversimplified atomic orbital picture, the moment is created by interaction between electrons on the same atom and the coupling between electrons on different atoms. Spins are aligned antiparallel at the smallest distances or volumes, since Pauli's exclusion principle prevents equal spins from occupying the same spot. This reduces the moment of an individual atom and produces antiferromagnetic coupling between atoms. The interaction changes its sign as soon as the wavefunctions cease to overlap strongly. The moment increases and the coupling becomes ferromagnetic. At even larger distances the magnetic coupling becomes indirect, using conduction electrons as mediators. It oscillates with a period determined by Fermi wave-vectors, thereby bringing orientation-dependent Fermi surface parameters into the picture. More sophisticated treatments, such as local density theory, take the band-like (itinerant) nature of the 3d wavefunctions in metallic ferromagnets into account, which blurs the simple atomic picture.

There is much more to magnetism than the spin-split band structure. Magnetic domains provide a large-scale texture that adds enormous complexity. As a consequence, there are many more magnetic properties than band-structure parameters, and a large number of techniques to measure them. The variability of an $H(M)$ hysteresis loop reflects a complex domain structure. Interestingly, the situation becomes simpler in nanostructures, which are smaller than the typical extension of a domain wall (0.1–1 μm). They often exhibit a square hysteresis loop. Magnetic anisotropy and magnetostriction in thin films demonstrate that magnetic ordering is sensitive to small energy changes that are induced by the presence of an interface and by strain.

It is important to keep the characteristic *energy scales* for band structure and magnetism in mind; the width of the s, p bands is given by the kinetic energy at the Fermi level, which is of the order 10 eV. The magnetic band splitting δE_{ex} of about

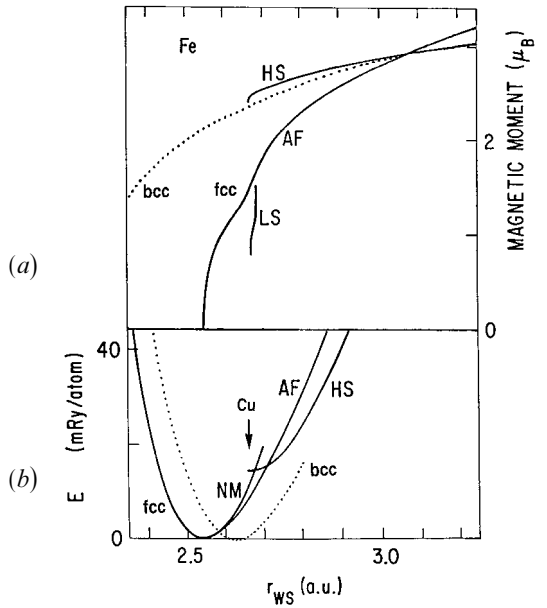

Figure 16. Magnetic moment and total energy of fcc Fe (——) and bcc Fe (.....) against interatomic distance (calculations by Moruzzi *et al.* 1986, 1989 and Moruzzi and Marcus 1992). Several magnetic phases are predicted by these first-principles calculations (curve NM, non-magnetic; curve AF, antiferromagnetic; curve LS, low-spin ferromagnetic; curve HS, high-spin ferromagnetic). They are sensitive to the interatomic distance. Constraining Fe to the lattice constant of Cu (arrow) produces fcc Fe very close to the transition between antiferromagnetic and ferromagnetic, explaining the complex phase diagram for Fe on Cu(100) in figure 20. r_{ws} is the radius of a Wigner–Seitz sphere with the volume per atom (1 a.u. = 0.53 Å).

1 eV derives from the Coulomb and/or exchange interactions. The spin–orbit coupling, which gives rise to crystalline anisotropy, is of the order of 0.1 eV for the 3d electrons in ferromagnets. The magnetic exchange coupling J is of the order of 0.01 eV atom^{-1}. The crystalline magnetic anisotropy is only about 10^{-5} eV atom^{-1} in the bulk but can increase to 10^{-4} eV atom^{-1} in the lower symmetry of a surface. Then it matches the shape anisotropy, which reflects the magnetic dipole–dipole interaction.

3.2.1. *Magnetic properties: magnetization, magnetic coupling, magnetostriction and anisotropy*

Magnetization and magnetic coupling are calculable from first principles by band theory. Today, the most common approach uses the local density formalism, where the spin-dependent part of the total energy is approximated by an expression derived from an electron gas (Von Barth and Hedin 1972). The corresponding exchange–correlation potential $V_{xc} = V_x + V_c$ depends only on the majority and minority spin densities $\rho\uparrow$ and $\rho\downarrow$. The dominant part is the exchange potential V_x, which is proportional to $-\rho_{\uparrow}^{1/3}$ and $-\rho_{\downarrow}^{1/3}$ for majority and minority spin wavefunctions respectively. Different magnetic structures, such as paramagnetic, ferromagnetic and various antiferromagnetic configurations, exhibit different total energies, and the lowest-energy configuration obtained by local density theory represents the observed magnetic state in most cases (figure 16) (Moruzzi *et al.* 1978, 1986, 1989, Moruzzi

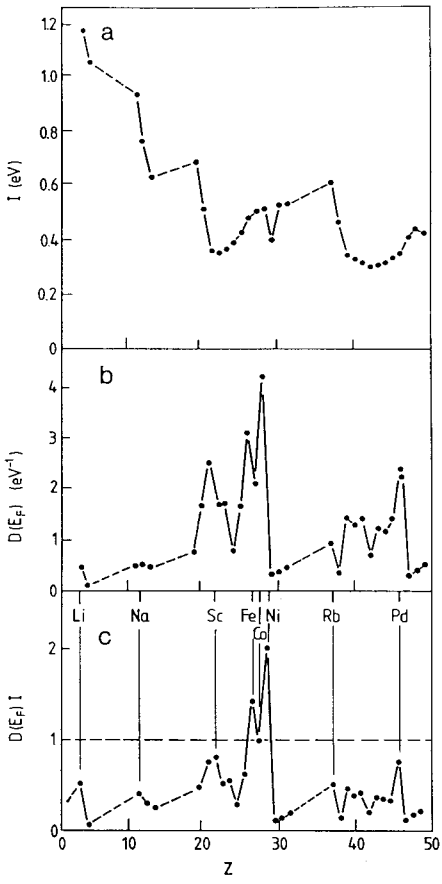

Figure 17. The Stoner criterion for ferromagnetism. The two important factors are (*a*) the density $D(E_F)$ of states at the Fermi level (per spin and atom) shown and (*b*) an atomic exchange integral I shown. (*c*) Their product has to be larger than unity to drive the transition to ferromagnetism (Janak 1977) (adapted from Ibach and Lüth (1993)). Elements marginally below the criterion can become ferromagnetic in thin films and multilayers, where the density of states is enhanced by band narrowing.

and Marcus 1992) (for the delicate situation near the ground state of Fe see Körling and Ergon (1996)).

Ferromagnetism occurs in rather few elements, Fe, Co, Ni, Gd and a few rare earths with low Curie temperatures (many fewer than superconductors!). The stability of ferromagnetism in these elements can be explained by the Stoner criterion (figure 17), which takes the density $D(E_F)$ of states at the Fermi level and an atomic exchange integral I as input (Gunnarson 1976, Janak 1977, Pettifor 1980). The transition from paramagnetism to ferromagnetism becomes favourable if

$$D(E_F) \cdot I > 1. \tag{5}$$

Then the system can lower its energy by bringing enough majority spin electrons down in energy by opening up the ferromagnetic exchange splitting. As with the opening of a gap in superconductivity, the density of states at the Fermi level and a coupling parameter (here the exchange integral I) are the critical quantities. The

Stoner criterion explains why Fe, Co and Ni are singled out for ferromagnetism. several other elements are close to fulfilling the criterion, for example Pd. In some thin-film structures these elements are transformed into ferromagnets, for example V, Cr, Mn, Mo, Ru, Rh, Pd and Pt (see section 4.1). Magnetism can either be induced by exchange coupling to a ferromagnetic substrate or occur spontaneously owing to a higher density of states in a monolayer, caused by reduced bandwidth (see section 5.2).

Antiferromagnetism is also driven by a large density of states at the Fermi level, but in this case at specific points in **k** space that are related to the antiferromagnetic reciprocal-lattice vector (Fawcett 1988). The antiferromagnetic ordering opens a bandgap E_g at these **k**-points that lowers the energy of the occupied states at the bottom of the gap and removes the high density of states from the Fermi level. Again, one discovers similarities with the opening of a gap in superconductivity. In fact, antiferromagnetic order in Cr can be mapped onto the superconducting order parameter to a certain approximation. The Bardeen–Cooper–Schrieffer theory of superconductivity then produces a relation between critical temperature and gap E_g:

$$E_g \approx 3.5 k T_{\text{Neel}}. \tag{6}$$

This relation is only a rough guide, as the case of Cr shows, where a Néel temperature of 311 K and a gap of 0.13 eV give $E_g \approx 5 k T_{\text{Neel}}$.

At elevated temperatures it becomes rather difficult to calculate magnetic properties from first principles, particularly the *Curie and the Néel temperatures*. The complex time-dependent magnetic microstructure near the critical temperature presents a formidable challenge. In the atomic limit, for example using the Heisenberg model, one assumes a magnetic moment on each atom that persists beyond T_C. The magnetization vanishes by orienting the moments at random in the paramagnetic phase. The other extreme, that is the Stoner model of band-like ferromagnetism, assumes that the magnetic moment gradually decreases at elevated temperature and vanishes above T_C. It gives Curie temperatures twice as high as observed (Pettifor 1980). The basic flaw is the assumption that the magnetic order disappears by spin-flip excitations across the Stoner gap Δ (see section 3.1.2). They cost more energy than is actually needed to disorder magnetic moments. More realistic models contain small domains with local order whose orientations are starting to fluctuate when approaching the Curie temperature T_C. Some degree of local correlation remains even above T_C. Such a picture brings in spin-wave excitations (magnons) which are not contained in the ground-state energy bands. recent efforts to model the spin structure just below and above the Curie point from first principles give qualitatively correct Curie temperatures (Uhl and Kübler 1996). At surfaces, an increased T_C becomes possible owing to the higher density of states at the Fermi level. In thin films, T_C generally decreases owing to fewer magnetic neighbours (see sections 4 and 5).

The *magnetic moment* is dominated by the electrons with high angular momentum, the 3d electrons in Cr, Mn, Fe, Co, Ni and the 4f electrons in the rare earths. With increasing atomic volume, one approaches the free-atom limit where Hund's first rule postulates maximum spin, that is all the individual spins of the electrons in a shell are aligned parallel. Electrons with parallel spin have different spatial wavefunctions, owing to Pauli's exclusion principle which is reflected in the exchange interaction. That reduces their Coulomb repulsion. When the atoms are squeezed into a solid, some of the electrons are forced into common spatial wavefunctions

which forces their spins antiparallel and reduces the overall magnetic moment. For example, the moment of $5\mu_B$ in the free Cr atom is reduced by an order of magnitude in the solid. Figure 16(*a*) shows how the magnetic moment of fcc and bcc Fe decreases in local density calculations when the atomic volume is reduced. At surfaces and interfaces, and in thin films the atomic volume is able to expand, which allows part of the atomic moment to be recovered. This type of enhanced surface magnetism will be discussed in section 5.2.

Another consequence of the volume-dependent magnetic moment is *magnetostriction*, that is, a change in the magnetization with strain and vice versa. This effect severely affects the functioning of magnetic devices as they become smaller and are able to sustain ever higher strain. Therefore magnetic devices are often composed of alloys with zero first-order magnetostriction, such as permalloy ($Ni_{0.8}Fe_{0.2}$) or analogous ternary compounds (along the line $Ni_{0.8}Fe_{0.2}$–$Ni_{0.65}Co_{0.35}$ and along $Ni_{0.25}Co_{0.3}Fe_{0.45}$–$Ni_{0.05}Co_{0.9}Fe_{0.05}$ (Miyazaki *et al.* 1994)). In strained epitaxial layers the magnetic ordering may change completely, for example from ferromagnetic to antiferromagnetic in thin Fe films on Cu(100) (figure 16; compare section 4.1).

Magnetic coupling between spins on different atoms determines the magnetic order, for example ferromagnetic as against antiferromagnetic in bulk solids. Magnetic multilayers exhibit analogous configurations, where the magnetizations of two layers lie parallel or antiparallel to each other, while each layer exhibits ferromagnetic order internally (figure 15(*b*)). The overall magnetic configuration can be analysed by breaking the magnetic energy up into pairwise interactions. The lowest-order term is bilinear in the magnetic moments $\mathbf{M}_i$ of individual atoms:

$$E_1 \propto -\sum J_1(\mathbf{r}_{ik})(\bar{\mathbf{M}}_i \cdot \bar{\mathbf{M}}_k), \qquad \bar{\mathbf{M}} = \frac{\mathbf{M}}{|\mathbf{M}|}. \tag{7a}$$

The coupling constant J_1 strongly depends on the distance $\mathbf{r}_{ik}$ between atoms.

For distances close to an atomic spacing the direct exchange interaction dominates. A typical case is fcc Fe in figure 16(*b*) (full curves). At the shortest interatomic distances r_{ws} the non-magnetic state (curve NM) is most stable, then the antiferromagnetic state (curve AF) takes over with increasing r_{ws}, and eventually the ferromagnetic state (curve HS) becomes favourable at the largest r_{ws}. Qualitative arguments are able to rationalize this behaviour: when highly compressed, electrons are forced into similar spatial wavefunctions with opposite spin to satisfy Pauli's exclusion principle. That reduces the magnetic moment and eliminates it altogether at the shortest distances (figure 16(*a*), full curves). The antiferromagnetic coupling at intermediate distances can be viewed as the exchange hole carried by an electron, which excludes parallel spins from its neighbourhood. At larger distances, electrons are able to reduce their Coulomb repulsion by occupying different spatial wavefunctions with equal spins.

An indirect exchange interaction takes over at distances beyond a few atomic spacings. It is mediated by the s, p electrons. Spin *i* polarizes the s, p-electron gas and a second spin *k* feels the induced polarization. This interaction starts out ferromagnetic at small distances and oscillates with a period of $\lambda_F/2$, where $\lambda_F = 2\pi/k_F$ is the Fermi wavelength and k_F is the Fermi wave-vector. The ferromagnetic coupling at small distances follows from a symmetry argument. Both spins interact in the same way with the s, p electrons, such that one has either a $\uparrow\downarrow\uparrow$ or a $\uparrow\uparrow\uparrow$ spin configuration. The oscillatory behaviour at larger distances arises because the s, p-electron gas responds to an extra spin by setting up a static spin wave. This wave contains spatial

frequencies up to the wave-vector $2k_F$, which is the largest wave-vector of zero-energy excitations across a spherical Fermi surface. In real space, the occupied states contain wavelengths from infinity down to λ_F. Charge and spin density are given by the square of the wavefunction, which oscillates with $\lambda_F/2$, twice as fast as the wavefunction itself. This indirect coupling via the s, p electrons is described to lowest order by the Ruderman–Kittel–Kasuya–Yosida (RKKY) interaction (see Majkrzak *et al.* 1991 for the prototype rare-earth superlattices and section 5.4 for transition and noble metals). In order to obtain the magnetism of a bulk solid, one has to integrate over couplings between atom pairs in all directions and at many distances. Thus RKKY oscillations tend to become averaged out. In well defined layer structures, however, they remain visible and produce an oscillatory magnetic coupling (section 5.4). The sum in equation (7*a*) is often simplified by dropping weaker couplings at larger distances. In the limit of retaining only nearest-neighbour terms, one arrives at the Heisenberg, the *xy* or the Ising model, depending on whether the magnetic moment vectors **M** have three, two or one degree of freedom. These are important for classifying magnetic phase transitions (section 4.2).

Higher-order magnetic couplings are starting to be observed in small structures, particularly where the lowest-order J_1 term in equation (7*a*) goes through zero during one of the RKKY oscillations. The next term is the biquadratic coupling:

$$E_2 \propto + \sum J_2(\mathbf{r}_{ik})(\mathbf{M}_i \cdot \mathbf{M}_k)^2, \qquad \bar{\mathbf{M}} = \frac{\mathbf{M}}{|\mathbf{M}|}. \tag{7b}$$

It varies as $\cos^2 \vartheta$ with the angle ϑ between two moments $\mathbf{M}_i$ and $\mathbf{M}_k$ and thus exhibits energy minima either at $\pm 90^\circ$ (J_2 positive) or at 0° and 180° (J_2 negative). The ordinary bilinear coupling in equation (7*a*) exhibits either a minimum at 0° (J_1 positive; ferromagnetism) or at 180° (J_1 negative; antiferromagnetism) but cannot explain 90° coupling. The 90° coupling has been found in thin-film systems, such as Fe/Cr(100) when the film thickness is adjusted to the point where J_1 switches from ferromagnetic to antiferromagnetic (Slonczewski 1993).

At distances larger than about 10 nm the magnetostatic dipole interaction takes over from the exchange coupling and orients particles or layers as if they were macroscopic bar magnets (compare figure 15(*c*)).

Magnetic anisotropy is another magnetic variable that becomes rather volatile as the bulk symmetry is reduced in small structures. In general, the magnetic energy density E varies quadratically with the angle ϑ of the magnetization with respect to a symmetry axis in a crystal or film:

$$E = K \cos^2 \vartheta. \tag{8}$$

The anisotropy constant K can be negative ('easy' axis) or positive ('hard' axis). If K vanishes by symmetry, such as in a cubic environment, fourth-order terms in ϑ take over. A variety of phenomena cause anisotropy, which may be grouped into crystalline and dipole anisotropy. The source of crystalline bulk anisotropy is the spin–orbit interaction. While atomic spin wavefunctions are isotropic by themselves, they become tied to the crystal lattice by spin–orbit interaction. Therefore the total magnetic moment (spin plus orbital moment) is coupled to the crystal axes. For the common ferromagnetic materials the easy axes are [100] in bcc Fe, [0001] in hcp Co, [111] in fcc Ni, and [0001] in hcp Gd. In nanostructures the symmetry of the system is lowered by the existence of a surface or interface, where orbitals perpendicular and parallel to the interface become inequivalent. This symmetry breaking propels the

anisotropy from a fourth-order effect to a second-order effect in Fe and Ni. Some surfaces exhibit an additional in-plane anisotropy, which can be intrinsic, for example for (110) surfaces of fcc and bcc structures, or step induced. If there is lattice mismatch between a magnetic layer and the substrate, one encounters a magnetoelastic anisotropy which is related to magnetostriction. The second major source of anisotropy is the magnetic dipole interaction, which can be viewed as the energy density $E = -\frac{1}{2}\mathbf{M}\cdot\mathbf{H}_d$ of the magnetic moment $\mathbf{M}$ in the demagnetizing field $\mathbf{H}_d$. This shape anisotropy becomes important in thin films ($K_{dipole} = -2\pi M^2$) and for wires ($K_{dipole} = -\pi M^2$), where it aligns the magnetization to the plane of a thin film or to the axis of a wire. For the analysis of the magnetic data in thin films, the bulk expression for magnetocrystalline anisotropy K_{bulk} has to be augmented by a thickness-dependent term $K_{interface}/d$, which describes surface, interface and strain-induced contributions to the magnetic energy density, averaged over the thickness of the film (Heinrich and Cochran 1993). To this first approximation, the bulk terms are independent of thickness, while the surface and interface terms decrease in relative weight as the film becomes thicker. However, the bulk contribution is not necessarily independent of thickness either, since strain and alloying with the substrate may be thickness dependent. An example is the double transition from parallel to perpendicular and back to parallel, observed in Ni films on Cu(100) with increasing thickness (Schulz and Baberschke 1994, O'Brien *et al.* 1996). The Ni film is magnetized parallel to the surface up to seven atomic layers, driven by surface, interface and shape anisotropy. Between seven and about 40 monolayers, the magnetization orients itself perpendicular, along the axis preferred by the strained Ni film. Above the critical thickness of about 40 monolayers, the Ni film begins to relax into the bulk Ni structure, which is isotropic to second order. Therefore the shape anisotropy takes over again and forces the magnetization parallel to the film.

Thin films often exhibit a competition between the shape anisotropy, which wants to orient the moment parallel to the surface, and the crystalline anisotropy (for an overview see Pappas (1996)). The crystalline anisotropy often favours a magnetization perpendicular to the surface (Néel 1954, Daalderop *et al.* 1994, Wang *et al.* 1994). A simple estimate of the relative strengths shows that with decreasing film thickness the interface anisotropy will eventually dominate, because its energy density scales like $1/d$. This explains a frequently observed switch from parallel to perpendicular magnetization in epitaxial films below about five monolayers coverage, for example in bcc Fe on Ag(100) and fcc Fe on Cu(100) (compare section 4 and figure 20).

Two-dimensional magnetism in thin films is dependent on the presence of anisotropy in a rather general fashion, because long-range magnetic ordering occurs only for the uniaxial Ising model, whereas an isotropic Heisenberg system cannot establish long-range order at finite temperatures (Mermin and Wagner 1966) (see section 4.2).

Steps have a strong influence on the anisotropy, which will be discussed in section 6.

3.2.2. *Charge and spin transport: magnetoresistance*

In order to understand magnetic transport phenomena, such as magnetoresistance, spin-polarized tunnelling, and the spin transistor we have to know the *electronic carriers* of charge and spin in magnetic materials (Prinz 1995). It is clear that the relevant electronic states have to lie close to Fermi level, for example a few

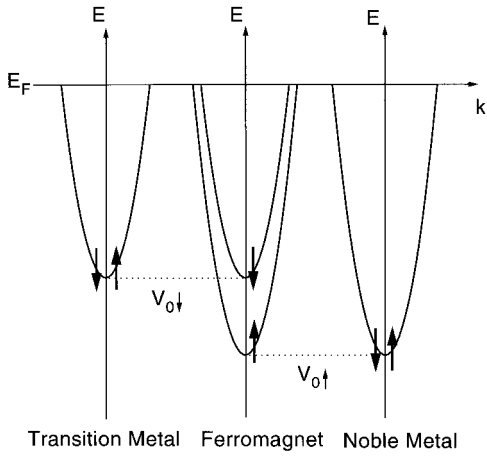

Figure 18. Greatly simplified view of the energy bands contributing to magnetic coupling, transport and quantum confinement at the Fermi level E_F. The s, p band sections that hybridize with the $3d_{z^2}$ states near the Fermi level (highlighted in figure 11) are approximated by free-electron parabolae in a potential V_0.

kT in conductance, and a few tenths of an electronvolt in planar tunnelling through insulators, vacuum tunnelling and field emission, depending on the barrier height (Alvarado 1995). Beyond that there is no obvious answer. Are these the s,p electrons or the d electrons? Are they majority spin or minority spin? The argument for transport by s, p electrons is based on the high group velocity dE/dp of the steep s, p band (see figure 11). The d bands are flat, with a low group velocity and a high effective mass. The density of states at the Fermi level, on the other hand, is smaller for the s, p band than for the d bands. To estimate the spin polarization of the current one could argue that the minority spin d electrons dominate the total density of states at the Fermi level, at least in Ni and Co where the majority spin d bands are full (Fe has majority spin polarization at E_F). However, the s, p electrons tend to be magnetized opposite to the d electrons, albeit much less (only about 10% of the total moment; see section 3.1.2). They always exhibit majority spin polarization at the Fermi level since the s, p Fermi surface is larger for majority spin due to the larger band filling, not only for Ni and Co but also for Fe (see figures 11 and 18). To complicate the issue further, one may note that in Ni and Co the spin polarization at the Fermi level is opposite to the energy-integrated overall moment. Minority d states dominate at E_F whereas the overall spin polarization is, of course, majority. For s, p states the same holds in reverse.

Taking realistic energy bands, the distinction between *s, p and d states* becomes blurred. They hybridize since the spherical symmetry of the atom is broken by the **k** vector, leaving only the point-group symmetry. Even along high-symmetry directions there is mixing, for example, between s, p_z and d_{z^2} states in the Δ_1 band that crosses the Fermi level along the [100] direction in fcc and bcc structures (figures 11 and 18). The steep section of this band (bold in figure 11) is usually labelled the s, p band because it tracks a free-electron parabola for a significant portion of **k** space. At the Γ point the character of the Δ_1 band is mostly d like, with a large exchange splitting δE_{ex} and flat bands, whereas it becomes s, p like with small δE_{ex} and large dispersion at the Brillouin zone boundary. The Fermi level lies in between, giving the band a highly mixed character. A quantitative projection onto the different angular

momenta produces about three to four times as much d character as s, p for the 's, p band' (taking the character of the majority spin states at E_F in Ni and Co from Papaconstantopoulos 1986). Therefore the *s, p band* has been occasionally labelled an itinerant d band (d_i) (Stearns 1977). It dominates *conductivity and tunnelling* (see below and section 5.5) and also determines magnetic coupling across layers (sections 5.3 and 5.4). A parabolic approximation to the s, p band is often used to describe these phenomena (compare figure 18 and section 3.2.2). The *d bands* make their presence felt via *scattering*. They determine the lifetime and mean free path of s, p carriers at the Fermi level. Minority spin electrons are scattered more strongly, leaving majority spin s, p electrons as the principal carriers. The reason for the strong *minority spin scattering* is the high density of minority spin d-states at the Fermi level in Ni and Co, combined with a spin-conserving electron–electron scattering process (compare section 5.5).

In other types of experiment, such as photoemission and inverse photoemission, the weight can be shifted from s, p to d bands and back. For example, s, p bands dominate at low photon energies (below 10 eV) and d bands at higher energies (Ortega and Himpsel 1993, Mankey *et al.* 1994). f states in rare earths turn on at higher energies yet (above 30 eV). These cross-sections are determined by the match between the wavelength of the photoelectron and the radius of the orbital (for a tabulation—see Yeh and Lindau 1985). Higher-angular-momentum states have a smaller radial quantum number and thus require shorter-wavelength photoelectrons for a match.

Magnetoresistance, that is a change in the resistivity under the influence of a magnetic field, has generated rapidly growing attention. As the capabilities of producing tailored materials have grown, the effect as well as the terminology has become inflated, starting with anisotropic magnetoresistance (AMR), a 2% effect in Permalloy ($Ni_{0.8}Fe_{0.2}$), processing to giant magnetoresistance (GMR), a 200% effect in multilayers, and currently peaking with colossal magnetoresistance (CMR), which gives a factor of 10^5 in magnetic perovskites. Even the traditional, bulk magnetoresistance (Pippard 1989) can take on dramatic values in ultrapure metals at low temperatures, for example an increase by a factor of 10^8 at 1 T in Mg. The direct connection between magnetism and electrical properties makes this phenomenon ideal for magnetic sensors (section 8.2). Various physical phenomena lead to the different kinds of magnetoresistance. They may produce an increase in the resistance in a magnetic field (positive magnetoresistance, e.g. in AMR and in metals at low temperatures), as well as a decrease (negative magnetoresistance, e.g. in GMR, CMR and magnetic tunnelling). Hysteretic behaviour has also been observed as in GMR and spin-polarized tunnelling. Positive magnetoresistance in pure metals at low temperatures can be attributed loosely to the longer effective path of electrons as they travel along helical paths around the magnetic field lines. Electrons moving perpendicular to the field lines are affected the most, leading to a maximum in the resistance along this direction. AMR occurs at room temperature, where the mean free path is much too short for a helical orbit (Thompson *et al.* 1975, Hong and Giordano 1995). It leads to a maximum in the resistance parallel to the magnetization, not perpendicular. The majority spin s, p electrons that dominate conductivity are scattered more strongly when propagating parallel to the magnetization direction and less when moving perpendicular to it. This effect is currently used for magnetic reading heads in data storage (section 8.2). GMR produces a decrease in the resistance in magnetic–non-magnetic–magnetic multilayers when consecutive mag-

netic layers with antiparallel magnetic orientation are forced parallel by an external field. It can be rationalized by an optical analogue; each interface acts as a polarizer for electrons. The parallel magnetic orientation corresponds to parallel polarizers, whereas the antiparallel orientation is represented by crossed polarizers. A similar decrease in resistance is produced by spin-dependent tunnelling in ferromagnet–insulator–ferromagnet junctions when the magnetic orientation is forced from antiparallel to parallel. The key to the resistance change is the injection of majority spin s, p electrons at the Fermi level into empty majority states on the other side of the junction. GMR and magnetic tunnelling depends on the existence of interfaces in a multilayer structure with nanometre thickness. Therefore it is explained in more detail in the context of electronic states in thin films (section 5.5). The cause of the CMR effect in perovskites is still under investigation. A characteristic feature of these materials is a phase transition from a semiconductor at high temperatures to a ferromagnetic metal at low temperatures. An external field affects this transition and causes a distinct maximum in the magnetoresistance near the transition temperature. The key role is played by electrons hopping between spin-polarized Mn^{3+} and Mn^{4+} ions (Prinz 1995). In order to obtain the full resistance change, one generally needs fields of several tesla.

3.2.3. *Experimental techniques: microscopies*

Magnetic measurements can be performed on small quantities of magnetic materials by a wide variety of experimental methods (for an overview see Falicov *et al.* (1990) and McWhan (1994)). Traditional bulk techniques, such as neutron, X-ray and Brillouin scattering, need relatively thick superlattice structures to obtain sufficient signal. Neutrons have been sued to map the elaborate spin structures of rare-earth superlattices (Borchers *et al.* 1988) and Fe/Cr multilayers (Schreyer *et al.* 1995). The scattering intensity I is determined by the vector product of the momentum transfer $\mathbf{q} = \mathbf{k}' - \mathbf{k}$ and the Fourier component $\mathbf{M}(\mathbf{q})$ of the magnetization (Fawcett 1988):

$$I(\mathbf{q}) \propto \left|\mathbf{M}(\mathbf{q}) \times \bar{\mathbf{q}}\right|^2, \qquad \bar{\mathbf{q}} = \frac{\mathbf{q}}{\left|\mathbf{q}\right|}. \tag{9}$$

Magnetic X-ray scattering (McWhan 1994) is generally a very weak effect but can be enhanced by resonances at core level absorption edges, which also makes the process element specific. By using circularly polarized light and taking the difference between opposite magnetization directions, the magnetic roughness of interfaces can be determined (MacKay *et al.* 1996). Brillouin scattering probes spin waves but can also be used to obtain magnetization, magnetic coupling, and anisotropy by modelling the magnon dispersion curves (Grünberg 1989, Krams *et al.* 1992). Quite a few magnetometry techniques have become sensitive enough to detect monolayer quantities, for example the superconducting quantum interference device (SQUID) magnetometer, the torsion magnetometer (Gradmann and Przybylski 1987) and the alternating-gradient magnetometer (Turtur and Bayreuther 1994). Magnetic anisotropy can be determined by angle-resolved magnetic resonance (Heinrich and Cochran 1993). Apart from these direct methods there are a number of indirect techniques for measuring magnetization in thin films. Conversion electron Mössbauer spectroscopy measures the hyperfine field (Shinjo 1991), which is related but not directly proportional to the magnetization. Magneto-optical techniques produce signals related to the magnetization. They are very useful for obtaining hysteresis

loops but difficult to calibrate in absolute units. A popular method is the surface magneto-optic Kerr effect (SMOKE) which measures the rotation of the polarization when light is reflected off a magnetized surface (Bader 1990). It comes in several varieties: polar, longitudinal and transverse. The signal is largest when the electric field of the light is perpendicular to the magnetization (Falicov 1993). Thereby, in-plane magnetization is probed by the longitudinal Kerr effect and perpendicular magnetization by the polar effect. The Kerr signal of a monolayer originates from a small fraction of the optical penetration depth in metals (10–20 nm) and thus is rather small (a fraction of a degree rotation). Surface sensitivity and Kerr rotation can be enhanced dramatically by going to the nonlinear Kerr effect, where the rotation in the second harmonic of a pulsed laser is measured (Rasing *et al.* 1996, Straub *et al.* 1996). Second-harmonic generation requires a breakdown of the inversion symmetry, which only happens at a surface or interface in centrosymmetric crystal structures. Other magneto-optic techniques probe the change in absorption of linearly or circularly polarized light when the sample magnetization is reversed. The most common method is magnetic circular dichroism (MCD), applied to transitions from a core level to magnetic valence states just above the Fermi level (Rudolf *et al.* 1992, Stöhr 1995, Schütz *et al.* 1997). It can be used in conjunction with approximate sum rules (de Groot 1994, Wu *et al.* 1994b) to obtain the orbital and spin moment of a specific element from the two spin–orbit split components of a core level absorption edge. Inherently surface-sensitive probes are based on spin-polarized electrons. Spin-polarized secondary-electron emission is particularly useful for surface magnetization measurements (Falicov *et al.* 1990, Scheinfein *et al.* 1990, Siegmann 1992, Allenspach 1994).

Magnetic microscopes are essential to detect the magnetic domain structure. Domains at the submicrometre level have to be resolved to analyse today's magnetic storage devices with bit sizes of $0.1 \times 5\,\mu m$. Likewise, such small domains need to be resolved to understand the micromagnetic behaviour near phase transitions. the following gives a brief tour through the large variety of magnetic microscopes, proceeding roughly towards increasing spatial resolution. Direct magnetic measurements with small SQUID detectors integrated onto a Si chip can provide very sensitive magnetic maps. For example, single flux quanta are easily detected (Ketchen and Kirtley 1995). Optical microscopes can be adapted to produce a contrast based on the Kerr rotation of linearly polarized light reflected off domains with different magnetization (Schmidt *et al.* 1985, Trouilloud *et al.* 1994). The diffraction limit of the resolution is about 500 nm, but it can be overcome by near-field scanning optical microscopy, where evanescent light from a narrow capillary scans the sample (Betzig *et al.* 1992). Magnetic imaging with circularly polarized light has produced images with about 100 nm resolution (Levy *et al.* 1996). Another scanning probe is magnetic force microscopy (MFM), which measures the force that the magnetic stray field of the surface exerts onto a small magnetic tip. The magnetization is probed indirectly via the magnetic poles of the sample (Lederman *et al.* 1994, Proksch *et al.* 1994, New *et al.* 1995a, b, Hehn *et al.* 1996, Hug *et al.* 1996) (see also figure 51 in section 8). Thereby it is possible to detect local magnetization on a scale of 10–50 nm. The force can be detected in a static mode via the deflection of a cantilever, which can be measured very accurately by a laser beam reflected off the cantilever into a split diode. Surface and tip interaction limit the resolution in this static contact mode. New non-contact techniques, where the shift in the resonance frequency of an oscillating cantilever is measured, have produced atomic resolution

on Si surfaces and raise hopes for high-resolution magnetic imaging. Recent developments in magnetic resonance force microscopy promise additional chemical information (Zhang *et al.* 1996).

Electron-based microscopes push the resolution further. Secondary-electron microscopy with polarization analysis (SEMPA) measures the spin polarization of secondary electrons emitted from a magnetized sample (about 20 nm resolution) (Pierce *et al.* 1989, Scheinfein *et al.* 1990, Allenspach 1994) (see also figure 50 in section 8). In low-energy electron microscopy (LEEM) and photoemission electron microscopy (PEEM), low-energy electrons emitted from a surface are accelerated to about 20 keV and then are imaged through a conventional electron lens system. Magnetic contrast is obtained by using spin-polarized electrons in LEEM (Grzelakowski *et al.* 1994, Duden and Bauer 1996), or by using circularly polarized light in PEEM (Stöhr *et al.* 1993). A resolution of 20 nm has been achieved in LEEM, and 300 nm in PEEM. In PEEM, the broad energy spectrum of photoelectrons limits the resolution when combined with the chromatic aberration of the electron optics. Improved electron optics should be able to improve the resolution by an order of magnitude. Particularly interesting is the inclusion of reflecting electron optics, which have opposite spherical and chromatic aberrations compared with transmission optics and thus are able to compensate the aberrations (Rempfer and Mauck 1992). The highest resolution is achievable by high-energy electron microscopes, for example in Lorentz microscopy where the deflection of the beam in an electron microscope by magnetic domains is detected. Several reflection and transmission techniques have been tried, some of which measure the magnetization, and others its spatial derivative (Falicov *et al.* 1990, Runge *et al.* 1996) (for the holographic version that can measure flux quantitatively, see Beeli *et al.* 1995). A resolution of 2 nm can be achieved.

The ultimate magnetic microscope would be a scanning tunnelling microscope with a tip emitting spin-polarized electrons (Wiesendanger *et al.* 1990, Alvarado and Renaud 1992, Shvets *et al.* 1992, Vásquez de Parga and Alvarado 1994, Alvarado 1995, Mukasa *et al.* 1995, Wiesendanger *et al.* 1997). So far, it has been difficult to obtain spin contrast in STM on a routine basis. A possible explanation is the localized nature of the spin-polarized d and f electrons which prevents overlap between the magnetic states on tip and sample. The dominant part of the tunnel current is carried by the delocalized s, p states, which are only weakly polarized. There are hopes, however, that at short tunnelling distances, that is high tunnelling currents, spin-polarized tunnelling through 3d states becomes appreciable. An increase in the spin polarization of tunnelling electrons with increasing tunnelling current up to value of 50% has been observed (Alvarado 1995). In this experiment, spin-polarized electrons tunnelling from a magnetized Ni tip into a $Ga_{1-x}Al_xAs$ surface induce bandgap luminescence with circular polarization (Alvarado and Renaud 1992). Magnetic tunnelling is also observed in planar ferromagnet–insulator–ferromagnet structures (Meservey and Tedrow 1994, Miyazaki and Tezuka 1995, Moodera and Kinder 1996). The measured spin polarization of electrons emitted from ferromagnets into an Al_2O_3 tunnel barrier is encouraging: + 40% for Fe, + 35% for Co, + 23% for Ni and + 14% for Gd. Recent observations of d-like surface states at Fe and Cr surfaces by scanning tunnelling spectroscopy (Stroscio *et al.* 1995) suggest that element-specific magnetic tunnelling measurements might be feasible. It will be critical to prepare well defined

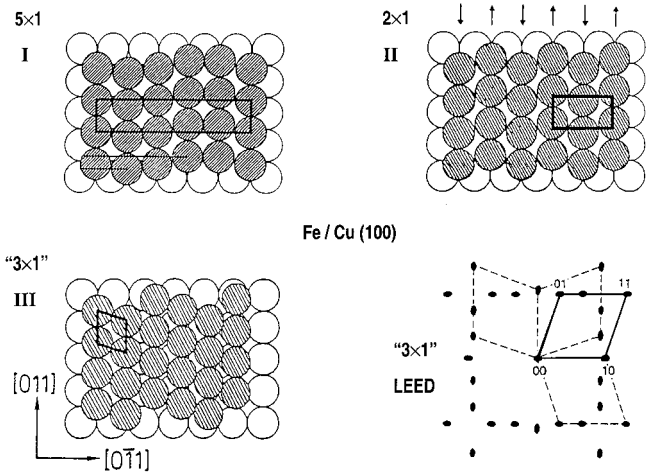

Figure 19. Structural models for Fe on Cu(100) in a top view. A continuous transition from fcc (100) to bcc (110) can be achieved by shifting the rows of a fcc (100) plane along the y axis. Three film thickness regions can be distinguished experimentally (compare figures 3 and 20). Region I: the 5×1 structure for zero to four monolayers of Fe (Landskron *et al.* 1991). Region II: the 2×1 structure for five to ten monolayers of Fe (Müller *et al.* 1995). Region III: the quasi 3×1 structure for more than 11 monolayers of Fe. Its diffraction pattern is explained by multiple bcc (110) domains in near registry with the fcc (100) surface (Wuttig *et al.* 1993a, Schmailzl *et al.* 1994).

ferromagnetic or antiferromagnetic tips and to keep the magnetic tip–sample interaction under control (Shvets *et al.* 1992).

4. Thin films

This section addresses the transition from three dimensions to two. Even though many properties of thin films can be described by three dimensional bands, or by magnetic energies that are proportional to the volume of the film, they are dramatically modified by the influence of the substrate. As the film thickness is reduced, one can ask the question when and how the transition to two-dimensional behaviour takes place. Magnetic data from thin films and interfaces have been compiled by Gradmann (1988).

4.1. *Metastable phases*

In this films it is possible to grow new crystal structures of a material by constraining them to the lattice of a single-crystal substrate. These 'artificial solids' grow to a critical thickness, where the adhesion at the interface cannot support the increasing strain any longer. It becomes energetically favourable to have small patches of the normal structure separated by misfit dislocations. Ferromagnets can be grown in several different crystal structures. Co, for example, which is hcp at room temperature, grows fcc on Cu(100) and bcc on GaAs(100) and ZnSe(100) (Prinz 1991). In order to assist with the design of epitaxial multilayers we give an overview of lattice-matched crystal structures in table 2.

The growth of fcc Fe on Cu(100) illustrates the richness of *magnetic phases* in thin-film structures (see figures 3, 16, 19 and 20). The amplitude of the RHEED oscillations in figure 3 indicates three thickness regimes with different growth modes

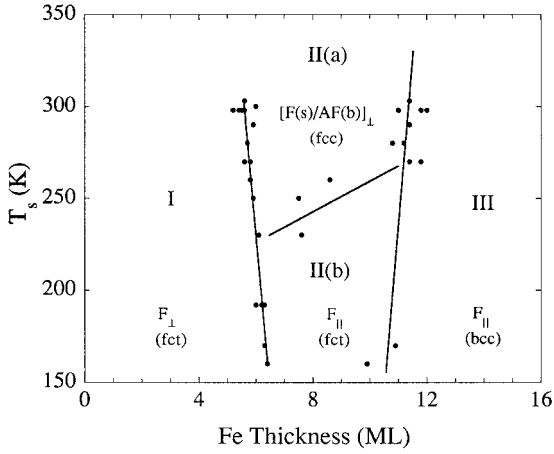

Figure 20. Phase diagram for fcc Fe on Cu(100). In region I, the film is ferromagnetic perpendicular to the surface ($F\perp$). In region IIa the surface is ferromagnetic while the underlying bulk is antiferromagnetic. In region IIB, the film is in-plane ferromagnetic. For fewer than 11 monolayers the structure is fct, a distorted fcc structure, and for more than 11 monolayers bcc (110) (compare figure 19). (From Li *et al.* 1994b.)

(Wuttig *et al.* 1993a). The boundaries lie at about four and 11 monolayers of Fe and vary somewhat in the literature owing to differences in the growth conditions and thickness calibration. Electron diffraction shows that the three regions have different surface structures, that is 4×1 and 5×1 in region I, 2×1 in region II, and quasi-3×1 in region III. Quantitative analysis gives a distorted fcc(100) structure in regions I and II (labelled fct in figure 20), and bcc(110) in region III (for region I see Müller *et al.* (1995), for region II, see Landskron *et al.* (1991); for region III see Wuttig *et al.* (1993a) and Schmailzl *et al.* (1994)). The critical thickness for the fcc to bcc conversion is 11 monolayers (2 nm). It is interesting to note that a bcc (110) plane can be obtained from the fcc (100) plane by a continuous, longitudinal shift of atom rows (along the y axis in figure 19 (c)). About every three rows the atoms are back in registry with the substrate again, leading to a quasi-3×1 diffraction pattern. Similarly, the observed $n \times 1$ patterns in regions I and II can be viewed as shifted-row structures. Kerr effect and magnetic dichroism measurements give specific magnetic characteristics for the three structural regions (figure 20). In region I, the film is ferromagnetic perpendicular to the surface ($F\perp$). In region IIa (above room temperature) the surface is ferromagnetic while the underlying bulk is antiferromagnetic. In region IIb (below room temperature), the film is in-plane ferromagnetic. In region III it is in-plane ferromagnetic (Li *et al.* 1994b). Analogous sequences are observed for other overlayer–substrate combinations (for fcc Fe(100) on various substrates see O'Brien and Tonner (1995)). These multiple magnetic structures are understandable when looking at the calculated total energy for fcc Fe in figure 16 (Moruzzi *et al.* 1986, 1989). At the lattice constant of Cu, the antiferromagnetic and ferromagnetic energy curves are just crossing each other. In addition, there are two ferromagnetic phases, a low-spin phase and a high-spin phase, upon further expansion of the lattice. The instability against bcc-like $n \times 1$ reconstructions has been demonstrated theoretically by Nordström and Singh (1996).

Band structure and exchange splitting of thin-film phases are quite different from those of the equilibrium bulk phases. The fcc and bcc structures have distinct band

topologies (compare figure 11), and the fcc and hcp structures can only be compared along the threefold direction after unfolding the hcp bands (figure 11) (Himpsel and Eastman 1980). The fcc phase of Fe has an exchange splitting of 1 eV, only half that of bcc Fe (Himpsel 1991b, Glatzel *et al.* 1992) (these data and the corresponding band structure in figure 11 are for phase II at room temperature). However, the complex magnetic structure of these films with ferromagnetic interface layers and an antiferromagnetic bulk makes a band-structure and spin analysis difficult.

Spin polarization can be induced in thin films of various 3d and 4d metals that are on the threshold of being ferromagnetic. The ordering is induced by a ferromagnetic substrate in most cases, but it may occur spontaneously in a monolayer (see section 5.2). Element-specific circular dichroism experiments have revealed ordered magnetic moments in V, Cr, Mn (O'Brien *et al.* 1994), Cu (Samant *et al.* 1994), Mo, Ru, Rh (Tomaz *et al.* 1997), Pd (Fullerton *et al.* 1995) and Pt (Schütz *et al.* 1992, 1997, Koide *et al.* 1996).

4.2. *Magnetism between three and two dimensions*

As the thickness of a film decreases, one expects to make a transition from three- to two-dimensional behaviour. To quantify this transition, for example to see whether it is abrupt or continuous, we have to find characteristics of three- and two-dimensional magnetism. Near a magnetic phase transition there exist characteristic power laws for magnetic quantities, such as the magnetization. They are described by *critical exponents* that cross over from the three- to the two-dimensional value near a certain thickness (Fisher 1974, Mills 1991). Two-dimensional magnetization curves fall off more abruptly near T_C than three-dimensional curves do. The Curie temperature itself is thickness dependent because the reduced number of neighbours in a thin film reduces the overall magnetic coupling. Again, there exists a power law and a critical exponent to describe this phenomenon in the thick-film limit (Erickson and Mills 1991). The magnetic orientation may change in thin films as well, for example from parallel to perpendicular. That changes the number of degrees of freedom and, thus, the critical exponents. Perpendicular orientation corresponds to the Ising model, in-plane orientation to the *xy* model (if isotropic) or to the Ising model (if there is a preferred in-plane axis).

The reduction of the *magnetization M near* T_C can be quantified by a critical exponent β:

$$M \propto \left(1 - \frac{T}{T_C}\right)^{\beta}, \qquad T \to T_C. \tag{10}$$

The value of β depends on the dimensionality and the number of degrees of freedom for the spin orientation, that is three for the Heisenberg model, two for the *xy* model and one for the Ising model. The predicted three-dimensional values are $\beta \approx 0.365$ for the Heisenberg model and $\beta \approx 0.325$ for the Ising model (figure 21). In two dimensions, only the Ising model exhibits true long-range order, with $\beta = \frac{1}{8} = 0.125$ given by the famous Onsager (1944) solution. The Heisenberg model does not (Mermin and Wagner 1966). The *xy* model lies in between and is able to order into a finite two-dimensional system with a critical exponent $\beta = 3\pi^2/2^7 \approx 0.23$ (Bramwell and Holdsworth 1993). Experimentally, one finds two groups of β values. One set lies close to the $\beta = 0.125$ of the Ising model and the other near $\beta \approx 0.23$ of the finite-size *xy* model. Examples for an Ising-like exponent are $\beta = 0.127$ for Fe/Pd(100) from

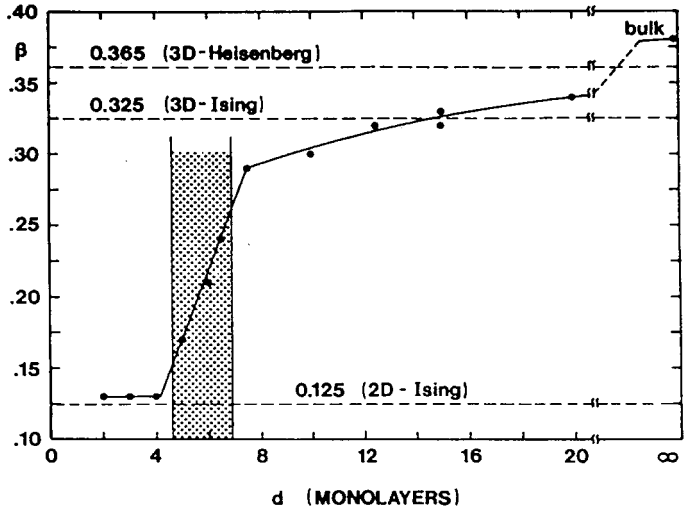

Figure 21. Transition from a three-dimensional to a two-dimensional critical exponent β in thin Ni(111) films on W(110). The exponent switches at a film thickness of about six atomic layers, indicating a rather abrupt transition from three- to two-dimensional behaviour (Li and Baberschke 1992).

Bader (1990), $\beta = 0.137$ for Fe(110)/Ag(111) from Qiu *et al.* (1991) and $\beta = 0.123$ for Fe/W(110) from Elmers *et al.* (1994). Exponents representative of the *xy* model are $\beta = 0.22$ for Fe/Au(100) from Dürr *et al.* (1989), $\beta = 0.24$ for Ni/Cu(111) from Ballentine *et al.* (1990), $\beta = 0.28$ for Ni/Cu(111) from Huang *et al.* (1994), $\beta = 0.24$ for Ni/Cu(100) from Huang *et al.* (1994) and $\beta = 0.22$ for Fe on W(100) from Elmers *et al.* (1996). It has been argued, however, that the true power law is difficult to extract because it holds only within a few per cent of T_C (Kohlhepp *et al.* 1992). There exists another way to determine the critical exponent β, that is, from the diverging line width $\delta H(T)$ of the ferromagnetic resonance near T_C:

$$\delta H(T) - \delta H(0) \propto \frac{1}{(1 - T/T_C)^{\beta}}, \qquad T \to T_C. \tag{11}$$

Figure 21 gives the result from Li and Baberschke (1992) for Ni(111) films on W(110). Here, a rather abrupt transition from the three-dimensional to the two-dimensional value is observed at a Ni thickness of about six monolayers. Huang *et al.* (1994) see a similar switch in Ni/Cu(100) between six and seven monolayers, except that the two-dimensional β is characteristic of the finite-size *xy* model instead of the Ising model. A theoretical estimate of this cross-over has been derived from the spin-wave excitation spectrum (Erickson and Mills 1991, Mills 1991). Spin waves are quantized when confined to a thin film, analogous to electron energy bands (compare section 5.3). The energy spacing between these quantized states increases as the thickness of the film decreases. When it exceeds kT, only the lowest state is thermally accessible and the system becomes two dimensional.

A second quantity characteristic of the dimensionality can be extracted from the *reduction* in T_C in thin films (figure 22). It reflects the cooperative nature of ferromagnetism, where the absence of layers on the vacuum side is felt by the deeper layers. Typically, T_C is reduced to half its bulk value at a film thickness of about five

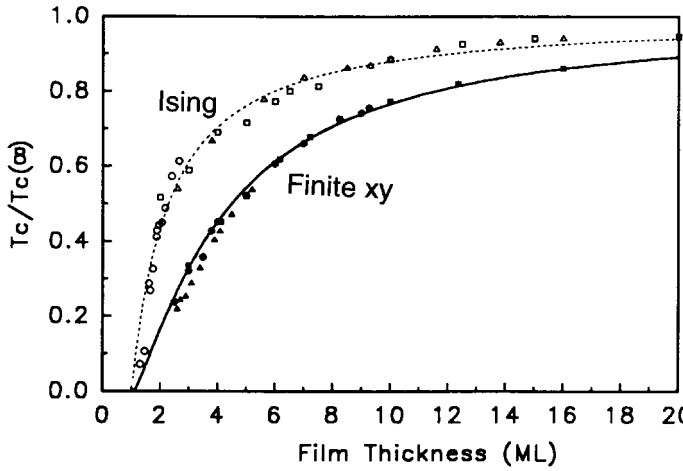

Figure 22. Decrease in the Curie temperature T_C with the number n of layers in a film, caused by the decreasing number of neighbours: (□), Ni(111)/W(110); (○), Fe(110)/Ag(111); (△), Ni(111)/Re(0001); (■), Ni/Cu(100); (●), Ni_9Co_1/Cu(100); (▲), Ni_3Co_1/Cu(100). Two classes of materials can be distinguished after normalizing T_C to the bulk value $T_C(\infty)$, one representing uniaxial Ising systems, and the other planar xy systems. T_C is reduced to half its bulk value at a thickness of about five monolayers in the xy systems and reaches zero at about one monolayer—see Huang *et al.* (1994) and references therein.

monolayers (Gradmann and Przybylski 1987, Li and Baberschke 1992, Engel *et al.* 1994, Güntherodt *et al.* 1994, Wu *et al.* 1996). A systematic analysis of this reduction comes from the theory of finite-size scaling (Domb 1973, Schmidt and Schneider 1992). The decrease in T_C with increasing thickness becomes independent of the material after normalizing it to $T_C(\infty)$, the Curie temperature of the bulk. In the limit of a large number of atomic layers n, one obtains again a power law for T_C which is characterized by a critical exponent λ, the inverse in the exponent ν for the correlation length:

$$\frac{T_C(n)}{T_C(\infty)} = 1 - \left(\frac{n_0}{n}\right)^{\lambda}, \qquad n \to \infty. \tag{12}$$

Predictions of $\lambda \approx 1.56$ and $\lambda \approx 1.49$ are obtained for the exponent from the three-dimensional Ising and xy models respectively. Below a certain thickness n_0 a film becomes paramagnetic ($T_C = 0$). The actual curves fitted to the data in figure 22 (Huang *et al.* 1994, Wu *et al.* 1996) have a different form at small n where equation (12) is not applicable. The zero crossing of T_C happens close to one monolayer. It appears that the scaled $T_C(n)$ curves of various materials in figure 22 fall into the same two classes that distinguished themselves by their β values already, that is the uniaxial Ising and the planar xy systems (Huang *et al.* 1994). The experimental exponents λ at large n are rather uncertain, but in the expected range, for example $\lambda = 1.25$-1.66 for the xy model class (Ballentine *et al.* 1990, Huang *et al.* 1994) and higher for the Ising class. Going down by one dimension, one has a transition from a monolayer to a single string of atoms. That can be achieved by producing stripes by step-flow growth at a surface with regular steps (see section 2.4 and figure 5). Experiments have been carried out for Fe/W(110) and a scaling parameter $\lambda = 1.03$ has been found in agreement with $\lambda = 1$ for the two-dimensional Ising model

(Elmers *et al.* 1994, 1995). The value n_0 where T_C vanishes corresponds to approximately four rows.

A third signature of two-dimensional behaviour is the transition from *parallel to perpendicular anisotropy* in a thin film (see section 3.2.1, figure 20). This can happen when the surface or interface anisotropy overcomes the shape anisotropy. The former scales with the surface area, whereas the latter scales with the film volume. Typically, the transition occurs at five monolayers film thickness, for example in fcc Fe/Cu(100) and bcc Fe/Ag(100) (Engel *et al.* 1991, Güntherodt *et al.* 1994, Pappas 1996). It is interesting to note that the symmetry of the spin arrangement changes from the *xy* model for in-plane magnetization to the Ising model for perpendicular magnetization. At the cross-over point, one might expect a Heisenberg-like interaction since the anisotropies are balanced. This does not happen. Instead, the film breaks up into striped magnetic domains akin to a smectic liquid crystal (Allenspach and Bischof 1992, Speckmann *et al.* 1995).

These clues from a variety of measurements suggest that magnetic films change their character from three to two dimensional at about five atomic layers thickness. To get at the underpinnings of this change we note that a five-layer critical thickness implies spin–spin interactions up to the second-nearest neighbour, that is from the centre of the film to the interface or surface. There are indications that the band structure of thin films undergoes a change at this thickness as well. Quantum well states in films thicker than five monolayers are described fairly well by a model that uses the bulk Hamiltonian with thin-film boundary conditions (see section 5.3). This approximation breaks down in thinner films since the interface atoms have different bonding partners (see figure 32).

5. Two-dimensional systems

As typical two-dimensional systems we consider surfaces, interfaces, monolayers and multilayers. The electronic and magnetic structure of surfaces is governed by *dilution*. It *enhances the magnetic moment* towards its atomic high-spin limit but also tends to *decrease the Curie temperature*, owing to the reduced interaction between fewer neighbours. Monolayers have an added interaction with the substrate, which enhances or reduces the magnetic moment, depending on whether the substrate is magnetic or not. These opposing trends produce a rich variety of magnetic phenomena, ranging from monolayers with enhanced magnetism to magnetically dead layers. Although there are many theoretical predictions of enhanced surface and monolayer magnetism, it has been difficult to fabricate the idealized structures that are assumed in the calculations. The lower symmetry at a surface or interface affects the magnetic anisotropy. For example, the in-plane d orbitals have a bond strength different from that of out-of-plane orbitals (Wang *et al.* 1994, Stöhr 1995). Surface magnetism has been reviewed by Siegmann (1992), and magnetic data from surfaces have been compiled by Gradmann 1994.

5.1. *Surfaces and interfaces*

As in the bulk, we can characterize the electronic structure of a surface by band dispersions, except that the momentum perpendicular to the surface ceases to be a good quantum number (see Himpsel 1983). The states truly specific to the surface are distinguished by their lack of interaction with bulk states, which usually requires that they are located at points in the $E(\mathbf{k}^{\|})$ diagram where bulk states of the same

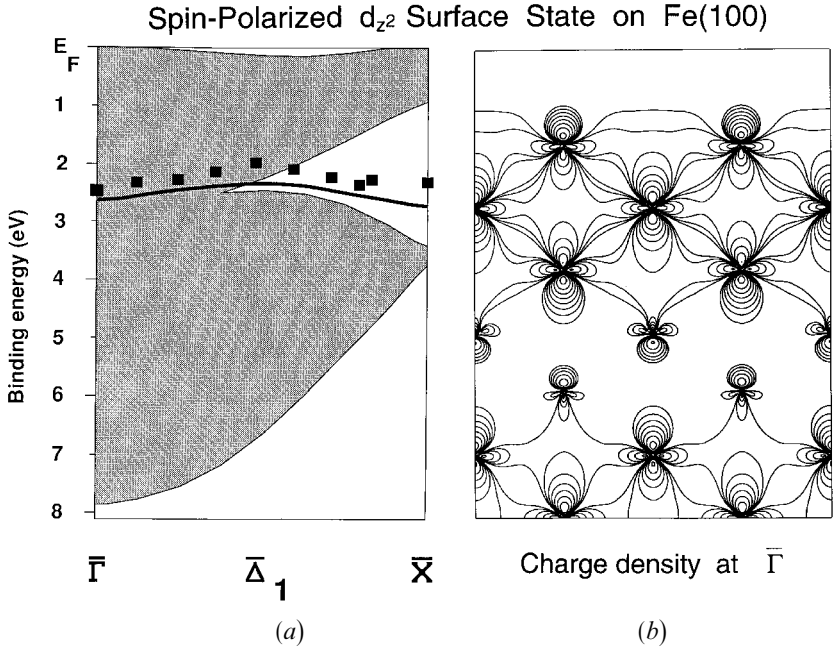

Figure 23. (*a*) Two-dimensional $E(\mathbf{k}^{\parallel})$ band dispersion of a d-like surface state with minority spin on Fe(100). The photoemission data points are superimposed on a first-principles calculation of the minority spin bands: (——), surface state: (▒), bulk bands. (*b*) A cut across the charge density perpendicular to the surface indicates d_z^2 character for the surface resonance at $\bar{\Gamma}$ (Brookes *et al.* 1990).

symmetry are absent. This is revealed in band diagrams where the $E(\mathbf{k}^{\parallel})$ band dispersions of *surface states* are superimposed on the regions of bulk bands projected along $k^{\perp}$. As in the bulk, there exist d-like surface states (figure 23) and s, p-like surface states (figures 24–26), with d states carrying most of the spin polarization in ferromagnets. Typically, the ferromagnetic exchange splitting of d states is more than twice that of s, p states.

A very basic type of s, p surface state occurs on metal surfaces. These are image states, that is electrons bound to a metal surface by their image charge and kept away from the bulk by Bragg reflection (figures 24 and 26) (for a review see Echenique and Pendry (1990)). They can be observed by two-photon photoemission (figure 26), by inverse photoemission and by scanning tunnelling spectroscopy. The $-\frac{1}{4}z$ image potential gives rise to a hydrogenic series of bound states converging towards the vacuum level, with the lowest $n = 1$ state bound by about $\frac{1}{16}$ Ryd = 0.85 eV below the vacuum level. Image states track the work function, which is the difference between the vacuum level and the spectroscopic reference level, that is the Fermi level. A broad image state peak energy signifies an inhomogeneous work function and high probability of island formation (see section 5.2 for an example). Although the image potential itself is non-magnetic, it is possible to observe a small ferromagnetic exchange splitting of image states that is induced by spin-dependent Bragg reflection at a ferromagnetic material (Donath 1989, De Rossi *et al.* 1966).

It is interesting to see how surface states are modified by adlayers. Localized d states tend to form bonding–antibonding pairs of states with nearby adsorbate orbitals. With delocalized s, p states, on the other hand, one often sees a simple

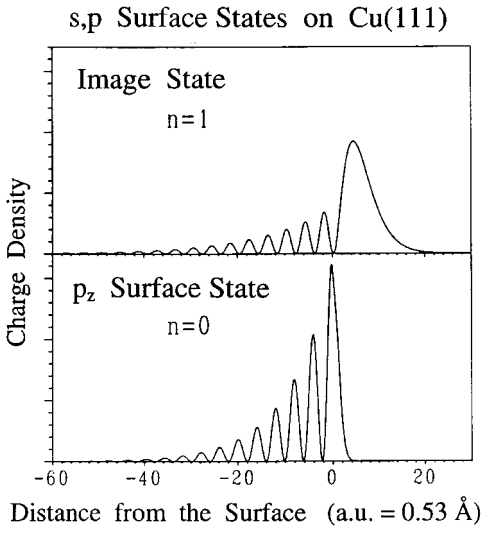

Figure 24. Two types of s, p-like surface state on transition and noble metals, exemplified on Cu(111) (Weinert *et al.* 1985). Firstly the p_z-like surface state is located near the Fermi level E_F with a charge density decaying exponentially over several lattice constants. This state is involved in figures 8, 25 and 48. Secondly the image state is located near the vacuum level E_{vac} and has its centre of gravity outside the surface. It can be seen in figures 26 and 49.

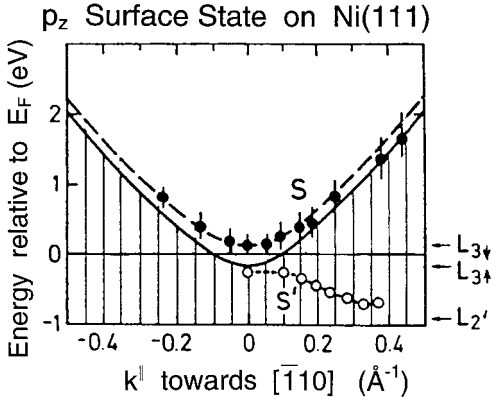

Figure 25. $E(\mathbf{k}^{\parallel})$ diagram for a p_z-like surface state on Ni(111). Two branches S and S′ are split from the combined edges of the bulk bands (▥), that is the s, p band near the $L_{2'}$ point and the 3d band near the L_3 point (Himpsel and Eastman 1978, Borstel *et al.* 1985, Donath *et al.* 1993).

energy shift of a surface state band, which represents a depletion or filling of the surface state band by electronegative or electropositive adatoms respectively. The filling of magnetic surface states is tied to the enhancement or decrease in the magnetic moment at the surface, and first attempts are being made to flesh out this correlation in a practical case (Donath *et al.* 1993). Depending on the growth mode the shift happens gradually with increasing coverage (for a lattice gas growth mode), or in a single jump with two states coexisting at incomplete coverage (two-dimensional island growth mode).

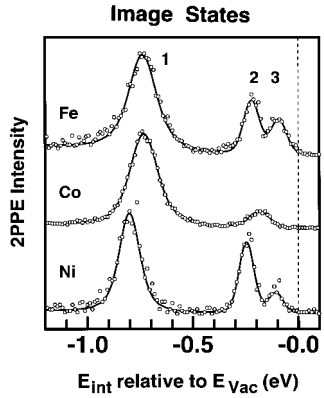

Figure 26. Observation of a hydrogenic series of image states on the densely packed Fe(110), Co(0001) and Ni(111) surfaces by two-photon photoemission (Fischer *et al.* 1992).

A well studied but still controversial case for *enhanced surface magnetism* is the Gd(0001) surface, where a surface Curie temperature 20–28 K higher than in the bulk has been reported (Tang *et al.* 1993, Weller *et al.* 1995). As a consequence, one has a ferromagnetic surface layer on top of a paramagnetic bulk between the two critical temperatures. It has been argued, however, that this enhancement is due to a complex film morphology and is not present in flat films (Donath *et al.* 1996). This surface exhibits a well pronounced spin-polarized surface state that straddles the Fermi level (Mulhollan *et al.* 1992, Li *et al.* 1994a, Donath *et al.* 1996). The magnetic Gd 4f states are shifted at the surface as well (Ortega *et al.* 1994). The Cr(100) surface might have an enhanced moment, giving it a ferrimagnetic character together with the antiferromagnetic bulk (Klebanoff *et al.* 1985). Such enhanced moments are predicted for the surface layer of many ferromagnets (Freeman and Wu 1991). A candidate for a ferromagnetic surface on a paramagnetic bulk material is Rh(100) (Wu *et al.* 1994b).

Magnetic *interface states* are conceptually similar to surface states (for examples see Houston *et al.* (1988), Weber *et al.* (1992) and Rader *et al.* (1994)). They are important for perpendicular anisotropy (Daalderop *et al.* 1994, Engel *et al.* 1994, Wang *et al.* 1994, Stöhr 1995). The two ingredients determining the sign of the anisotropy are the difference between the 3d energies of the atoms on both sides of the interface and the relative strength of in-plane bonds as against bonds across the interface (Wang *et al.* 1994). Heavy interface atoms with large spin-orbit interaction, such as Ir, Pt and Au promote strong perpendicular anisotropy. Interfaces also govern spin-dependent electron reflectivity and confinement of electrons (sections 5.3–5.5) (Hwang and Himpsel 1995, Li *et al.* 1995b).

5.2. *Monolayers*

To start out with a conceptually simple system, we initially consider free-standing and weakly bonded monolayers. The effects of bonding to the substrate will be included later. When a solid is spread out into a monolayer, one expects an increase in the magnetic moment for materials with a nearly half-filled d shell, for example V, Mn, Cr and Fe. They approach the dilute atomic limit where the magnetic moment is maximized according to Hund's first rule. The underlying physics is Pauli's principle

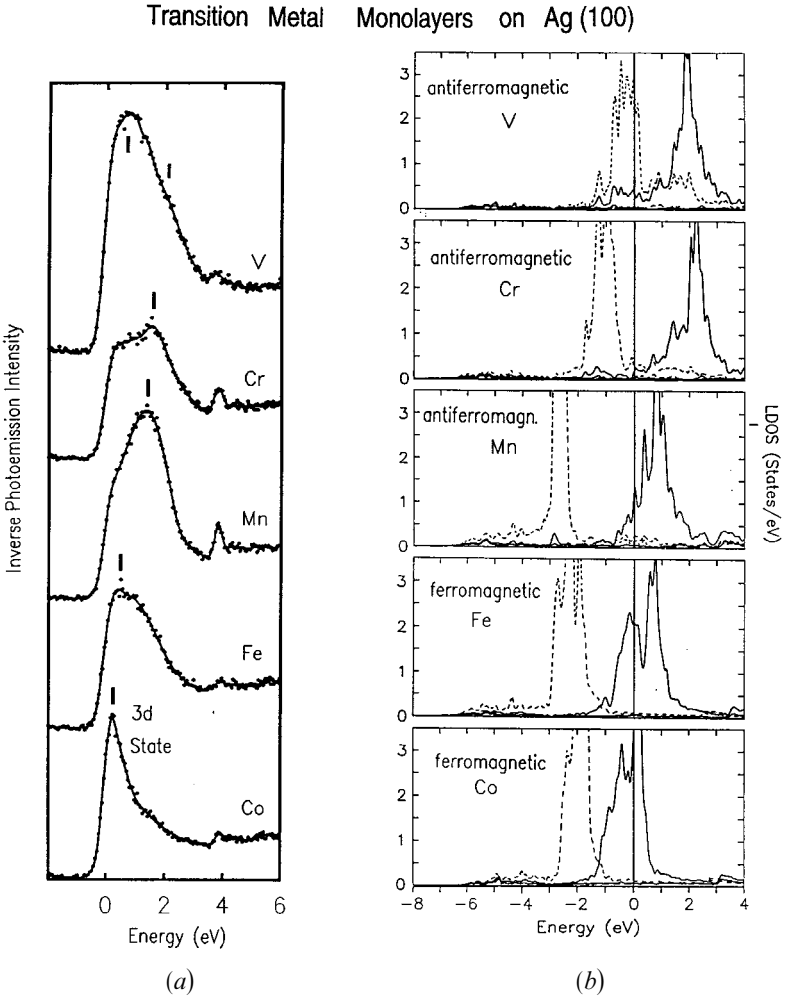

Figure 27. Density of states for transition-metal monolayers on Ag(100), showing the spin-split 3d bands filling up and crossing the Fermi level. Note the large magnetic splitting that is characteristic of high local moments. (*a*) Inverse photoemission results on unoccupied states obtained by Ortega and Himpsel (1993). (*b*) Local density calculation by Blügel *et al.* (1989).

and the Coulomb interaction. In order to have the same spin wavefunctions, the spatial wavefunctions have to be different. Being farther apart helps the electrons to reduce their Coulomb repulsion. In a solid it is the energy cost associated with finite bandwidth which acts against spin alignment. As one goes from the bulk to a monolayer, the bands become narrower, more like atomic levels, and the magnetic moment increases towards the maximum that is prescribed for the atom by Hund's rule. In a simple Stoner model the narrower bands mean a higher density of states at the Fermi level, which in turn drives a larger magnetic moment. Such ideas are confirmed by first-principles calculations for free-standing monolayers and monolayers and monolayers on weakly interesting noble metals and oxides. Figure 27 shows the calculated density of states for majority and minority spins across a series of 3d transition metals on the Ag(100) surface (Blügel *et al.* 1989). In all cases a

magnetic configuration has a lower calculated total energy for the monolayer than the non-magnetic state, despite the fact that some of these metals are non-magnetic in the bulk, for example V. The right-hand side of the 3d row orders ferromagnetically, and the left-hand side antiferromagnetically. Such calculations have led to predictions of enhanced magnetism in monolayers, where not only magnetic materials display enhanced moments, but non-magnetic materials may spontaneously become ferromagnetic (Fu *et al.* 1985, Richter *et al.* 1985, Blügel *et al.* 1989, Eriksson *et al.* 1991, Zhu *et al.* 1991).

Experimentally, it has been difficult to find clear evidence for spontaneous or *enhanced monolayer magnetism*. The search faces a general surface energy dilemma. Transition-metal monolayers are unstable thermodynamically on inert substrates, where the enhancement is predicted to be largest. To keep the surface energy low they tend to exchange atoms with the substrate or grow in clusters. The growth behaviour of transition metals on noble metals in general is reflected in the surface electronic structure, and particularly in the sharpness and intensity of their image states. Elements in the middle of the 3d series, that is Cr and Mn, exhibit the sharpest image states and, therefore, the most homogeneous growth (Ortega and Himpsel 1993). This is explained by a magnetic effect that lowers the surface energy for a half-filled 3d shell (Aldén *et al.* 1992). In this case, the 3d spins all line up according to Hund's rule. Thus each spin subshell behaves like a noble metal, the majority spins being completely filled and the minority spins empty. A similar high-spin configuration occurs in surface alloys of transition metals on noble metals, for example the $c(2 \times 2)$ structure of half a monolayer of Mn on Cu(100) (Wuttig *et al.* 1993b). Such alloys do not exist in the bulk because of size mismatch but become possible at the surface because the Mn atoms can expand outwards. In the process of increasing their atomic volume they develop a large local moment, which is reflected in a large magnetic exchange splitting (Rader *et al.* 1997). Direct evidence of long-range magnetic order is scarce in such systems despite extensive search. The best example is a Fe monolayer on Au(100) (see below). Spontaneous magnetization of paramagnetic metals was reported for V on Ag(100) but could not be confirmed. There have been indications for spontaneous magnetization for Rh/Ag(100) (Wu *et al.* 1994b) and Ru on graphite (Pfandzelter *et al.* 1995).

In order to obtain stable *layer-by-layer growth*, we need a substrate with high surface energy, or at least high interfacial bonding, since the surface energy of the transition-metal monolayer plus the interface energy has to be lower than the surface energy of the substrate (see section 2.1). On the other hand, strong bonding to a non-magnetic substrate will transfer the substrate paramagnetism to the overlayer. Typical examples are transition-metal films on W and Mo, which exhibit perfect initial epitaxy but tend to become paramagnetic at monolayer coverage. An exception is the closely packed W(110) surface, where a monolayer (and even submonolayer) is still magnetic (Elmers *et al.* 1989, 1994, 1995, Weber *et al.* 1990). Extrapolation to $T = 0$ yielded a 14% enhancement of the Fe moment of a Ag-coated Fe monolayer (Elmers *et al.* 1989). Another possibility is the growth of transition metals with comparable surface energy onto each other, which minimizes the surface energy difference. A popular example is Cr on Fe(100) where the strong Fe–Cr interface bond provides additional help. A magnetic moment of $3\mu_B$ has been measured for a monolayer of Cr on ferromagnetic Fe(100) and values of $4\mu_B$ or greater have been found at submonolayer coverage (Hopster 1994, Turtur and

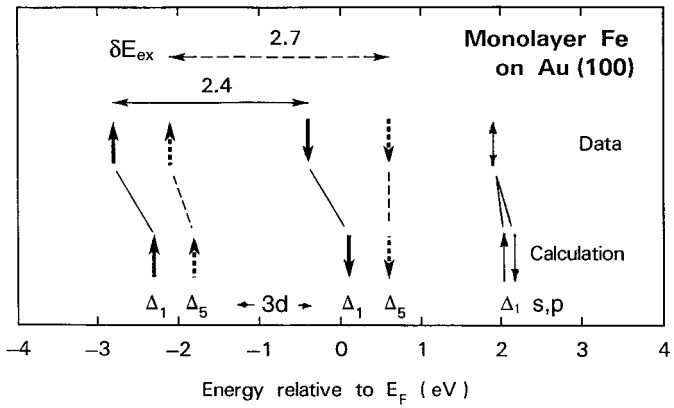

Figure 28. Electronic states of a Fe monolayer on Au(100) at $\mathbf{k}^{\parallel} = \mathbf{0}$. A large magnetic exchange splitting δE_{ex} is observed for the 3d states ($\Delta_1 = d_{z^2}$; $\Delta_5 = d_{xz,yz}$), but not for the s, p_z-like Δ_1 quantum well state (Heinen *et al.* 1990, Li *et al.* 1990, Himpsel 1991a, Crampin 1993).

Bayreuther 1994, Pizzagalli *et al.* 1997). This is much larger than the moment of $0.4\,\mu_B$ for antiferromagnetic bulk Cr.

One of the best-understood magnetic monolayers is Fe/Au(100). In this case, one has the good fortune that a monolayer of Au automatically diffuses onto the growing Fe monolayer, thereby lowering its surface energy and preventing it from breaking up into islands. As a consequence of this 'surfactant' action, Fe films on Au(100) remain ferromagnetic down to a monolayer (Bader and Moog 1987, Dürr *et al.* 1989), while for many other transition-metal overlayers the Curie temperature is reduced to zero at monolayer coverage (Wu *et al.* 1996) (see Kohlhepp *et al.* (1992) for other magnetic monolayers). The positions of the spin-split 3d bands for the Fe/Au(100) monolayer were obtained from spin-polarized photoemission and from inverse photoemission (figure 28). The magnetic splitting of the Δ_5 ($d_{xz,yz}$) band is enhanced from 1.8–2.1 eV in the bulk to 2.7 eV in the monolayer. This points towards an enhanced magnetic moment when using the relation between magnetic moment and exchange splitting in figure 13 as a guide. This result is in line with first-principles calculations for this system (Li *et al.* 1990) which predict enhanced magnetic splitting combined with enhanced moment. Only the splitting of the broad Δ_1 (d_{z^2}) band remains unchanged at 2.4 eV in contrast with theory, but that may be due to uncertainties in determining the peak position near the Fermi cut-off. In addition to the spin-split d-like states there is an additional s, p-like state with a very small magnetic splitting. It can be viewed either as a quantum well state extrapolating down from thicker Fe layers (see section 4.1) or as a Au(100) surface resonance, coming from the zero-coverage limit. It shows up in first-principles calculations as well (Crampin 1993). This type of state is visible in a series of transition-metal monolayers on Ag(100). It can be separated from the d-like states at photon energies below 10 eV where the 3d cross-section drops rapidly (Ortega and Himpsel 1993).

5.3. *Quantum wells*

A key feature of magnetic layer structures is the reflection of electrons at interfaces. It confines electrons to layers with lower inner potential and quantizes momentum and energy perpendicular to the layers. The reflectivity is spin dependent

owing to the spin dependence of the inner potential in ferromagnets. Therefore, these quantized states become spin polarized. Particularly important are *quantum well states at the Fermi level* (compare figure 1). The density of states at the Fermi level triggers electronic phase transitions, such as superconductivity, charge-density waves, ferromagnetism and antiferromagnetism. It also provides carriers for electrical and thermal transport. These phenomena can be tailored via quantum well states to produce novel electronic materials. Thus, quantum well states are at the heart of the 'designer solids' programme outlined in the introduction. Spin waves are reflected at interfaces, too. The resulting quantization of the perpendicular spin wave spectrum triggers the transition from three- to two-dimensional magnetism in thin films, as discussed in section 4.2.

One expects quantum well states to be a common phenomenon in thin films. Nevertheless, they have been the exception rather than the rule. The main culprit has been rough film morphology. Quantum well states require *interfaces smoother than the electron wavelength* (compare the interferometer model in section 5.4 and figure 41). That has not been easy to achieve in the past, but is becoming more prevalent as better growth techniques are being developed for metal films (Thomas 1970, Jaklevic and Lambe 1975, Iwasaki *et al.* 1985, Lindgren and Walldén 1987, 1988, Zhu *et al.* 1987, Miller *et al.* 1988, Mueller *et al.* 1990, Himpsel 1991a, Brookes *et al.* 1991, Jalochowski *et al.* 1992b). Quantum well states connected with magnetic phenomena were originally found by inverse photoemission and photoemission (Ortega and Himpsel 1992, Ortega *et al.* 1993a), but they also show up in the magnetic anisotropy (Weber *et al.* 1996) and in the magneto-optical response, such as the linear Kerr effect (Hayashi *et al.* 1993, Katayama *et al.* 1993, Carl and Weller 1995) and nonlinear Kerr effect (Kirilyuk *et al.* 1996). Quantum well states influence many other phenomena beyond magnetism, such as electrical conductivity (Jalochowski *et al.* 1992a), Hall effect (Jalochowski *et al.* 1996), superconductivity (Orr *et al.* 1984) and film growth (Hinch *et al.* 1989, Smith *et al.* 1996, Braun and Toennies 1997).

The *band structure* features of layer structures can be inferred from their unit, that is a single film confined by two interfaces. Taking vacuum on either side, one ends up with the geometry familiar from many slab calculations of surfaces. The band dispersion $E(\mathbf{k}^{\parallel})$ parallel to the surface of the slab is not affected by the confinement. Perpendicular to the surface, however, simple electron counting tells us that the continuous $E(\mathbf{k}^{\perp})$ spectrum of the infinite solid should be broken up into n discrete states per band, where n is the number of atomic layers in the slab (figure 29 (*a*)). These are often labelled *quantum well states*. Moving to figure 29 (*b*) brings us from reciprocal space to real space. The wavefunctions associated with the discrete states are characterized by a quickly oscillating Bloch function that is modulated by a slowly varying *envelope function*. The number of nodes in the envelope function determines the index of the discrete states. The farther away they are from the band edge, the larger the number of nodes becomes. The mathematical formalism for such states is well known from semiconductor quantum wells (Bastard 1988, Weisbuch and Vinter 1991). Roughly speaking, the Bloch function solves the bulk Hamiltonian, and the envelope function ensures that the boundary conditions at the surface of the slab are met, for example a node in the wavefunction at the boundary as shown in figure 29. In our example, the Bloch function wavelength is given by the atomic layer spacing via $\lambda_{\mathrm{Bloch}} = 2a$ because the wavefunction is expanded from states at the band edge at $k_{\mathrm{edge}} = \pi/a$. The envelope function wavelength λ_{env} is determined by the thickness d of the slab. With the specific

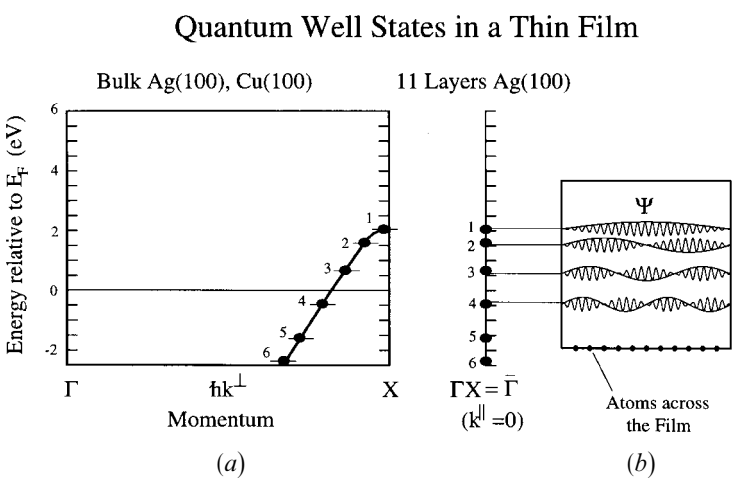

Figure 29. Quantum well states in a thin film. A band calculation for bulk Ag(100) from Eckhardt *et al.* (1984) is compared with an 11-layer slab calculation from Erschbaumer *et al.* (1991). The continuous bulk band breaks up into discrete states along $k^{\perp}$. The wavefunctions of the discrete quantum well states consist of a rapidly oscillating bulk Bloch function that is modulated by a slowly varying envelope wavefunction (Ortega *et al.* 1993a, b).

boundary conditions chosen in figure 29 (nodes at the surfaces of the slab) we have the simple condition that n half-wavelengths must fit into the slab, that is, $\lambda_{env} = 2d/n$. This implies that the wave-vector $k_{env} = 2\pi/\lambda_{env}$ comes in quanta of π/d, that is $k_{env} = n\pi/d$. Strictly speaking, k_{env} is not completely sharp owing to the finite extent of the wave train, and the uncertainty in $k^{\perp}$ is comparable with the spacing between adjacent $k^{\perp}$ points. The discrete energy levels are sharp, however, as long as the wavefunction is truly confined to the slab. For general boundary conditions, for example for the more realistic case of maxima in the wavefunction at the interfaces, the energy levels and $k^{\perp}$ points move but remain discrete.

The envelope function model for wavefunctions in a slab provides a good qualitative description of the phenomena encountered in multilayers and quantum wells. It has implicit limitations, however. By just combining the Hamiltonian for the bulk band structure with the boundary conditions of a slab, one neglects modifications of the *wavefunctions near the interfaces*, for example bonding with new neighbours across the interface. Therefore, such a model is expected to break down for slabs only a few atomic layers thick. This can already be guessed from the fact that the wavelengths of the envelope function and the Bloch function, that is λ_{env} and λ_{Bloch} become comparable when d is not much larger than a. In this case it is difficult to tell which of the two modulates the other. For obtaining information about the interfaces, one has to resort to more sophisticated calculations, such as first-principles local density theory (Crampin 1993, Mirbt *et al.* 1993, Samant *et al.* 1994, Crampin *et al.* 1996, Wu and Freeman 1996) (see also discussion of empirical tight-binding methods by Smith *et al.* (1994)). Figure 30 gives the calculated total spin density for a fcc Co/Cu(100) interface from Wu and Freeman (1996). It shows that the spin density induced in the Cu interface layer is much higher than in the deeper Cu layers. It also changes nodal character from d like to p like. One is tempted to assign the strong d-like interface spin density to direct exchange–

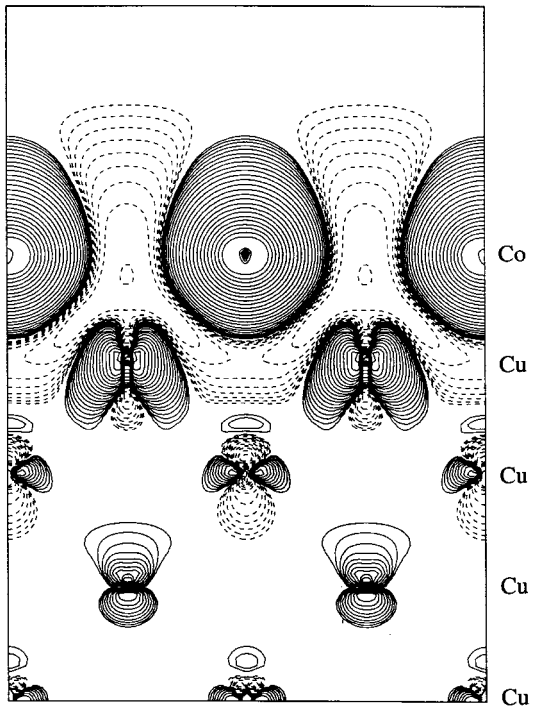

Figure 30. Calculated spin density across a Co–Cu(100) interface (Wu and Freeman 1996). The highly polarized Co 3d orbitals induce a d-like polarization at the Cu interface atoms (two nodal planes), which decays into a weaker p_z-like polarization towards the interior of the Cu spacer (single nodal plane). The latter is consistent with polarized s, p quantum well states in Cu.

hybridization with the Co neighbours, and the deeper p-like spin density to quantum well states derived from the s, p band.

Spectra of *quantum well states* in a simple magnetic layer structure are given in figure 31. Epitaxial Cu(100) films of varying thickness are deposited on top of a fcc Fe(100) or Co(100) film, which in turn is grown epitaxially on a Cu(100) surface. Compared with the continuum of a bulk Cu(100) crystal (top curve figure 31*b*) the spectra of thin Cu films exhibit discrete peaks due to individual quantized states. When numbered from the top down, all these peaks appear to move up in energy with increasing Cu film thickness. Eventually they converge towards the $X_{4'}$ point of Cu at 1.8 eV, which corresponds to the upper edge of the s, p band (compare the very similar band structure of Ag(100) in figure 29). Such a behaviour is exactly what we expect from a quantization of the s, p band into n discrete states, where n is the number of atomic layers in the film. For thicker films the density of $k^{\perp}$ points is higher, and the uppermost states move closer to the band edge. Such behaviour has been found for a number of magnetic multilayers using both inverse photoemission and photoemission (Ortega *et al.* 1993a).

The *energy positions* and movements of the quantized states with film thickness are described rather well by the simple envelope wave function model. Figure 32 shows a structure plot of the energy levels against Cu film thickness (full circles), obtained from photoemission and inverse photoemission data, such as those in

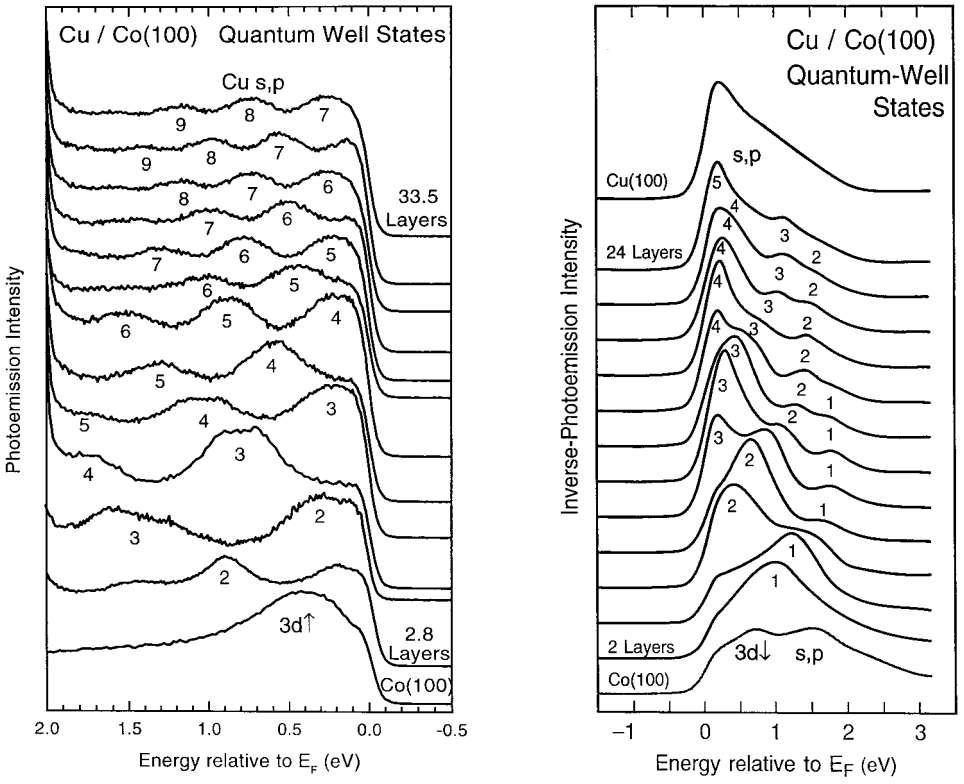

(*a*) (*b*)

Figure 31. Quantum well states in thin Cu films on fcc Co(100) as seen by photoemission and inverse photoemission at $\mathbf{k}^{\parallel} = \mathbf{0}$. The s, p-band continuum of bulk Cu is split up into discrete quantum well states that are numbered from the top of the band down (compare figures 29 and 32) (Ortega *et al.* 1993a, Segovia *et al.* 1996).

figure 31. The curves represent the envelope function model, which uses the bulk bands of Cu along the [100] direction as input (Ortega *et al.* 1993a):

$$d_n(E) = \frac{n - 1 + \varphi(E)}{1 - k_{\text{bulk}}(E)}, \tag{13}$$

where d_n is the thickness (in monolayers) at which the nth quantum well state appears at the energy E, $k_{\text{bulk}}(E)$ is the inverted bulk band dispersion (with k_{bulk} in units of the Brillouin zone boundary), and $\varphi(E)$ is the sum of the phase shifts for reflection at the two surfaces of the Cu slab (see below). The phase function $\varphi(E)$ could, in principle, be determined from bulk band calculations. Here, it is obtained empirically by fitting a linear $\varphi(E)$ relation to the $n = 2$ state. All the other states follow without adjustable parameters. For very thin Cu films (five atomic layers and less), one notices systematic deviations between the data and the simple envelope function model. This indicates that the approximation of a bulk Hamiltonian with thin-film boundary conditions breaks down. Rebonding across the interface becomes significant. Since the deviation starts already at five layers, not only the atoms right at the interface are affected, but also the next deeper layer. It is interesting to speculate that magnetic interactions might have a similar range. That would explain

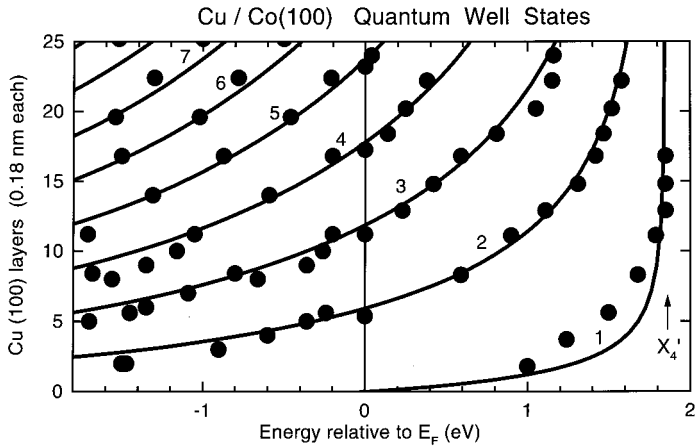

Figure 32. Energy against thickness diagram for quantum well states in Cu on fcc Co(100), where the states become denser in thicker films and appear to converge towards the upper band edge at X_4': (——), from a simple envelope function model (equation (13)); (●), from figure 31 (Ortega *et al.* 1993a, Segovia *et al.* 1996).

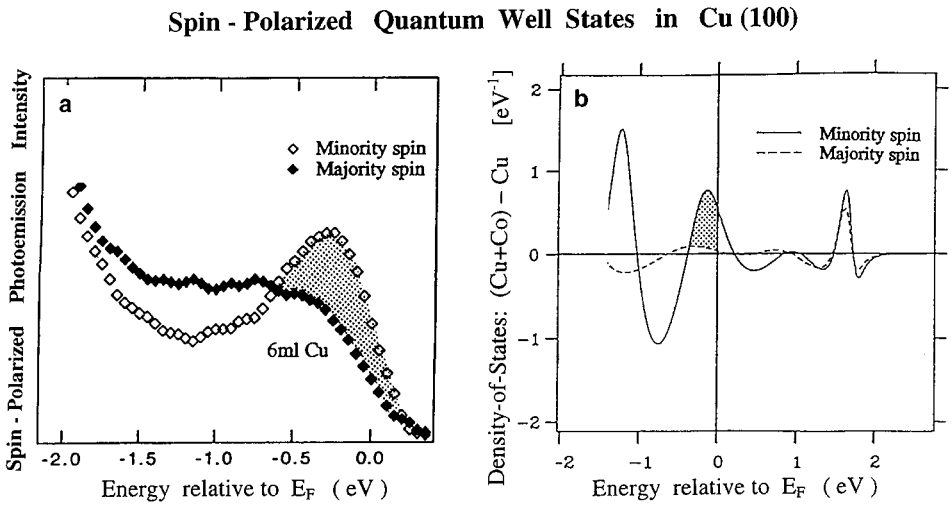

Figure 33. Spin polarization of quantum well states for Cu on Co(100). (a) Spin-polarized photoemission data obtained by Garrison *et al.* (1993). (b) First-principles calculation by Nordström *et al.* (1995).

why the Curie temperature of thin magnetic films is reduced to half its bulk value at a thickness of about five layers and why critical exponents switch from three dimensional to two dimensional at that thickness (see section 4.2).

For transmitting magnetic effects the quantum well states need to be *spin polarized*, even in a noble metal film, such as Cu. This rather counter-intuitive picture of a 'magnetized' noble metal has been confirmed, indeed. Figure 33(*a*) shows a spin-polarized photoemission spectrum of a quantum well state in a Cu on fcc Co(100) near the Fermi level (Garrison *et al.* 1993). It corresponds to state 2 in figures 31 and 32. The state has predominantly minority spin character. A first-principles local density calculation (Nordström *et al.* 1995) arrives at the same

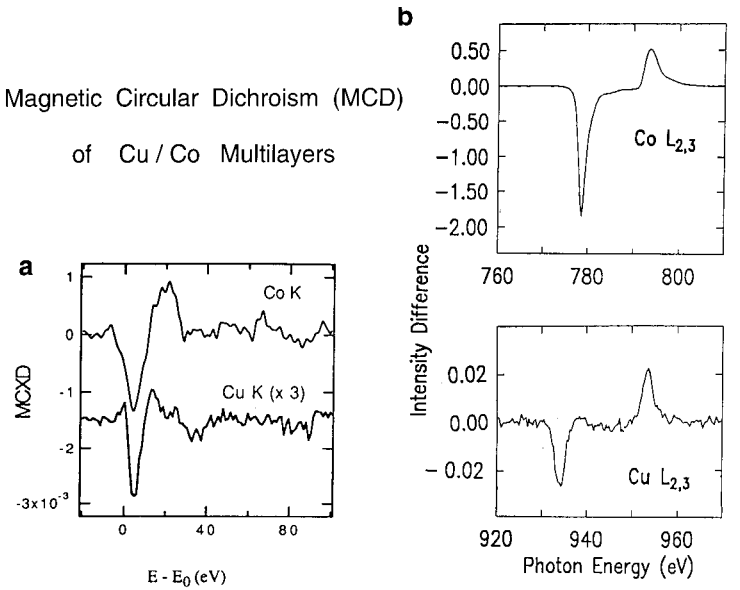

Figure 34. MCD data showing that Cu becomes spin polarized between Co layers. The magnetic moment at the Cu is only about two per cent of the Co 3d moment, but comparable with the Co 4p moment. (a) 4p-like magnetism probed by transitions from the 1s core level (Pizzini *et al.* 1995). (b) 3d magnetism probed by transitions from the 2p core level (Samant *et al.* 1994).

conclusion (figure 33(b)). MCD results from the Cu 2p and Cu 1s core levels (figure 34) show clearly that there is some spin polarization in the Cu film, albeit 50 times smaller than in the Co film (Samant *et al.* 1994, Pizzini *et al.* 1995). Both the 3d and the s, p states are spin polarized, but in opposite directions. Most of the Cu magnetization appears to reside near the interface (Samant *et al.* 1994), where hybridization with the magnetic Co states is strongest (compare figure 30). However, for explaining the observed magnetic coupling across the Cu layer (see section 5.4) it is necessary to have spin-polarized states all the way across the Cu layer. In fact the weakest link in the centre of the spacer layer is expected to determine the strength of the coupling.

There is a rather simple and general explanation for the spin polarization of quantum well states in magnetic multilayers. Quantum well states are formed by reflection of electrons at interfaces. The averaged inner potential of majority and minority states differs by the magnetic exchange splitting, leading to a *spin-dependent reflectivity*. Only states with significant band offset to the non-magnetic spacer band are being confined. For metals to the right of the ferromagnets (particularly noble metals) the majority bands are nearly lined up (figures 18 and 35). Therefore minority spins experience a band offset and are confined into quantum well states, but majority spins behave like a continuous bulk band that extends throughout noble metal and ferromagnet. For spacers to the left of the ferromagnets, for example Cr, the minority bands line up, and a majority spin polarization is expected for the quantum well states. This argument works independent of the specific band topology, but it does not guarantee full confinement, that is 100% reflectivity at the interface. Only in particular cases does one encounter a situation where minority

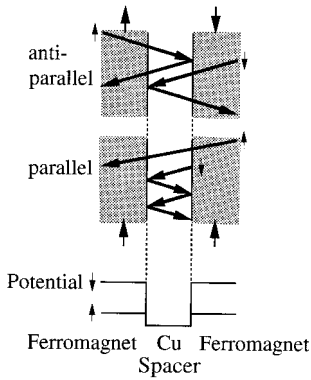

Figure 35. Schematic diagram of the possible wavefunctions in trilayers, where two magnetic layers are separated by a non-magnetic spacer (Himpsel and Rader 1995). Quantized states exist for parallel magnetization only (bottom) and not for antiparallel magnetization. This restriction is lifted in photoemission experiments on a bilayer, where the states are always confined on the vacuum side.

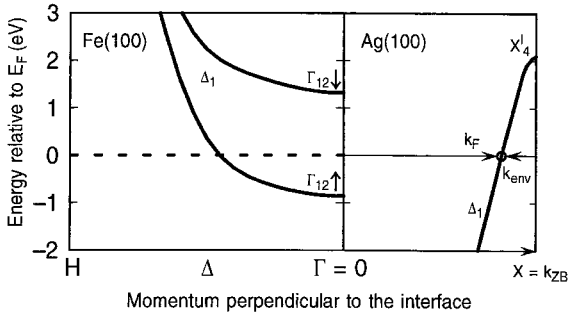

Figure 36. Explanation of the spin polarization of quantum well states by spin-dependent reflectivity, taking fcc Ag(100) on bcc Fe(100) as example. The minority spin electrons at E_F cannot propagate from Ag into Fe, owing to a Δ_1 symmetry gap in Fe(100). Therefore, they form standing waves, that is quantum well states in Ag(100). Majority spin states are able to propagate and remain band like (Ortega *et al.* 1993a).

spins become totally Bragg reflected since they run into a bandgap in the ferromagnet (figure 36).

It has been debated whether the *spin polarization in noble-metal spacer layers* is carried by 3d or by s, p electrons. A first glance at the Cu band structure, for example, shows only s, p bands near the Fermi level. The 3d bands beginning 2 eV below the Fermi level are apparently completely filled and are therefore not spin polarized. However, an angular momentum analysis of the s, p band shows that it contains significant 3d character due to hybridization with the 3d band (49%, 23% and 61% at the Fermi level for Cu, Ag and Au respectively, according to a tight-binding fit to local density calculations by Papaconstantopoulos (1986)). Since the moment carried by an s, p state is much smaller (and opposite) to that of a 3d state, one has the peculiar situation that the magnetization in the Cu film is likely to be carried by 3d states, even though they are part of the so-called s, p band. A proper angular momentum projection can be achieved by magnetic circular dichroism of transitions from different core levels, due to the $l \rightarrow l \pm 1$ dipole selection rule.

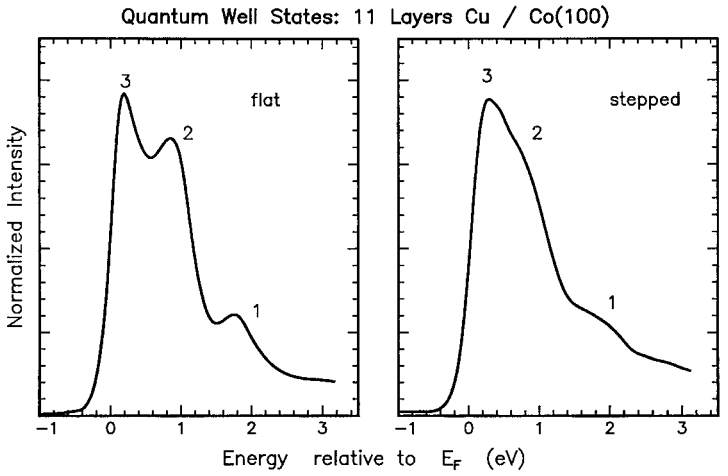

Figure 37. Influence of interface roughness on quantum well states (Ortega and Himpsel 1994). At a Cu/Co(100) surface with 1 nm step spacing the discrete states are smeared out owing to momentum transfer at the step lattice.

Figure 34 gives the result, which shows polarization in both the 3d and the 4p states. A real-space picture at the orbitals can be obtained from self-consistent calculations (figure 30) which suggest strong Cu 3d polarization at the interface and weaker Cu $4p_z + 3d_{z^2}$ polarization throughout the Cu spacer. The former may be viewed as hybridized Co–Cu states, the latter as s, p-like quantum well states.

The influence of *interface roughness* on quantum well states can be quantified by using stepped surfaces. Figure 37 shows that quantum well states in Cu on fcc Co(100) are broadened significantly on a stepped substrate with 1 nm terrace width (Ortega and Himpsel 1994). The modulation in the density-of-states oscillations at the Fermi level drops by a factor of two at this step spacing. In the future it would be interesting to prepare highly perfect multilayers and to explore the intrinsic width of quantum well states at the Fermi level. It should be much smaller than the widths observed so far if the states are truly two dimensional, that is in a gap of bulk states (such as the quantum well states responsible for the short-period oscillations in Cu/Co(100), (see section 5.4)). Such states do not exhibit $k^{\perp}$ broadening and are only broadened by $\mathbf{k}^{\parallel}$ transfer at defects.

Most quantum well states observed so far occur in s, p bands. A *quantization of 3d bands* is not easy to detect. The narrow band width places quantized states closely together such that they tend to overlap within their lifetime broadening (for d-like quantum well states see Hartmann *et al.* (1993), Ortega *et al.* (1993c), Mankey *et al.* (1994) and Li *et al.* (1995b)). Transition-metal spacers with their high density of d-states at the Fermi level and large lifetime broadening make it even more difficult to detect quantum well states. Nevertheless, density-of-states oscillations and shifts due to confinement have been observed for Cr on Fe(100) (Ortega *et al.* 1993c, Li *et al.* 1997). Quantum well states have even been seen for rather localized electrons, such as the valence states in solid Xe (Schmitz-Hübsch *et al.* 1995).

More sophisticated multilayer structures than quantum wells are starting to be explored by photoemission and inverse photoemission, for example *trilayers* and *interface doping* (Himpsel and Rader 1995, Hwang and Himpsel 1995, Li *et al.* 1995b). In trilayers, one can have standing waves not only in the non-magnetic

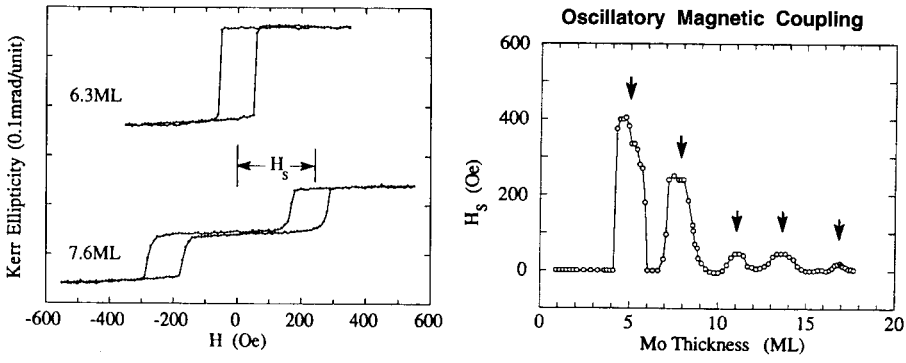

Figure 38. Magnetic oscillations at Fe/Mo/Fe(100) trilayers determined by the SMOKE (Qiu *et al.* 1992b). (*a*) Hysteresis loops characteristic of parallel and antiparallel coupling (top and bottom). H_s is the magnetic field required to force antiparallel layers parallel. Adding just slightly more than a monolayer to the Mo spacer reverses the magnetic orientation. (*b*) Alternating antiparallel and parallel coupling (arrows and baseline respectively).

spacer, but also in the ferromagnetic outer layers. The simple interferometer picture is again helpful. Instead of a mirror at each interface, one has now a mirror with an antireflective or reflective coating, depending on the thickness of the ferromagnetic layers. The reflectivity changes periodically with the thickness of the ferromagnetic layers with a period characteristic of the Fermi wave-vector of the ferromagnet. This effect has repercussions on the magnetic coupling since the strength of the magnetic coupling is sensitive to the spin-dependent reflectivity (see section 5.4) (Stiles 1996). Indeed, an oscillation of the coupling strength with the thickness of the ferromagnetic layers has been observed and explained (Bloemen *et al.* 1994, Bruno 1995).

5.4. *Oscillatory magnetic coupling*

One of the fascinating features of magnetic nanostructures is an oscillatory magnetic coupling (Grünberg *et al.* 1986, Parkin *et al.* 1990, 1991, Parkin 1991). Two ferromagnetic layers line up either parallel or antiparallel depending on the thickness of a non-magnetic spacer. This switching happens with atomic precision, as shown in figures 38 and 39, where the addition of little more than an atomic layer to the Mo or Cr spacer inverts the alignment of the Fe layers (Unguris *et al.* 1991, Qiu *et al.* 1992b). The effect has been observed for many combinations of ferromagnets and spacer materials (Parkin 1991). Typical oscillation periods are about 10 Å, but shorter and longer periods have been observed, too (e.g. short periods in Fe/Cu/Fe and Co/Cu/Co by Johnson *et al.* (1992a, b), in Fe/Mo/Fe by Qiu *et al.* (1992b) and a short and a long period in Fe/Cr/Fe by Unguris *et al.* (1991)). The oscillation periods are connected to the Fermi wavelength. That can be seen from their orientation dependence (Johnson *et al.* 1992a, b) or by modulating the Fermi surface via alloying (Parkin *et al.* 1993).

To find the *electronic origin* for this effect we focus onto states near the Fermi level, since they determine magnetic coupling and phase transitions. Figure 40 compares data on the thickness-dependent density of states in Cu layers on fcc Co(100) with Kerr-effect results on the magnetic coupling in fcc Co/Cu/Co(100)

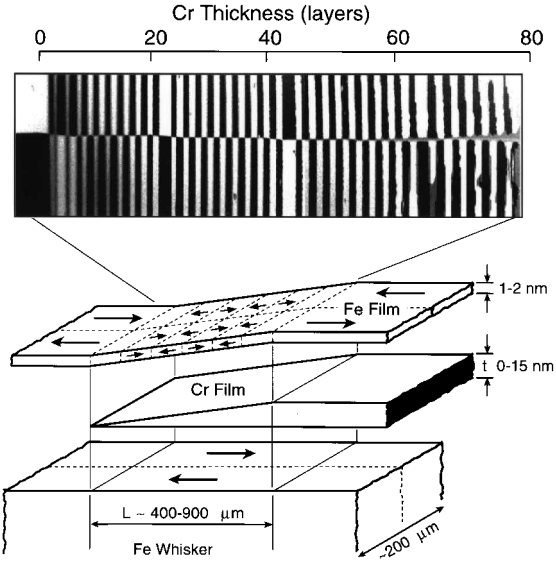

Figure 39. Oscillations in the magnetic coupling across a Cr spacer exhibiting a short and a long period (Unguris *et al.* 1991). The magnetic orientation of the outer Fe layer is determined by SEMPA.

trilayers (Qiu *et al.* 1992a, Carbone *et al.* 1993, Ortega *et al.* 1993a). The density of states at the Fermi level oscillates and the spin polarization follows suit. The period of about six atomic layers (1 nm) coincides with the magnetic period. Such a coincidence is found wherever comparable data exist, for example for Ag/bcc Fe(100), Au/bcc Fe(100), Cu/fcc Co(100), Cu/fcc Fe(100) (Ortega *et al.* 1993b), including short-period oscillations that require highly perfect interfaces (Cu/fcc Co(100) (Segovia *et al.* 1996)) and transition-metal spacers (Cr/Fe(100) (Li *et al.* 1997a)). Comparison of figures 41 and 31 shows how density-of-states oscillations can be traced directly to quantum well states, using Cu on fcc Fe(100) as example, which exhibits quantum well states very similar to Cu on fcc Co(100). Figure 41 simply represents a vertical cut through figure 31 at the Fermi level. Maxima in the oscillations in figure 41 correspond to quantum well states 2–5 crossing the Fermi level. Even without invoking the envelope function formalism described in section 5.3, one can give an intuitive explanation for the oscillations. The Cu spacer is comparable with a Fabry–Perot interferometer (figure 41), with the two interfaces acting as mirrors for electrons. By changing the spacing between the interfaces, one produces interference fringes every half-wavelength, as in the optical analogue. Thus, one has an interference device of atomic dimensions for electrons, which directly measures their wavelength. After discovering the similarity between density-of-states oscillations and oscillatory magnetic coupling the question remains why a density-of-states maximum appears to correlate with antiparallel coupling (figure 40). Even though such a coincidence may not hold in general, it may be driven by a mechanism suggested by S. D. Bader (1996), private communication); the high density of states at the Fermi level is unstable and leads to a magnetic restructuring. In a trilayer, quantum well states can only occur for the parallel orientation of the ferromagnetic layers, as shown in figure 35. For antiparallel orientation, wavefunctions are

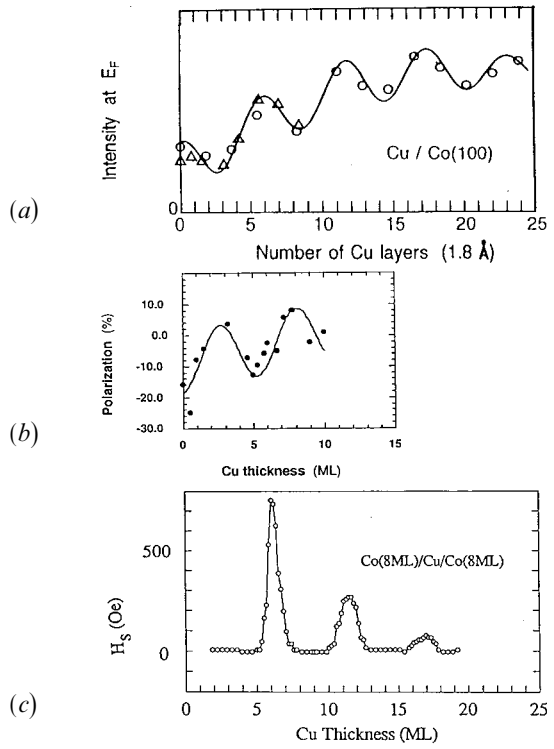

Figure 40. Simultaneous oscillations in (*a*) the density of states, (*b*) the spin polarization and (*c*) the magnetic coupling for the Cu/Co(100) system. Identical periods of six monolayers suggest a connection between quantum well states at the Fermi level and oscillatory magnetic coupling (Qiu *et al.* 1992a, Carbone *et al.* 1993, Ortega *et al.* 1993a). The magnetoresistance oscillates with the same period, too, since it requires antiparallel coupling (compare figure 47). H_S is the field required to switch the coupling between two Co layers from antiparallel to parallel (see figure 38).

confined by a single interface, and not by both. Therefore, the transition to antiparallel coupling circumvents the high density of states created by a discrete quantum well state. It may be puzzling why quantum well states are still seen in figures 31, 40 and 41 for Cu thicknesses characteristic of antiparallel coupling. This is because the density of states is measured for bilayers, where one of the ferromagnetic layers is replaced by vacuum. The potential barrier at the surface always confines the wavefunction. It is difficult to perform surface-sensitive experiments for trilayers where the ferromagnetic overlayer tends to swamp the signal from the spacer. First results demonstrate that one can see through the overlayer under favourable conditions (Himpsel and Rader 1995).

The wavelength measured in the density-of-states oscillations is that of the envelope function, and not the much shorter wavelength of Bloch states at the Fermi level. This explains a puzzle that magnetic oscillations posed right after their discovery: why are the *periods* so much longer than the Fermi wavelength, which is the length scale in classic models of magnetic coupling, such as the RKKY model (see below). There is a second length scale in the system, that is the lattice constant, and the beating frequency between the Fermi wavelength and the lattice constant determines the long magnetic oscillations. Using the same argument in reciprocal

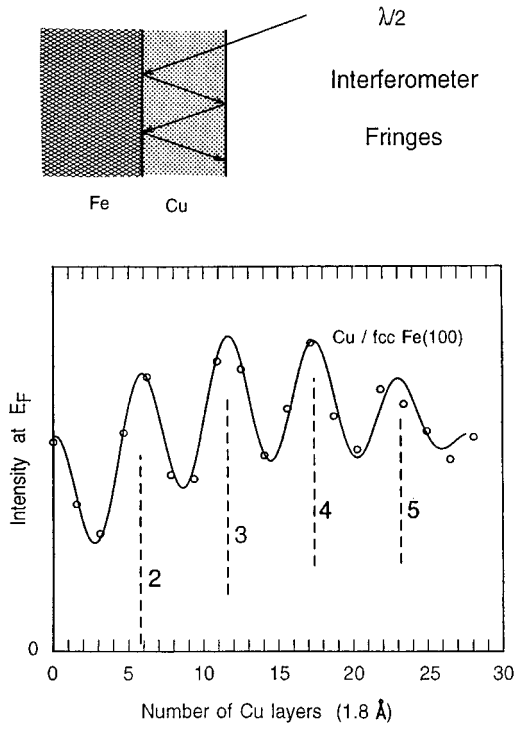

Figure 41. Interferometer picture for the oscillations in the density of states with thickness (Ortega *et al.* 1993a). The wavelength λ of the envelope wavefunction is measured directly (compare figure 29). Peak number n corresponds to quantum well state number n passing through the Fermi level in figure 31*b*.

space (figures 29, 36), one has to determine the (short) envelope function wave-vector k_{env} by subtracting the (long) Fermi wave-vector $k_F = 2\pi/\lambda_F$ from the (long) zone boundary wave-vector k_{ZB}:

$$k_{env} = k_{ZB} - k_{Fermi}. \tag{14}$$

The oscillation period in monolayers is given simply by the inverse of the envelope function wave-vector k_{env} in units of the zone boundary (Ortega *et al.* 1993a). The fact that the Fermi level crossing in Cu occurs at about one sixth of the Brillouin zone away from band maximum at X leads to a six-layer oscillation period. This result is identical with the prediction of RKKY theory after taking the discrete lattice into account, as we shall show in the following.

The RKKY model describes the coupling between two spin impurities via an intervening electron gas (compare section 3.2.1). The electron gas responds to the first spin by spin-density oscillations whose period is set by the Fermi wave-vector k_F. A second spin at a distance r from the first couples to the spin-density wave. For a free-electron gas, the interaction energy between the two spins takes the form

$$J(r) \propto \frac{\cos(2k_F r)}{r^3}. \tag{15a}$$

When summed over spins in two sheets, the coupling becomes

$$J_{planar}(z) \propto \frac{\cos(2k_F z)}{z^2}, \tag{15b}$$

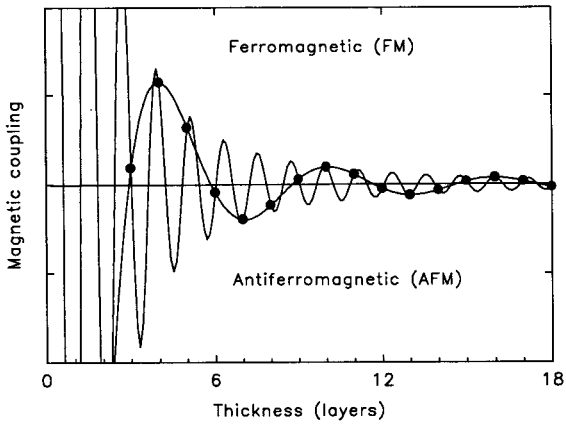

Figure 42. Formation of a beat frequency (aliasing) between the Fermi wavelength and the lattice periodicity for the RKKY coupling through Cu along the [100] direction. The long beat frequency of six atomic layers corresponds to the wavelength of the envelope wavefunction in figures 29 and 41.

where z is the spacing between the sheets (figure 15b). At finite temperatures an additional damping of the oscillations is to be expected. Experimentally, the coupling strength is found to be sensitive to the preparation and magnetic domain structure of the films. A number of power laws have been reported, some close to the inverse square law (figure 40) (Qiu *et al.* 1992a), some decaying faster (see figure 47, Parkin *et al.* 1994a, b). The situation changes somewhat when the crystal lattice is introduced into the continuous electron gas of the traditional RKKY approach (Bruno and Chappert 1991, Koelling 1994, Bruno 1995). Now, the quickly oscillating RKKY coupling can only be sampled at discrete crystal planes (aliasing). Figure 42 shows the resulting beat frequency between the Fermi wavelength and the lattice constant. If the two are similar, the resulting oscillation period can become quite long, such as for Cu along the [100] direction. The end result consists of several periods that are given by spanning vectors between two extremal portions of the Fermi surface (figure 43). In most cases, these RKKY periods are identical with those obtained for quantum well states, with the spanning vector equal to twice the envelope wave vector k_{env}. Sometimes, the reasons for this coincidence can be quite subtle (Edwards *et al.* 1994, Ferreira *et al.* 1996).

With the similarity in the periods predicted by RKKY and quantum well states, the question arises whether or not the two models are equivalent descriptions of the same physics. Theoretical work has established close connections between the two approaches (Edwards *et al.* 1991, Stiles 1993, 1996, Bruno 1995, Mathon *et al.* 1995). Essentially, one starts in the quantum well model with a total energy expression that consists of a sum over all occupied quantum wells (figure 44). Whenever a quantum well state crosses the Fermi level, the energy balance changes abruptly, and switches from one magnetic configuration to the other. The total energy integrals are similar to the momentum space integrals in the RKKY method. Although details are still being worked out in this connection, there is good reason to believe that the identical periodicity predictions are based on common physics, with the RKKY approach coming from reciprocal space and the quantum well approach from real space. Predictions for the *strength of the coupling*, however, are not identical (van

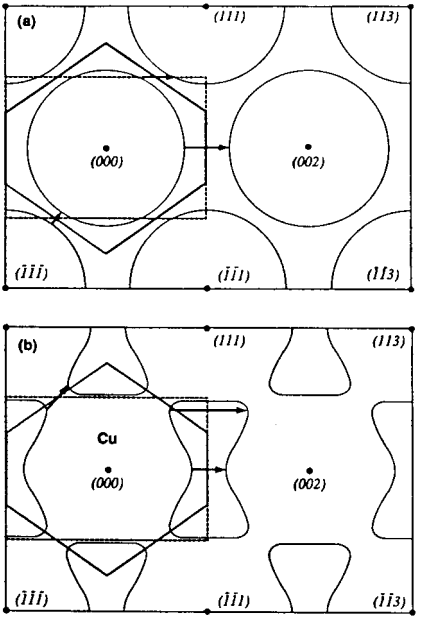

Figure 43. Extremal spanning vectors across the Fermi surface of Cu in low-index crystallographic directions (arrows). They determine the period of magnetic oscillations (Bruno and Chappert 1991). Top: free electrons. Bottom: electrons in Cu.

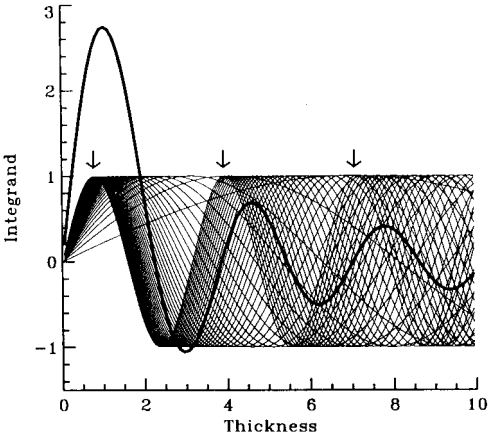

Figure 44. Integration of the magnetic interaction energy over parallel momentum for a magnetic quantum well (Stiles 1993). The integrand at 20 $\mathbf{k}^{\parallel}$ values (——) is summed up to give the bold curve, cancelling out most of the oscillations. Only oscillations coming from extremal points in the Fermi surface remain (arrows).

Schilfgaarde and Harrison 1993, Mathon *et al.* 1995). Traditional RKKY theory represents a lowest-order perturbative treatment. In the quantum well approach, there is no such restriction. The coupling strength depends not only on the density of states near extremal points of the Fermi surface but also on the spin-dependent reflection amplitudes at the interface (Stiles 1996). Truly confined quantum well states contribute much more than resonances. That explains why the short-period

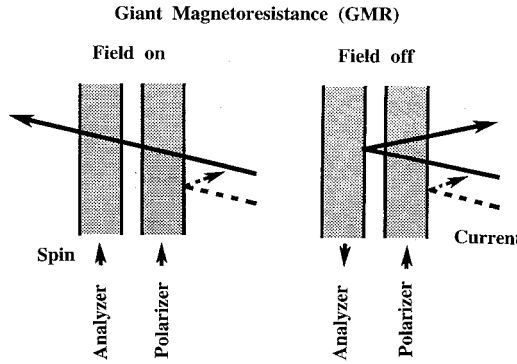

Figure 45. Simplified visualization of GMR via an optical polarizer–analyser analogue. Interfaces at ferromagnetic layers act as spin polarizers, owing to their spin-dependent electron scattering. The electron current perpendicular to the interfaces increases when the magnetic orientation is switched from antiparallel (crossed optical polarizers) to parallel by an external field.

oscillation in Cu(100) spacers is predicted to dominate the longer period in the coupling (Mathon *et al.* 1995). In fact, the calculated spin density in figure 30 is dominated by the short period. It has been difficult to quantify the strength of the short period coupling, owing to the extreme interface smoothness required to establish short-period quantum well states. Ongoing experiments with very smooth interfaces grown and measured at low temperature promise to settle this question in the near future (Segovia *et al.* 1996, Würsch *et al.* 1997).

5.5. *Magnetic tunnelling and giant magnetoresistance*

Magnetoresistance can be produced by many different mechanisms for (see section 3.2.2), but there are two effects that are characteristic of two-dimensional magnetic nanostructures. These are spin-polarized tunnelling and GMR. The basic structural unit in both is a trilayer where two ferromagnetic layers are separated by a non-magnetic layer, typically 1 nm thick. The separation layer is an insulator in magnetic tunnelling and a metal in GMR. Two magnetic configurations are possible: one with the ferromagnetic layers oriented parallel, and the other antiparallel (figure 45). The parallel configuration exhibits the lower resistance. If one starts out with an antiparallel configuration and forces it into parallel alignment by an external field, the resistance decreases (negative magnetoresistance). To obtain the antiparallel configuration as starting point there are several possibilities, that is oscillatory magnetic coupling at the right spacer thickness (section 5.4), dipole coupling at large spacer thickness (figure 15(*c*)), random coupling in granular materials, pinning one magnetic layer to an antiferromagnet (exchange biasing), and using two ferromagnets with different coercivities.

Spin-polarized tunnelling can occur between various combinations of ferromagnets, normal metals and superconductors (Meservey and Tedrow 1994). In all cases there is an insulating spacer layer that acts as barrier for planar tunnelling. Owing to the high barrier in the insulator, only electrons close to the Fermi level participate in the tunnelling process, and of those the s, p electrons with their more extended wavefunctions dominate. The density $n\uparrow$ of majority states is higher for s, p states at the Fermi level than the density $n\downarrow$ of minority s, p states (see section 3.2.2). Consequently, a large number of majority spin electrons emitted into the junction

meets a high density of empty states when the magnetic orientation is parallel. Therefore the resistance is low. This argument is quantified by adding the conductivities $\sigma \propto 1/R$ of the two spin channels, which gives $\sigma\uparrow\uparrow \sim n\uparrow n\uparrow + n\downarrow n\downarrow$ for parallel orientation and $\sigma\uparrow\downarrow \propto n\uparrow n\downarrow + n\downarrow n\uparrow$ for antiparallel. Defining the spin polarization as

$$P = \frac{n\uparrow - n\downarrow}{n\uparrow + n\downarrow} \tag{16}$$

and generalizing to two electrodes with different spin polarizations P_1 and P_2, one obtains a formula for $\delta R/R$. At this point we have to mention that two definitions of $\delta R/R$ exist in the literature, which are normalized to the maximum and minimum resistance respectively:

$$\left(\frac{\delta R}{R}\right)_c = \frac{R\uparrow\downarrow - R\uparrow\uparrow}{R\uparrow\downarrow}, \qquad \text{'conservative', } \leqslant 100\%, \tag{17a}$$

$$\frac{\delta R}{R} = \frac{R\uparrow\downarrow - R\uparrow\uparrow}{R\uparrow\uparrow}, \qquad \text{'inflationary', up to } \infty. \tag{17b}$$

Their relation is

$$\frac{\delta R}{R} = \left(\frac{\delta R}{R}\right)_c \Big/ \left[1 - \left(\frac{\delta R}{R}\right)_c\right]. \tag{17c}$$

The resulting magnetoresistances are

$$\left(\frac{\delta R}{R}\right)_c = \frac{2P_1P_2}{1 + P_1P_2} \qquad \text{(Julliere 1975)}, \tag{18a}$$

$$\frac{\delta R}{R} = \frac{2P_1P_2}{1 - P_1P_2}. \tag{18b}$$

Strictly speaking, these are upper limits for $\delta R/R$ since our argument neglects spin flip. One might guess that in the field of GMR the inflationary definition has become the more popular. In tunnelling, one finds both the former (Moodera and Kinder 1996) and the latter (Miyazaki and Tezuka 1995). Magnetoresistance was a small effect in tunnelling at room temperature for a long time, until better growth methods were developed for atomically sharp metal–insulator junctions (Meservey and Tedrow 1994, Miyazaki and Tezuka 1995, Moodera and Kinder 1996, Moodera *et al.* 1996, Gallagher *et al.* 1997.) Now, the observed effect comes close to the limit in equation (18). In fact, a non-uniform current flow is able to simulate even larger effects of up to 100% (Moodera *et al.* 1996). To see how close the data are to the theoretical limit, we take an effective spin polarization $P = +40\%$ from tunnelling between Fe and a superconductor (Meservey and Tedrov 1994). With this value, equation (18*b*) gives $\delta R/R = 38\%$. Miyazaki and Tezuka (1995) reported experimental values of $\delta R/R = 30\%$ at 4 K and 18% at room temperature for an Fe/Fe junction (figure 46). For a CoFe/Co junction the magnetoresistance measured by Moodera and Kinder (1996) reaches $(\delta R/R)_c = 25.6\%$ at 4 K and 18% at room temperature, again close to the limit of $(\delta R/R)_c = 27.6\%$ given by equation (18*a*) in this case. The transitions happen rather sharply with the applied field, with $(\delta R/R)/H$ up to 5% Oe^{-1} (Moodera and Kinder 1996), making these structures interesting for magnetic storage devices and sensors. There is ample room for

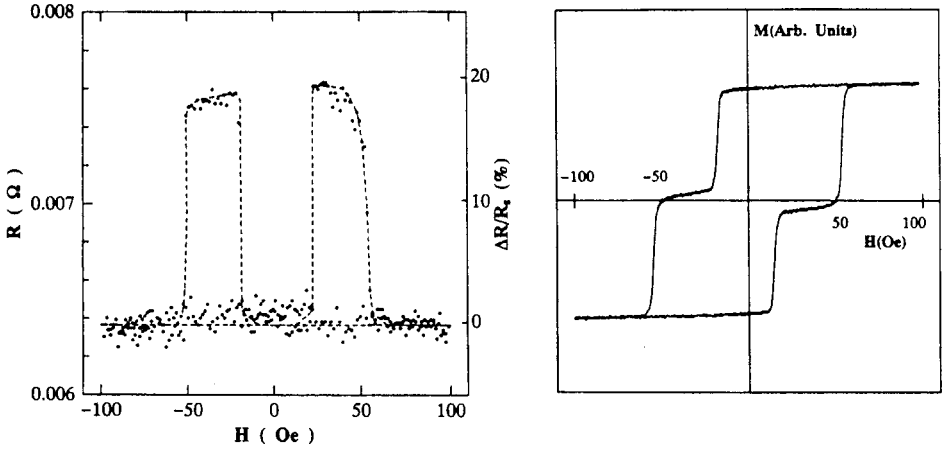

Figure 46. Magnetoresistance via magnetic tunnelling in an $Fe/Al_2O_3/Fe$ junction at room temperature (Miyazaki and Tezuka 1995). The resistance is low when the two Fe layers are magnetized parallel (for $|H| < 20$ Oe and $|H| > 52$ Oe) and high in between, as seen in conjunction with the $M(H)$ hysteresis curve. The different switching fields of the two Fe layers were generated by deposition at room temperature (high coercivity) and 200°C (low coercivity).

manipulating tunnel junctions, for example by using ferromagnetic insulators as barriers. The sensitivity to the quality of the interfaces suggests possibilities for interface engineering by interlayers.

GMR occurs in two geometries, i.e., with the current in the plane of the layers (CIP) and the current perpendicular to the plane of the layers (CPP). The CPP geometry is much less practical than the CIP geometry, owing to the extremely small resistance across the nanolayers, but it is conceptually simpler and exhibits larger magnetoresistance. Interfaces play the essential role in this effect. They can be bypassed by part of the current in the CIP geometry. Roughness, on the other hand, brings them back into the picture, which makes the CIP effect rather susceptible to structural details. Indeed, both an increase and a decrease in the magnetoresistance with increasing roughness have been observed in this geometry. A general description of GMR involves 20 parameters (Hood and Falicov 1992); the two ferromagnetic layers and the spacer are characterized by three thickness parameters, three effective masses, three inner potentials, three relaxation times and eight spin scattering parameters (four for the two outer surfaces of the stack and four for the two interfaces inside). Each surface or interface has two parameters, one for each spin, which describe specular as against diffuse scattering. A number of experiments have been designed to pinpoint individual parameters and to assess their relative importance. Here we shall focus on the simpler, CPP geometry to give a flavour of the key phenomena contributing a GMR (for detailed analyses see Camblong *et al.* (1993), Valet and Fert (1993) and Fert *et al.* (1994)). A good starting point is the optical polarizer–analyser analogy in figure 45. Conduction electrons become spin polarized by spin-dependent scattering at magnetic interfaces. Antiparallel orientation of the two ferromagnetic layers is equivalent to crossed optical polarization filters. (Note that a 90° rotation of an optical polarizer corresponds to a 180° rotation for an electron polarizer since the photon spin is 1 and the electron spin $\frac{1}{2}$.) Therefore, the transmitted electron current is low in the antiparallel configuration.

Such a picture can be quantified into a two-channel model, where majority and minority spins are treated as separate current channels and their conductivities are added up (see the discussion of spin-polarized tunnelling above). Such a model assumes a low probability for spin-flip scattering across the whole stack. Each channel then experiences the equivalent of a series of resistors when electrons are scattered at various interfaces and in the bulk.

A priori, it is not obvious whether the spin-dependent scattering takes places at the interfaces or in the bulk. It might not even be specular, as in the simplified picture in figure 45, but rather diffuse, owing to inelastic scattering by d electrons. In either case, the resulting resistance change is the same. A natural explanation for *interface scattering* comes from the spin-dependent step in the inner potential which, in some cases, causes even total reflection of minority spins and spin-polarized quantum well states (figures 18 and 36 and section 5.3). Spin-dependent bulk scattering is due to electron–hole pair creation at the Fermi level, which affects mostly minority spins since the density of minority spins is higher at the Fermi level (at least in Co and Ni) and spin is conserved during this type of scattering. In a sense, the majority spin band structure of Co and Ni is like that of a noble metal, with the d bands completely filled (see figure 11). Perpendicular transport measurements on multilayers are able to settle the issue. If it is an interface effect, then the magnetoresistance should increase with increasing number of interfaces or layers in a stack. If it is a bulk effect, only the overall thickness of the stack should matter, but not the number of layers. Results from such an analysis produce interface scattering ratios $\alpha_{A/B} \approx 10$ and bulk scattering ratios $\alpha_A \approx 3$ between minority and majority spin electrons, showing that interface scattering is indeed the dominant factor in GMR (Pratt *et al.* 1993). Independent evidence for the critical role of interfaces are experiments where the magnetoresistance is strongly affected by coating the interfaces by as little as a monolayer of a foreign material (interface doping). Placing a high-moment ferromagnet at the interface, such as Co, more than doubles the magnetoresistance (Parkin 1992, 1993). Spectroscopic studies of such interfaces reveal a variety of interface states with decay constants in the monolayer range that are likely to be connected with an enhanced reflectivity of minority spin electrons at a Co interlayer (Hwang and Himpsel 1995, Li *et al.* 1995b).

Sophisticated multilayer structures allow an analysis of the spin-dependent bulk *mean free paths* at the Fermi level that enter into the 20 parameters describing GMR. Typical values range from 2 to 10 nm, with a spin asymmetry α ranging from 10 in Co to less than unity in Fe, where the majority-to-minority spin ratio at the Fermi level is inverted relative to Co and Ni (Pratt *et al.* 1991, 1993, Gurney *et al.* 1993). Noble metals, such as Cu, have a much longer mean free path of more than 100 nm at the Fermi level. These mean free paths determine the magnetic layer thickness where the bulk effect saturates. A much longer mean free path determines spin-flip scattering, usually large compared with the thickness of the multilayer structures. Typical values range from micrometres in noble metals to 20–90 nm in metals with spin impurities as spin scatterers (Bass *et al.* 1994, Fert *et al.* 1994, Fert and Lee 1996). When the energy of the electrons is increased, such as in photoemission experiments, the mean free path becomes shorter owing to the increasing phase space for creating electron–hole pairs. This gives rise to the shorter mean free paths in figure 10 at an energy of abut 5 eV above the Fermi level.

There is a wealth of *experimental results* on GMR. Shortly after its discovery the effect was explored far enough to be incorporated into electronic devices, thereby

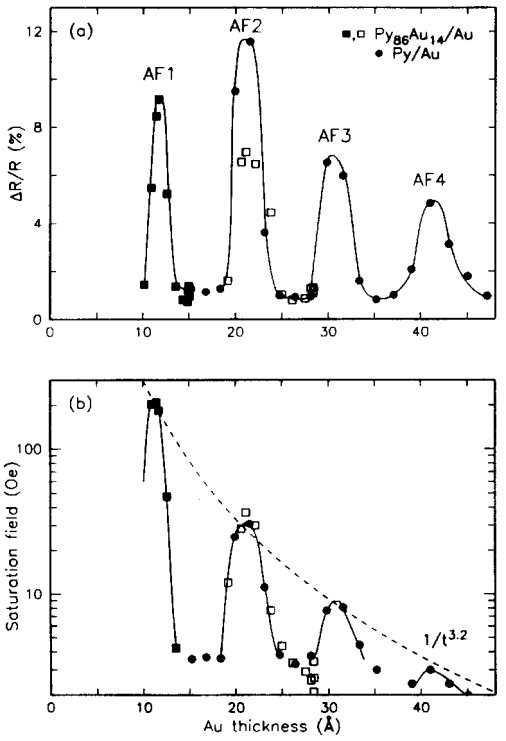

Figure 47. GMR (a) against oscillatory magnetic coupling (b) in $Au/Ni_{0.8}Fe_{0.2}(111)$ multilayers (Parkin *et al.* 1994a, b). GMR occurs only at well defined thicknesses of the Cu spacer layer where the Co layers are magnetized antiparallel. The resistance drops when the orientation is switched from antiparallel to parallel by the external field.

providing a good test case for the use of nanostructures in the real world. Early results by Baibich *et al.* (1988) and Binasch *et al.* (1989) were systematically expanded by Parkin *et al.* (1990, 1991) and connected with oscillatory magnetic coupling (figures 40 and 47). Perpendicular transport measurements became possible by using superconducting contacts to measure extremely low resistances (Pratt *et al.* 1991, 1993) or by increasing the resistance through micropatterning (Gijs *et al.* 1993). An increase in the magnetoresistance of a factor of three to ten was found when going from the parallel to the perpendicular geometry in the same sample (Pratt *et al.* 1991). Resistance changes of up to 220% (normalized to the lower resistance at high fields) have been obtained at 1.5 K (Schad *et al.* 1994). GMR occurs not only in well ordered multilayers but also in granular materials, such as ferromagnetic particles segregated in noble metals (Berkowitz *et al.* 1992, Xiao *et al.* 1992, Hylton *et al.* 1993). The effect occurs also in a homogeneous film with striped magnetic domains that provide regions with antiparallel magnetizations (Gregg *et al.* 1996). Essentially, a random coupling is enough to produce GMR because half of the grains or domains are antiparallel to each other, on average.

Stripe and wire structures are being explored for GMR in order to have the best of all worlds, that is the high magnetoresistance perpendicular to the interfaces as well as the workable resistance of the in-plane geometry. In stripes, the current can flow in the plane but perpendicular to the stripes. Azimuthal rotation by 90° leads to

a geometry with the current parallel to the interfaces that produces a less favourable magnetoresistance. The resulting in-plane anisotropy of the magnetoresistance has been observed in structures built on sawtooth-like Si surfaces (Ono and Shinjo 1995, Oepts *et al.* 1996). Wires consisting of stacks of magnetic–non-magnetic multilayers can also produce a current perpendicular to the interfaces with a reasonable resistance along the wires (Blondel *et al.* 1994, Piraux *et al.* 1994, Liu *et al.* 1995). Such geometries lead naturally to the study of one-dimensional magnetic nanostructures.

6. One-dimensional systems: steps and stripes

Most of the concepts developed for surface states and quantum well states in planar structures can be extended to one-dimensional wire or stripe structures. It is much more difficult to obtain truly confined states, however, since bulk states are able to couple to wire states much more easily. They can be projected along two **k** directions: one perpendicular to the surface, and the other inplane but perpendicular to the wires. The crystal periodicity is kept only along the wire direction. Nevertheless, a variety of step-related electronic and magnetic phenomena have been discovered, such as step states, lateral quantization and in-plane anisotropy. Some of the effects are familiar from semiconductors where an absolute gap makes it easier to confine states along two directions and to observe one-dimensional phenomena (for reviews see Hansen *et al.* 1992 and Kastner 1993).

In passing we would like to mention a completely different class of materials with one-dimensional electronic states. These are bulk compounds containing *chains or ladders* of magnetic atoms that are stabilized and decoupled by an insulating lattice of ionic groups, either organic or inorganic (e.g. in perovskites). They become magnetic at low temperatures and have been used as testing ground for phenomena in one-dimensional magnetism, such as the Haldane gap in antiferromagnetic chains.

The one-dimensional analogue of a two-dimensional surface or interface is a *single step*. Electrons that are confined perpendicular to the surface already can become confined perpendicular to the step, Too. Even if they are not totally confined, their wavefunction is scattered elastically at the step edge, producing standing waves and ripples in the charge density. These oscillations have been sampled directly by scanning tunnelling spectroscopy. For example, the p_z-like surface state in figure 24 has been used to produce interference patterns when reflected at steps on Cu(111) (Crommie *et al.* 1993a), Ag(111) (Avouris *et al.* 1994, Li *et al.* 1997b) and Au(111) (Hasegawa and Avouris 1993). The patterns look similar to the ripples in figure 8 that are produced by reflection of electrons at the boundaries of a corral. Such reflections at a step edge are equivalent to a surface resonance. The analogue of a surface state would be a wavefunction confined to a step edge. Such step states have been seen by photoemission on highly steped Ir(111) and Ni(111) surfaces (Van der Veen *et al.* 1981, Namba *et al.* 1993). Even the one-dimensional equivalent to a monolayer state, that is a single-row state, has been found for Cu strings on stepped W(110) (Himpsel and Ortega 1994). All these cases deal with a p_z-like surface state becoming confined to a step.

A *terrace* confined by two parallel steps is the one-dimensional analogue of a thin film. Such a structure produces lateral standing waves (Avouris and Lyo 1994), similar to the standing waves induced by quantum well states in a thin film (compare section 5.3). On a terrace, the band structure perpendicular to the steps becomes

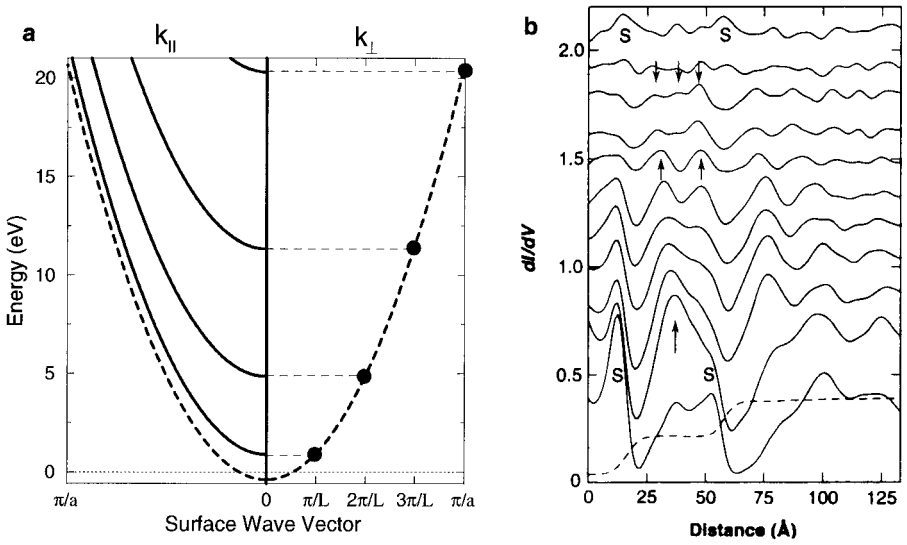

Figure 48. Band structure of electrons confined to a single stripe of length L. (a) Schematic diagram showing quantized levels perpendicular to the stripe (along $k^{\perp}$) and band dispersion parallel to it (along $k^{\parallel}$). (b) Charge density of the first three quantized states on a Au(111) terrace 0.36 nm wide, probed by scanning tunnelling specroscopy (Avouris and Lyo 1994). The dI/dV spectra are offset according to the sample bias. The arrows indicate maxima in the charge density when the bias voltage coincides with one of the quantized levels. The step profile is shown as a broken curve.

quantized (figure 48a). The number of quantized states is equal to the number of rows on the terrace, as in thin films. Parallel to the step the continuum of energies remains. Scanning. tunnelling spectroscopy allows direct visualization of this effect (figure 48b). By measuring in the spectroscopic mode, that is, detecting dI/dV against V at constant current, one effectively probes the charge density of the standing waves. With increasing sample voltage V, one passes through the lowest three quantized states, that is the $n = 1$ state at - 0.33V (single arrow), the $n = 2$ state at - 0.01 V (double arrow), and the $n = 3$ state at +0.41 V (triple arrow). Their spacing from the bottom of the two-dimensional surface state band at - 0.41 V increases nearly quadratically with n. That is expected when a band with parabolic $E(k)$ dispersion becomes quantized into equal k intervals (see figure 48a). The lateral charge density exhibits an increasing number of maxima, like the envelope function of quantum well states (compare section 5.3 and figure 29). In addition to the quantized terrace states there are peaks in the dI/dV spectra at the bottom of the steps (labelled S in figure 48b). They may signify step states, which represent the one-dimensional analogue of a two-dimensional surface state, as discussed in the previous paragraph.

On a stepped surface we have an infinite array of parallel steps forming a *lateral superlattice*. For such a periodic structure we expect energy bands, but they are back-folded into the small Brillouin zone of the step lattice. Its boundaries lie at $k = \pm\pi L$ in the direction perpendicular to the steps, where L is the step spacing (figure 49a). Such back-foldingf the bands has been observed for the $n = 1$ image state on Cu(100) by Wang *et al.* (1996b) (see figure 49b). A simple model potential for the steps, that is a one-dimensional train of δ functions produces the nearly-free-

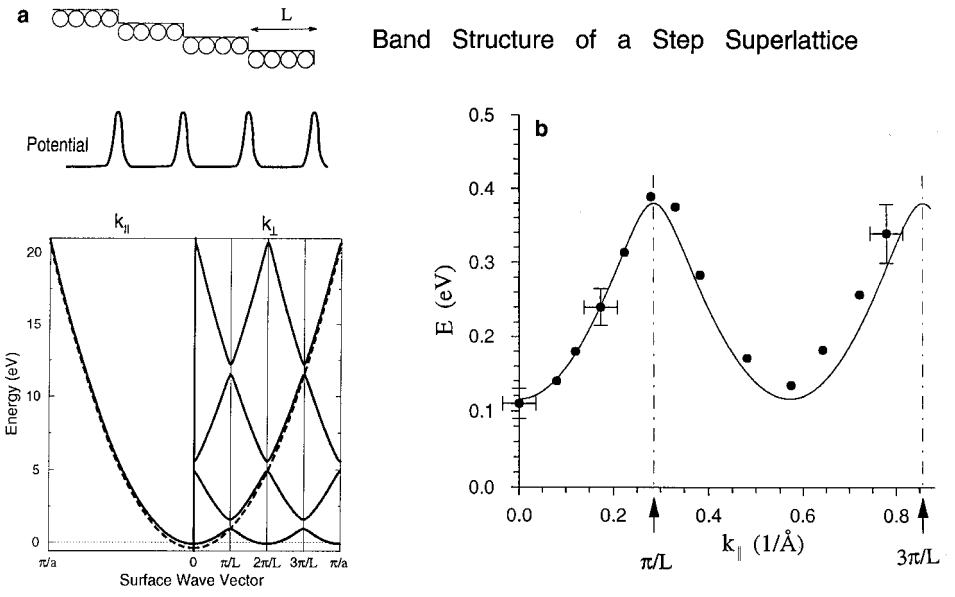

Figure 49. (a) Schematic band structure of a lateral superlattice induced by steps. (b) Band dispersion of an image state on a stepped Cu(100) surface measured by two-photon photoemission. In the direction perpendicular to the steps the bands are back-folded at the Brillouin zone boundaries of the reciprocal step lattice (Wang *et al.* 1996b).

electron-like band structure in figure 49a. With respect to the flat surface we notice two changes; the bottom of the band is shifted up in energy, since the average potential is higher after including the repulsive barriers, and the continuity is broken at the boundaries of the step-induced Brillouin zone, where small gaps open up. The shift of the surface band has been observed with STM and photoemission spectroscopy for the p_z-like surface state on Cu(111) and Au(111) (Crommie *et al.* 1993a, Avouris and Lyo 1994, Sánchez *et al.* 1995). From these measurements, one estimates a transmission coefficient through the step of the order of 0.6 for the lowest-energy electrons at the bottom of the band (Sánchez *et al.* 1995).

Steps have a significant influence on magnetic properties, particularly the *anisotropy*. Because of the broken azimuthal symmetry, magnetic thin films on stepped surfaces are expected to exhibit an 'easy' axis for the in-plane magnetization, which can be either parallel or perpendicular to the steps. For example, Fe films on stepped W(001) have an easy magnetization direction perpendicular to the steps (Chen and Erskine 1992); Co on stepped Cu (Berger *et al.* 1992, Nguyen-Van-Dan *et al.* 1997) and Fe on stepped Ag(100) (Kawakami *et al.* 1996), on the other hand, show an easy axis parallel to the steps. In Fe films grown on W(110) it is possible to overcome the bulk-related anisotropy by step anisotropy when increasing the number of steps of the growing Fe(110) film by elevating the growth temperature (Hillebrands *et al.* 1987). This causes the in-plane easy axis to rotate. A similar in-plane rotation of the easy axis can be induced by a submonolayer of foreign atoms adsorbed at steps (Buckley *et al.* 1995, Weber *et al.* 1995). Two general mechanisms can be invoked for step-induced anisotropy, that is a specific orientation of 3d orbitals at steps and magnetoelastic anisotropy induced by strain in the growing film. The latter is particularly prominent for bcc films deposited on fcc substrates

(compare section 2.1), such as Fe(100) on Ag or Au(100), where the lattice is matched in plane but not in the perpendicular direction. High step density at the substrate considerably alters the magnetic properties of the film (Cabanel *et al.* 1990). Even though vertical mismatch does not affect the growth of Co on stepped Cu(001), a step-induced uniaxial anisotropy has been observed and traced to the elastic strain field at steps (Oepen *et al.* 1993, Krams *et al.* 1994). In this system it can be seen how the twofold step-induced anisotropy superimposes itself onto the fourfold symmetry, which is characteristic for the Co(100) films grown on Cu(100) (Krams *et al.* 1992). At a certain thickness, the easy axis of magnetization rotates from perpendicular to parallel to the steps (Oepen *et al.* 1993, Krams *et al.* 1994, Wulfhekel *et al.* 1994). Here, the interface anisotropy competes with surface and bulk terms, and an increasing density of interface steps delays the transition (Wulfhekel *et al.* 1994).

Using the stepped surface of a non-magnetic material it is possible to create lateral magnetic superlattices by step decoration and step-flow growth of ferromagnets. The magnetic properties of these systems have not been investigated yet, but we can expect a strong competition between in-plane shape anisotropies and interface-related perpendicular anisotropy. By increasing the film coverage up to a monolayer, one covers the gap between one and two dimensions. This is of particular interest for observing the onset of magnetism in Ising-like systems (see section 4.2) (Elmers *et al.* 1994). Long-range magnetic order is not possible in one-dimensional systems at finite temperatures as long as the magnetic interaction remains short-range.

7. Zero-dimensional systems: particles and arrays

As magnetic particles become smaller, they pass through a series of *magnetic phases*. The first change comes when their size shrinks below a domain wall thickness (typically 0.1–1 μm), which favours single-domain behaviour. Such particles have been the mainstay of magnetic storage media. Farther down in size, at about 10–20 nm one approaches the superparamagnetic limit where a spontaneous flip of the magnetization can happen by thermal activation at room temperature (see section 8.1). Yet smaller particles exhibit rapid spin flips. Macroscopic quantum tunnelling comes into play as a new mechanism for spin flip, particularly when thermally activated switching is frozen out (Awschalom and diVicenzo 1995). At the lowest length scales, one finds magnetic molecules and clusters with a well defined level structure (Yang *et al.* 1981, Klots *et al.* 1991, Gatteschi *et al.* 1994, Wang *et al.* 1996a). Small particles have a large *surface-to-bulk ratio*, for example about 1 to 1 for a fcc cube with four cubic lattice constants on each side (1.4 nm for Ni) and still 1 to 9 for a 10 nm Ni cube. Therefore magnetic properties are strongly affected by the surface. Enhanced magnetism, as well as a magnetically disordered surface region are possible, as discussed in the context of surfaces (section 5).

Reduced magnetism has been implied from the magnetic hysteresis of $NiFe_2O_4$ nanoparticles (6.5 nm diameter). The analysis suggests a magnetized core surrounded by a magnetically disordered shell. The fluctuating moments in the shell can be frozen out into a spin glass below 50 K (Kodama *et al.* 1996). Thermally activated magnetic switching of Ni wires with diameters of 40–100 nm proceeds with an activation volume much smaller than the total (Wernsdorfer *et al.* 1996) (compare section 8.1). Ni carbonyl clusters have a magnetically dead surface layer due to the carbonyl ligands, similar to carbonyl-covered Ni surfaces (Van Leeuwen *et al.* 1994).

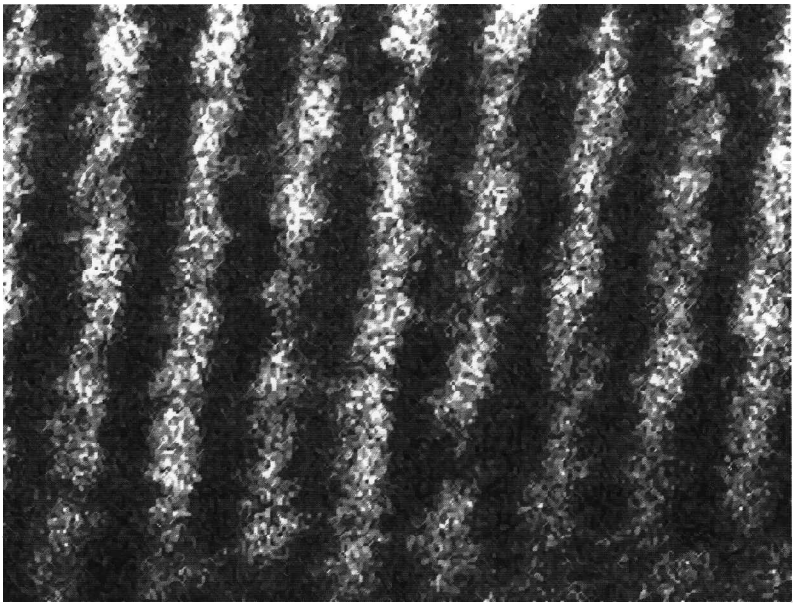

Figure 50. Magnetic bit pattern imaged by SEMPA. The bit size is $0.13\,\mu m \times 3\,\mu m$, corresponding to a storage density of $1.7\,Gbit\,in^{-2}$. Jagged domain boundaries give rise to fluctuations in the readout signal—see the work by Pierce *et al.* (1989) and Scheinfein *et al.* (1990).

Enhanced magnetism is unusual in particles, but it can be promoted by surface treatment. An enhanced Curie temperature has been found in $MnFe_2O_4$ particles with diameters in the 5–25 nm range (Tang *et al.* 1991). In this case, the enhancement could be described by three-dimensional finite-size scaling (see section 4.2). Oxygen adsorbed on Fe particles gives rise to ferromagnetic order (**Bø**dker *et al.* 1994). Magnetic particles coated by cobalt ferrite exhibit a large magnetic anisotropy that makes them more stable against thermal polarization reversal (Mallinson 1987, chapter 3). Antiferromagnetic particles exhibit uncompensated spins (Kodama *et al.* 1997).

Particle arrays are at the heart of magnetic storage media, such as embedded particles in magnetic tape and segregated grains in magnetic discs (see section 8.1). Looking at the micromagnetics of stored bits with spin-resolving microscopes reveals a rather irregular domain structure with jagged edges (figure 50). These irregularities contribute significantly to the read-out noise, requiring typically 10^3 particles to form a stored bit. Regular arrays of particles are particularly desirable for achieving the ultimate goal of single-particle-per-bit recording (Lederman *et al.* 1994, Chou *et al.* 1994, New *et al.* 1995a, b, Hehn *et al.* 1996, Runge *et al.* 1996, O'Barr *et al.* 1997). Although optical lithography has difficulties reaching the small bit sizes of high-end storage media, there is ample room to get insight into the magnetic coupling between particles and into domain formation within individual particles as they are switched by an external field (figure 51). It is now possible to detect the magnetic fine structure down to the level of single flux quanta in nanowires ($40\,nm \times 2\,\mu m$) (Beeli *et al.* 1995). Particles serve as model kit for understanding domains, domain walls and magnetization reversal. Micromagnetic modelling typically includes a minimization over several energy terms, such as the exchange energy, crystalline anisotropy, the magnetostatic energy of the magnetic moment in the demagnetizing field, and the

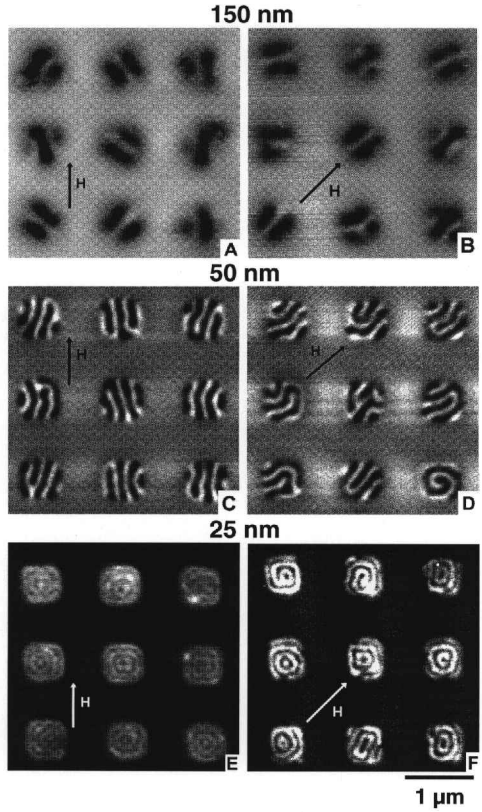

Figure 51. Domain structure in an array of magnetic dots with different thicknesses, as seen by MFM (Hehn *et al.* 1996).

Zeeman energy of the magnetic moment in an external field (Bertram and Zhu 1992, Mosdiel *et al.* 1996). To see what might happen to particle–particle interactions at sublithographic dimensions one can look at the magnetic behaviour of random arrays of magnetic islands (Scheinfein *et al.* 1996). They exhibit distinct magnetic phases, such as perpendicularly magnetized random antiferromagnet (island diameters, less than 3 nm), in-plane superparamagnet (diameters, 3–6 nm) and in-plane ferromagnet (diameters, greater than 6 nm).

8. Applications in magnetic data storage

Magnetic nanostructures are starting to play a role in technology, particularly in non-volatile magnetic data storage (figures 52, 53). Reviews have been given by White (1984), Mallison (1987), Mee and Daniel (1988), Bertram and Zhu (1992), Grochowski and Thompson (1994), Prinz and Hathaway (1995) and Kryder (1996). Applications focus onto the two key parts of storage: media (Lambeth *et al.* 1996) and reading heads (Brug *et al.* 1996). The fundamental limits to this technology are far beyond the current state of the technology, leaving ample room for continuing the exponential growth in performance that magnetic storage has experienced in the past. New combinations with semiconductor technology are developing, such as magnetic random access memories (MRAMs) (Daughton 1992, Everitt *et al.* 1997, Gallagher *et al.* 1997) where the storage capacitor of a traditional semiconductor

memory is replaced by a non-volatile magnetic dot. Several other applications of small magnetic structures have been discussed by Falicov *et al.* (1990), such as magneto-optic recording media, magnetoelastic devices, high-energy-product permanent magnets, and the integration of magnetic and semiconductor devices onto a single chip.

8.1. *Storage media*

The storage media to today's magnetic *hard disc drives* may be viewed as an array of magnetic nanoparticles. The magnetic coating of the disk consists of a ternary Co–Pt–Cr mixture which segregates into magnetic Co–Pt grains. These grains are magnetically separated by Cr at the grain boundaries (for a review see Bertram and Zhu (1992), and for new developments see Lambeth *et al.* 1996). Typical grain sizes are 10–20 nm, using about 10^3 grains per bit at a recording density of 1 Gbit in^{-2} for commercial devices. The grains segregate randomly, which introduces statistical noise into the read-out signal due to the variations in grain size, coercivity and domain structure. This explains the large number of grains that are required to reduce these fluctuations in a device.

How far can the magnetic storage density improve? A fundamental limit is given by thermal flipping of the bits as the grains become smaller and the energy barrier ΔE between the two stable magnetizations along the easy axis becomes comparable with kT. Eventually, the *superparamagnetic limit* is reached, where individual grains stay magnetized, but their orientations fluctuate thermally. For estimating the flip rate R we may write down a simple thermally activated process, where an attempt frequency υ is multiplied by the probability per attempt, which is given by the Boltzmann factor (Mee 1964, Mallinson 1987, Sellmyer *et al.* 1998):

$$R = \upsilon \exp\left(\frac{-\Delta E}{kT}\right). \tag{19}$$

The energy ΔE in the exponent dominates the flip rate. An estimate for the barrier can be obtained from the energy of the magnetic moment $M_s V$ in the demagnetizing field H_d which is given by

$$\Delta E = \tfrac{1}{2} M_s V H_d, \tag{20}$$

where $M_s = 2.2\,\mu_B\,\text{atom}^{-1} = 1700\,\text{erg G}^{-1}\,\text{cm}^{-3}$ is the saturation magnetization of Fe and V the volume of the particle. For a uniform rotation of the magnetization in a needle-shaped particle (top of figure 54) one has $H_d = 2\pi M_s$, but this represents an upper limit for the barrier. In a more realistic model the particle breaks up into domains during the flip and a reduced value $H_d \approx M_s$ is more appropriate (Mallinson 1987) (compare also Braun (1994) for micromagnetic models). For the less important attempt frequency, one may use the Larmor frequency at this field:

$$\upsilon \approx \upsilon_L = \frac{\omega_L}{2\pi} = \frac{eH_d}{4\pi mc}, \tag{21}$$

which is $2.4 \times 10^9\,\text{s}^{-1}$ in this example. For a particle with volume $V = (10\,\text{nm})^3$ the flip probability per attempt is still extremely small, about $e^{-35} \approx 7 \times 10^{-16}$, but multiplied by the attempt frequency the flip rate comes out to be about one per week. On the other hand, just doubling the particle dimensions to $V = (20\,\text{nm})^3$ produces an astronomical flip time of once every 10^{104} years. This transition happens so

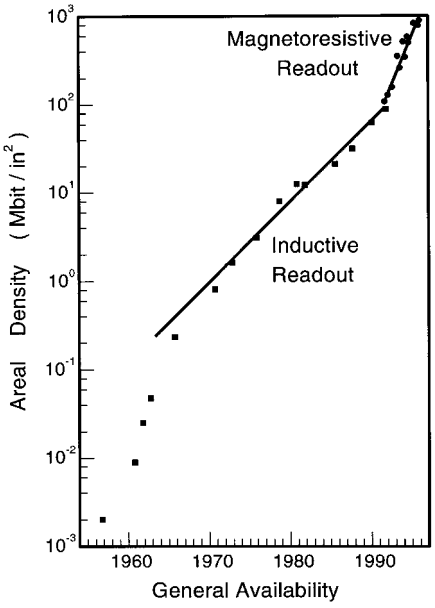

Figure 52. Exponential growth of commercially available magnetic storage density against time (after White (1984) and Grochowski and Thompson (1994)). The introduction of magnetoresistive reading heads in the early 1990s (●) doubled the growth rate.

sharply since the volume V, that is the third power of the particle size, appears in the exponent of the extremely small Boltzmann factor.

Such a back-of-the-envelope estimate of the superparamagnetic limit has still wide margins. The critical particle size increases when considering magnetization reversal that starts at a localized nucleus or vortex. In this case, the barrier becomes proportional to the sample cross-section multiplied by a domain wall energy, instead of being proportional to the volume (Braun 1994). Magnetic force microscopy images of a single needle-shapeed Fe_2O_3 particle (300 nm × 65 nm) present a rather complex thermal switching behaviour that may require a spectrum of energy barriers (Lederman *et al.* 1994). The magnetization reversal in individual Ni wires with diameters of 40–100 nm did follow the Arrhenius law for thermal activation across a barrier, but the active volume was much smaller than that of the wires (Wernsdorfer *et al.* 1996).

For typical magnetic storage media, the superparamagnetic limit imposes a minimum particle size of about 10 nm, that is a maximum recording density of several terabits per square inch (Lambeth *et al.* 1996). This is almost four orders of magnitude higher than the density of 1 Gbit in^{-2} found in top-of-the-line disc drives today. While the current particle size is already close to the superparamagnetic limit, the number of particles per bit is still more than 10^3. There are many signal-to-noise issues on the way towards reducing this number and reaching the theoretical limit. Inconsistent switching of different particles and an irregular domain structure require averaging over many particles. Controlling coercivity, size, orientation and position of magnetic nanoparticles will be essential for reducing the number of particles needed to store a bit. A number of such efforts are under way (Kryder 1996, p. 28). For example, a large crystalline anisotropy can produce a higher switching barrier than the shape anisotropy discussed above. Single-domain nanoparticles with

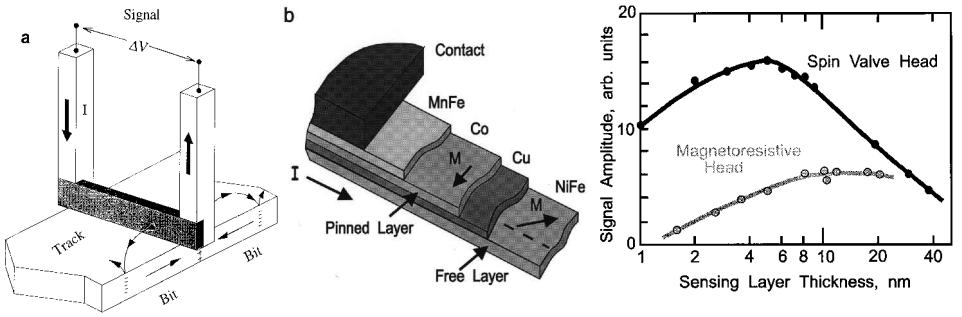

Figure 53. Schematic diagram of magnetoresistive reading heads for hard discs (Grochowski and Thompson 1994, Heim *et al.* 1994). (a) Initial design, based on the AMR of Permalloy ($Ni_{0.8}Fe_{0.2}$). (b) Latest Spin valve design, based on GMR of a Co/Cu/Permalloy sandwich. (c) Comparison. Note the higher output and smaller dimensions of the spin valve head, which bring it into the single-digit nanometre regime.

high saturation magnetization and coercivity are being optimized for that purpose (Liou *et al.* 1996). The orientation of segregated grains can be controlled using multilayer structures where the first layer acts as seed for small grains and subsequent layers shape the crystalline orientation for the desired anisotropy (Lambeth *et al.* 1996). A further improvement would be the move from longitudinal to perpendicular recording, where the demagnetizing field does not destabilize the written domains. Layered structures can be designed to favour a perpendicular magnetization due to interface anisotropy (Wang *et al.* 1994).

The ultimate goal in magnetic storage is *single-particle-per-bit* or quantized recording. It is aimed at producing single-domain particles close to the superparamagnetic limit with uniform switching properties. Lithography is currently the method of choice for producing regular arrays of uniform magnetic dots (Lederman *et al.* 1994, Chou *et al.* 1994, New *et al.* 1995a, b, Chou *et al.* 1996, Hehn *et al.* 1996, Levy *et al.* 1996, Runge *et al.* 1996, Everitt *et al.* 1997, O'Barr *et al.* 1997). Dot arrays with a density of 65–250 Gbit in^{-2} have been produced by electron-beam lithography (Chou *et al.* 1996). Self-assembly schemes are being considered as an easier alternative (Himpsel *et al.* 1997). Even with the many remaining difficulties it becomes clear from a look at the fundamental limits that magnetic storage has much room to continue its rapid development and that the control of magnetic nanostructures will play a key role for further advances. There is good reason to believe that the exponential growth in storage density will continue. Since the 1950s we have experienced an increase of six orders of magnitude (figure 52). Every three years the density doubles and the cost per bit is reduced by a factor of two (Simonds 1995). So far, that has been achieved without lithographic patterning of the storage medium, in contrast with the more mature semiconductor memory.

8.2. *Sensors*

The other component of today's magnetic disc drives, that is the *reading head*, is undergoing revolutionary changes that rely on nanostructured magnetic materials (Brug *et al.* 1996, Kryder 1996, p. 23). The traditional inductive pick-up of the magnetic signal is replaced by a magnetoresistive sensor in state-of-the-art devices (figures 52, 53). There exist various mechanisms of magnetoresistance as explained in sections 3.2.2 and 5.5. Of these, AMR in Permalloy ($Ni_{0.8}Fe_{0.2}$) and GMR in

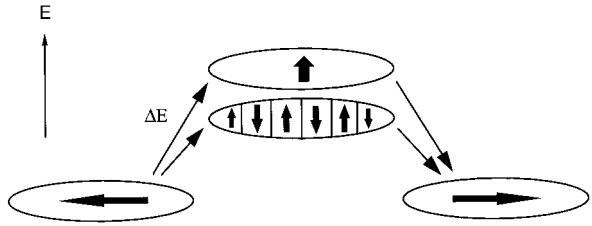

Figure 54. Superparamagnetic limit of the magnetic storage density. The time for thermally activated magnetization reversal drops precipitously at about 10 nm particle size since the energy barrier decreases rapidly. This corresponds to a storage density of several terabits per square inch, 10^3 times higher than present densities.

Permalloy/Cu/Co multilayers are utilized in reading heads. Currently, reading heads in high-end disc drives are based on the 2% AMR of Permalloy (figure 53). The resistance is highest for the current parallel to the magnetization and lowest perpendicular to it, producing a sinusoidal orientation dependence. The magnetic stray field between adjacent bits with opposite orientation rotates the magnetization in the permalloy film with respect to the current and thus induces a resistance change. That is directly convertible into a read-out voltage. It is desirable to have the magnetization of the film oriented at 45° with respect to the current, that is, at the zero crossings of the sinusoidal magnetoresistance curve where the response to a given rotation is largest and linear.

GMR in magnetic multilayers can exceed 200% in high fields (10^5 Oe) but drops to about 10% at the low switching fields of 10 Oe that are required in reading heads (Heim *et al.* 1994, Brug *et al.* 1996). Even small improvements in magnetoresistance translate into significant technological improvements, since the efficiency of a magnetoresistive reading head increases quadratically with the magnetoresistance (Thompson *et al.* 1975). A measure of the sensitivity in low fields is the magnetoresistance per Oersted $(\delta R/R)/H$. Values of 0.2–1% Oe^{-1} have been reached using GMR (Burkett *et al.* 1996, Parkin and Rabedau 1996) and CMR (Eckstein *et al.* 1996, Sun *et al.* 1997) and up to 5% Oe^{-1} by tunnelling (Moodera and Kinder 1996). The junction resistance is low in GMR, producing a small voltage but substantial signal power. Tunnelling junctions are characterized by high resistance, which makes them sensitive to Johnson noise but keeps the power consumption low.

A typical sensor structure is shown in figure 53b). It is often termed a *spin valve* because the majority spin current is turned on or off by the external magnetic field. In addition to the characteristic three layers of GMR structures there is a fourth layer in a spin valve that fixes the magnetization of one of the ferromagnetic layers. This way it is not necessary to have antiparallel coupling between the two ferromagnetic layers to get the GMR effect. The fourth layer is an antiferromagnet (FeMn or NiO) with a specific domain orientation. It orients the adjacent ferromagnetic layer via the exchange interaction without disturbing the overall magnetic field configuration (exchange biasing). Present activities are directed towards lowering the switching field while keeping a large magnetoresistance. To obtain the best of both characteristics, one combines a magnetically soft Permalloy layer for easy switching with a high-spin Co layer that enhances the magnetoresistance (Heim *et al.* 1994, Tsang *et al.* 1994). Alternatively, one can use two permalloy layers (Hamakawa *et al.* 1996) and give the interfaces an additional Co coating (Parkin 1992). Spin valve sensors

have been moving through the prototype state, and manufacturing issues have been addressed (Gurney *et al.* 1997). The first commercial product was announced by IBM in late 1997. A future avenue is the use of wire and stripe structures (Blondel *et al.* 1994, Piraux *et al.* 1994, Liu *et al.* 1995, Ono and Shinjo 1995, Oepts *et al.* 1996). The goal is to have the current flowing perpendicular to the interfaces where the magnetoresistance is typically a factor of five higher because all electrons experience the spin-dependent interface scattering (see section 5.5).

Another type of non-volatile magnetic storage device avoids moving parts altogether, at the expense of having to pattern the storage medium. This is a combination of magnetic memory elements with semiconductor circuits that sense and amplify the magnetic state (MRAM) (Daughton 1992, Tang *et al.* 1995, Everitt *et al.* 1997, Gallagher *et al.* 1997). Some of the architectures are reminiscent of the classic magnetic core memory, where a magnetic storage element sits at the intersection of crossed write–read wires. Magnetic tunnelling structures are likely to play a role here (see section 5.5).

Farther into the future are *logic devices* based on magnetic nanostructures. A bipolar spin switch has been demonstrated that acts like a transistor, although with gain figures far from being practical for electronic devices (Johnson 1994). The structure consists of a ferromagnet–non-magnet–ferromagnet sandwich smilar to that in GMR devices with the current perpendicular to the layers. Likewise, the explanation is closely related to the injection of a spin-polarized current from one ferromagnet into the non-magnet. This creates a splitting between the chemical potentials of opposite spins in the non-magnet which is sensed as a voltage by the other ferromagnetic layer (Johnson 1994, Fert and Lee 1996).

The number of creative ideas for novel devices involving magnetic nanostructures is growing rapidly. Everything from magneto-optic to magneto-elastic and integrated magnetic–semiconductor devices has been fair game. Not all these ideas will be converted into useful devices, but there is a wide-open territory to be covered. Current magnetic device structures are still rather simple compared with semiconductor devices. Many structures, such as recording media, are not even patterned. Looking at this simplicity it becomes clear that magnetoelectronics has a wide-open territory for further growth.

Acknowledgment

This work was supported by the National Science Foundation under award Nos. DMR-9624753, DMR-9632527 and DMR-9531009.

References

Aldén, M., Skriver, H. L., Mirbt, S., and Johansson, B., 1992, *Phys. Rev. Lett.*, **69,** 2296.

Alivisatos, A. P., Harris, T. D., Carrol, P. J., Steigerwald, M. L., and Brus, L. E., 1989, *J. Chem. Phys.*, **90,** 3463.

Allenspach, R., 1994, *J. Magn. magn. Mater.*, **129,** 160,

Allenspach, R., and Bischof, A., 1992, *Phys. Rev. Lett.*, **69,** 3385.

Alvarado, S. F., 1995, *Phys. Rev. Lett.*, **75,** 513.

Alvarado, S. F., and Renaud, P., 1992, *Phys. Rev. Lett.*, **68,** 1387.

Anderson, G. W., Hanf, M. C., and Norton, P. R., 1995, *Phys. Rev. Lett.*, **74,** 2764.

Anderson, G. W., Ma, P., and Norton, P. R., 1996, *J. appl. Phys.*, **79,** 5641.

Avouris, Ph., and Lyo, I.-W., 1994, *Science*, **264,** 942.

Avouris, Ph., Lyo, I.-W., Walkup, R. E., and Hasegawa, Y., 1994, *J. Vac. Sci. Technol.* B, **12,** 1447.
Awschalom, D. D., and DiVincenzo, D. P., 1995, *Phys. Today*, April, 43.
Awschalom, D. D., Smyth, J. F., Grinstein, G., DiVincenzo, D. P., and Loss, D., 1992, *Phys. Rev. Lett.*, **68,** 3092.
Bader, S. D., 1990, *Proc. Inst. elect. electron. Engrs*, **78,** 909.
Bader, S. D., and Moog, E. R., 1987, *J. Appl. Phys.,* **61,** 3729.
Baibich, M. N., Broto, J. M., Fert, A., Nguyen-Van-Dan, F., Petroff, F., Etienne, P., Creuzet, G., Friedrich, A., and Chazelas, J., 1988, *Phys. Rev. Lett.,* **61,** 2472.
Ballentine, C. A., Fink, R. L., Araya-Pochet, J., and Erkskine, J. L., 1990, *Phys. Rev.* B, **41,** 2631.
Bass, J., Yang, Q., Lee, S. F., Holody, P., Loloee, R., Schroeder, P. A., and Pratt, W. P., 1994, *J. appl. Phys.*, **75,** 6699.
Bastard, G., 1988, *Wave Mechanics Applied to Semiconductor Heterostructures* (Les Ulis: Les Editions de Physique).
Bauer, E., 1958, *Z. Kristallogr.*, **110,** 372.
Bauer, E., and van der Merwe, J. H., 1986, *Phys. Rev.*, **33,** 3657.
Beeli, C., Doudin, B., and Stadelmann, P., 1995, *Phys. Rev. Lett.*, **75,** 4630.
Berger, A., Linke, U., and Oepen, H., 1992, *Phys. Rev. Lett.*, **68,** 839.
Berkowitz, A. E., Mitchell, J. R., Carey, M. J., Young, A. P., Zhang, S., Spada, F. E., Parker, F. T., Hutten, A., and Thomas, G., 1992, *Phys. Rev. Lett.*, **68,** 3745.
Bertram, H. N., and Zhu, J.-G., 1992, *Solid St. Phys.*, **46,** 271.
Betzig, E., Trautman, J. K., Wolfe, R., Gyorgy, E. M., Finn, P. L., Kryder, M. H., and Chang, C.-H., 1992, *Appl. Phys. Lett.*, **61,** 142.
Binasch, G., Grünberg, P., Saurenbach, F., and Zinn, W., 1989, *Phys. Rev.* B, **39,** 4828.
Blakemore, R. P., and Frankel, R. B., 1981, *Sci. Am.*, **245,** 58.
Bloemen, P. J. H., Johnson, M. T., van de Vorst, M. T. H., Coehoorn, R., de Vries, J. J., Jungblut, R., aan de Stegge, J., Reinders, A., and de Jongee, W. J. M., 1994, *Phys. Rev. Lett.*, **72,** 764.
Blondel, A., Meier, J. P., Doudin, B., and Ansermet, J.-Ph., 1994, *Appl. Phys. Lett.*, **65,** 3019.
Blügel, S., Drittler, B., Zeller, R., and Dederichs, P. H., 1989, *Appl. Phys.* A, **49,** 547.
Bødker, F., Mørup, S., and Lindroth, S., 1994, *Phys. Rev. Lett.*, **72,** 282.
Borchers, J. A., Nieuwenhuys, G., Salamon, M. B., Flynn, C. P., Du, R., Erwin, R. W., and Rhyne, J. J., 1988, *J. Phys., Paris*, **49,** C3–1685.
Borstel, H., Thörner, G., Donath, M., Dose, V., and Goldmann, A., 1985, *Solid St. Commun.*, **55,** 469.
Bos, L. W., and Lynch, D. W., 1970, *Phys. Rev.* B, **2,** 4567.
Bott, M., Michely, T., and Comsa, G., 1992, *Surf. Sci.*, **272,** 161.
Bramwell, S. T., and Holdsworth, P. C. W., 1993, *J. Phys., condens. Matter*, **5,** L53.
Braun, H.-B., 1994, *Phys. Rev.* B, **50,** 16 501.
Braun, J., and Toennies, J. P., 1997, *Surf. Sci. Lett.* (to be published).
Brookes, N. B., Chang, Y., and Johnson, P. D., 1991, *Phys. Rev. Lett.*, **67,** 354.
Brookes, N. B., Clarke, A., and Johnson, P. D., 1992, *Phys. Rev.* B, **46,** 237.
Brookes, N. B., Clarke, A., Johnson, P. D., and Weinert, M., 1990, *Phys. Rev.* B, **41,** 2643.
Brug, J. A., Tran, L., Bhattacharyya, M., Nickel, J. H., Anthony, T. C., and Jander, A., 1996, *J. appl. Phys.*, **79,** 4491.
Bruno, P., 1995, *Phys. Rev.* B, **52,** 411.
Bruno, P., and Chappert, C., 1991, *Phys. Rev. Lett.*, **67,** 1602, 2592.
Buckley, M. E., Schumann, F. O., and Bland, T. A. C., 1995, *Phys. Rev.* B, **52,** 6596.
Burkett, S. L., Yang, J., Pillai, D., and Parker, M. R., 1996, *J. vac. Sci. Technol.* B, **14,** 3131.
Burton, W. K., Cabrera, N., and Frank, F. C., 1951, *Phil. Trans. E. Soc.* A, **243,** 299.
Cabanel, R., Etienne, P., Lequien, S., Barthélémy, A., and Fert, A., 1990, *J. appl. Phys.*, **67,** 5409.

Camarero, J., Graf, T., de Miguel, J. J., Miranda, R., Kuch, W., Zharnikow, M., Dittschar, A., Schneider, C. M., and Kirschner, J., 1996, *Phys. Rev. Lett.*, **76,** 4428.
Camblong, H. E., Zhang, S., and Levy, P. M., 1993, *Phys. Rev.* B, **47,** 4735.
Camley, R. E., Rahman, T. S., and Mills, D., 1983, *Phys. Rev.* B, **27,** 261.
Carbone, C., Vescovo, E., Rader, O., Gudat, W., and Eberhardt, W., 1993, *Phys. Rev. Lett.*, **71,** 2805.
Carl, A., and Weller, D., 1995, *Phys. Rev. Lett.*, **74,** 190.
Celotta, R. J., Gupta, R., Scholten, R. E., and McClelland, J. J., 1996, *J. Appl. Phys.*, **79,** 6079; see also http://physics.nist.gov/Divisions/Div841/Gp3/epg-files/atom-lines-proj.html.
Chambliss, D. D., Wilson, R. J., and Chiang, S., 1991, *Phys. Rev. Lett.*, **66,** 1721.
Chen, J., and Erskine, J. L., 1992, *Phys. Rev. Lett.*, **68,** 1212.
Chou, S. Y., Krauss, P. R., and Kong, L., 1996, *J. appl. Phys.*, **79,** 6101.
Chou, S. Y., Wei, M., Krauss, P. R., and Fischer, P. B., 1994, *J. Vac. Sci. Technol.* B, **12,** 3695.
Condon, N. G., Leibsle, F. M., Lennie, A. R., Murray, P. W., Vaughan, D. J., and Thornton, G., 1995, *Phys. Rev. Lett.*, **75,** 1961.
Cook, R. F., 1986, *J. Mater. Res.*, **1,** 852.
Crampin, S., 1993, *J. Phys. condens. Matter*, **5,** 4647.
Crampin, S., De Rossi, S., and Ciccacci, F., 1996, *Phys. Rev.* B, **53,** 13 817.
Crommie, M. F., Lutz, C. P., and Eigler, D. M., 1993a, *Nature*, **363**, 524; 1993b, *Science*, **262,** 218; see also http://eagle.almaden.ibm.com/vis/stm/gallery.html.
Daalderop, G. H. O., Kelly, P. J., and Schuurmans, M. F. H., 1994, *Phys. Rev.* B, **50,** 9989.
Daughton, J. M., 1992, *Thin Solid Films*, **216,** 162.
Davies, A., Stroscio, J. A., Pierce, D. T., and Celotta, R. J., 1996, *Phys. Rev. Lett.*, **76,** 4175.
De Groot, F. M. F., 1994, *J. Electron Spectrosc.,* **67,** 529.
De la Figuera, J., Huerta-Garnica, M. A., Prieto, J. E., Ocal, C., and Miranda, R., 1995, *Appl. Phys. Lett.*, **66,** 1006.
De Rossi, S., Ciccacci, F., and Crampin, S., 1996, *Phys. Rev. Lett.*, **77,** 908.
Domb, C., 1973, *J. Phys.* A, **6,** 1296.
Donath, M., 1989, *Appl. Phys.* A, **49,** 351.
Donath, M., Gubanka, B., and Passek, F., 1996, *Phys. Rev. Lett.*, **77,** 5138.
Donath, M., Passek, F., and Dose, V., 1993, *Phys. Rev. Lett.*, **70,** 2802.
Dose, V., 1985, *Surf. Sci. Rep.*, **5,** 337.
Duden, T., and Bauer, E., 1996, *Phys. Rev. Lett.*, **77,** 2308.
Dürr, W., Taborelli, M., Paul, O., Germar, R., Gudat, W., Pescia, D., and Landolt, M., 1989, *Phys. Rev. Lett.*, **62**, 206.
Eberhardt, W., and Plummer, E. W., 1980, *Phys. Rev.* B, **21,** 3245.
Echenique, P. M., and Pendry, J. B., 1990, *Prog. Surf. Sci.*, **32,** 111.
Eckardt, H., Fritsche, L., and Noffke, J., 1984, *J. Phys.* F, **14,** 97.
Eckstein, J. N., Bozovic, I., O'Donnell, J., Onellion, M., and Rzchowski, M., 1996, *Appl. Phys. Lett.*, **69,** 1312.
Edwards, D. W., Mathon, J., and Muniz, R. B. 1994, *Phys. Rev.* B, **50,** 16 066.
Edwards, D. M., Mathon, J., Muniz, R. B., and Phan, M. S., 1991, *Phys. Rev. Lett.*, **67,** 493.
Egelhoff, W. F., Chen, P. J., Powell, C. J., Stiles, M. D., McMichael, R. D., Lin, C.-L., Sivertsen, J. M., Judy, J. H., Takano, K., and Berkowitz, A. E., 1996, *J. appl. Phys.*, **80,** 5183.
Egelhoff, W. F., Jr, and Jacob, I., 1989, *Phys. Rev. Lett.*, **62,** 921.
Ehrichs, E. E., Smith, W. F., and de Lozanne, A. L., 1992, *Ultramicroscopy*, **42–44,** 1438.
Ehrlich, G., and Hudda, F. G., 1966, *J. chem. Phys.*, **44,** 1039.
Elmers, H. J., Hauschild, J., Fritzsche, H., Liu, G., Gradmann, U., and Köhler, U., 1995, *Phys. Rev. Lett.*, **75,** 2031.
Elmers, H. J., Hauschild, J., Höche, H., and Gradmann, U., 1994, *Phys. Rev. Lett.*, **73,** 898.

ELMERS, H. J., HAUSCHILD, J., LIU, G. H., and GRADMANN, U., 1996, *J. appl. Phys.*, **79,** 4985.
ELMERS, H. J., LIU, G., and GRADMANN, U., 1989, *Phys. Rev. Lett.*, **63,** 566.
ENGEL, B. N., ENGLAND, C. D., VAN LEEUWEN, R. A., WIEDMANN, M. H., and FALCO, C. M., 1991, *Phys. Rev. Lett.*, **67,** 1910.
ENGEL, B. N., WIEDMANN, M. H., and FALCO, C. M., 1994, *J. appl. Phys.*, **75,** 6401.
ERICKSON, R. P., and MILLS, D. L., 1991, *Phys. Rev.* B, **44,** 11 825.
ERIKSSON, O., ALBERS, R. C., and BORING, A. M., 1991, *Phys. Rev. Lett.*, **66,** 1350.
ERSCHBAUMER, H., FREEMAN, A. J., FU, C. L., and PODLOUCKY, R., 1991, *Surf. Sci.*, **243,** 317.
EVANS, D. A., ALONSO, M., CIMINO, R., and HORN, K., 1993, *Phys. Rev. Lett.*, **70,** 3483.
EVERITT, B. A., POHM, A. V., and DAUGHTON, J. M., 1997, *J. appl. Phys.*, **81,** 4020.
FALICOV, L. M., 1993, *Braz. J. Phys.*, **23,** p. 233.
FALICOV, L. M., PIERCE, D. T., BADER, S. D., GRONSKY, R., HATHAWAY, K. B., HOPSTER, H. J., LAMBETH, D. N., PARKIN, S. S. P., PRINZ, G., SALAMON, M., SCHULLER, I. K., and VICTORA, R. H., 1990, *J. Mater. Res.*, **5,** 1299.
FARLE, M., BABERSCHKE, K., STETTER, U., ASPELMEIER, A., and GERHARDTER, F., 1993, *Phys. Rev.* B, **47,** 11 571.
FARROW, R. F. C., PARKIN, S. S. P., and SPERIOSU, V. S., 1988, *J. appl. Phys.*, **64,** 5315.
FAWCETT, E., 1988, *Rev. mod. Phys.*, **60,** 209.
FEIBELMAN, P. J., 1995, *Phys. Rev.* B, **52,** 16 845.
FERREIRA, M. S., D'ALBUQUERQUE E CASTRO, J., EDWARDS, D. M., and MATHON, J., 1996, *J. Magn. magn. Mater.*, **154,** L1.
FERT, A., and LEE, S.-F., 1996, *Phys. Rev.* B, **53,** 6554.
FERT, A., VALET, T., and BARNAS, J., 1994, *J. appl. Phys.*, **75,** 6693.
FISCHER, R., FISCHER, N., SCHUPPLER, S., FAUSTER, TH., and HIMPSEL, F. J., 1992, *Phys. Rev.* B, **46,** 9691.
FISHER, M. E., 1974, *Rev. mod. Phys.*, **46,** 597.
FREEMAN, A. J., and WU, R.-Q., 1991, *J. Magn. magn. Mater.*, **100,** 497.
FU, C. L., FREEMAN, A. J., and OGUCHI, T., 1985, *Phys. Rev. Lett.*, **54,** 2700.
FULLERTON, E. E., STOEFFLER, D., OUNADJELA, K., HEINRICH, B., CELINSKI, Z., and BLAND, J. A. C., 1995, *Phys. Rev.* B, **51,** 6364.
GALLAGHER, W. J., PARKIN, S. S. P., LU, Y., BIAN, X. P., MARLEY, A., ROCHE, K. P., ALTMAN, R. P., RISHTON, S. A., JAHNES, C., SHAW, T. M., and XIAO, G., 1997, *J. appl. Phys.*, **81,** 3741.
GARRISON, K., CHANG, Y., and JOHNSON, P. D., 1993, *Phys. Rev. Lett.*, **71,** 2801.
GATTESCHI, D., CANESCI, A., PARDI, L., and SESSOLI, R., 1994, *Science*, **265,** 1054.
GIJS, M. A. M., LENCZOWSKI, S. K. J., and GIESBERS, J. B., 1993, *Phys. Rev. Lett.*, **70,** 3343.
GILMAN, J. J., 1960, *J. appl. Phys.*, **31,** 2208.
GLATZEL, H., SCHNEIDER, R., FAUSTER, T., and DOSE, V., 1992, *Z. Phys.* B, **88,** 53.
GRADMANN, U., 1988, Landolt–Börnstein New Series, Group III, Vol. 19g, edited by H. P. J. Wijn (Berlin: Springer-Verlag) p. 1; 1994, Landolt–Börnstein New Series, Group III, Vol. 24b, *Physics of Solid Surfaces; Electronic and Vibrational Properties*, edited by G. Chiarotti (Berlin: Springer-Verlag), p. 506; 1991, *J. Magn. Magn. Mater.*, **100,** 481.
GRADMANN, U., and PRZYBYLSKI, M., 1987, *Thin Film Growth Techniques for Low-Dimensional Structures*, edited by R. F. C. Farrow, S. S. P. Parkin, P. J. Dobson, J. H. Neave and A. S. Arrott, NATO Advanced Study Institute Series, Series B: Physics, Vol. 163, p. 261.
GREGG, J. F., ALLEN, W., OUNADJELA, K., VIRET, M., HEHN, M., THOMPSON, S. M., and COEY, J. M. D., 1996, *Phys. Rev. Lett.*, **77,** 1580.
GROCHOWSKI, E., and THOMPSON, D. A., 1994, *IEEE Trans. Magn.*, **30,** 3797; see also http://www.almaden.ibm.com:80/.
GRÜNBERG, P., 1989, *Top. appl. Phys.*, **66,** 303.
GRÜNBERG, P., SCHREIBER, R., PANG, Y., BRODSKY, M. B., and SOWERS, H., 1986, *Phys. Rev. Lett.*, **57,** 2442.
GRZELAKOWSKI, K., DUDEN, T., BAUER, E., POPPA, H., and CHIANG, S., 1994, *IEEE Trans. Magn.,* **30,** 4500.

Guillot, C., Ballu, Y., Paigné, J., Lecante, J., Jain, K. P., Thiry, P., Pinchaux, R., Pétroff, Y., and Falicov, L. M., 1977, *Phys. Rev. Lett.*, **39,** 1632.

Güntherodt, G., Hillerbrands, B., Krams, P., Harzer, J. V., Lauks, F., Stamps, R. L., Weber, W., Hartmann, D., Wesner, D. A., Rampe, A., Effner, U. A., Oepen, H. P., Weller, D., Farrow, R. F. C., Engel, B. N., and Falco, C. M., 1994, *Phil. Mag.* B, **70,** 767.

Gunnarson, O., 1976, *J. Phys.* F, **6,** 587.

Gurney, B. A., Speriosu, V. S., Nozieres, J.-P., Lefakis, H., Whilhoit, D. R., and Need, O. U., 1993, *Phys. Rev. Lett.*, **71,** 4023.

Gurney, B. A., Speriosu, V. S., Wilhoit, D. R., Lefakis, H., Fontana, R. E., Heim, D. E., and Dovek, M., 1997, *J. appl. Phys.*, **81,** 3998.

Hamakawa, Y., Hoshiya, H., Kawabe, T., Suzuki, Y., Arai, R., Nakamoto, K., Fuyama, M., and Sugita, Y., 1996, *IEEE Trans. Magn.*, **32,** 149.

Hansen, W., Kotthaus, J. P., and Merkt, U., 1992, *Semicond. Semimetals*, **35,** 279.

Hartmann, D., Weber, Rampe, A., Popovic, S., and Güntherodt, G., 1993, *Phys. Rev.* B, **48,** 16 837.

Hasegawa, Y., and Avouris, Ph., 1993, *Phys. Rev. Lett.*, **71,** 1071.

Hayashi, M., Katayama, T., Suzuki, Y., Taninaka, M., Thiaville, A., and Geerts, W., 1993, *J. Magn. magn. Mater.*, **126,** 547.

Hehn, M., Ounadjela, K., Bucher, J.-P., Rosseaux, F., Decanini, D., Bartenlian, B., and Chappert, C., 1966, *Science*, **272,** 1782.

Heim, D. E., Fontana, R. E., Tsang, C., Speriosu, V. S., Gurney, B. A., and Williams, M. L., 1994, *IEEE Trans. Magn.*, **30,** 316.

Heimann, P., Himpsel, F. J., and Eastman, D. E., 1981, *Solid St Commun.*, **39,** 219.

Heinen, W., Carbone, C., Kachel, T., and Gudat, W., 1990, *J. Electron Spectrosc. Related Phenom.*, **51,** 701.

Heinrich, B., and Cochran, J. F., 1993, *Adv. Phys.*, **42,** 523.

Henderson, M. A., Ramsier, R. D., Yates, J. T., Jr, 1991, *J. vac. Sci. Technol.* A, **9,** 1563.

Henzler, M., 1993, *Surf. Sci.*, **298,** 369.

Henzler, M., and Ranke, W., 1993, *Numerical Data and Functional relationships in Science and Technology*, Landolt–Bernstein New Series, Group III, Vol. 24a (Berlin: Springer), p. 225.

Hillebrands, B., Baumgart, P., and Güntherodt, G., 1987, *Phys. Rev.* B, **36,** 2450.

Himpsel, F. J., 1983, *Adv. Phys.*, **32**, 1: 1986, *Comments condens. Matter Phys.*, **12,** 199; 1991a, *Phys. Rev.* B, **44,** 5966; 1991b, *Phys. Rev. Lett.*, **67,** 2363; 1991c, *Appl. Phys. Lett.*, **58,** 1920.

Himpsel, F. J., and Eastman, D. E., 1978, *Phys. Rev. Lett.*, **41,** 507; 1980, *Phys. Rev.* B, **21,** 3207.

Himpsel, F. J., Jung, T., and Seidler, P. F., 1998, *IBM Jl Res. Dev.*, **42** (to be published).

Himpsel, F. J., Knapp, J. A., and Eastman, D. E., 1979, *Phys. Rev.* B, **19,** 2919.

Himpsel, F. J., Mo, Y. M., Jung, T., Ortega, J. E., Mankey, G. J., and Willis, R. F., 1994, *Superlattices Microstruct.*, **15,** 237.

Himpsel, F. J., and Ortega, J. E., 1994, *Phys. Rev.* B, **50,** 4992.

Himpsel, F. J., and Rader, O., 1995, *Appl. Phys. Lett.*, **67,** 1151.

Hinch, B. J., Koziol, C., Toennies, J. P., and Zhang, G., 1989, *Europhys. Lett.*, **10,** 341.

Hong, K., and Giordano, N., 1995, *Phys. Rev.* B, **51,** 9855.

Hood, R. Q., and Falicov, L. M., 1992, *Phys. Rev.* B, **46,** 8287.

Hopster, H., 1994, *Surf. Rev. Lett.*, **1,** 89.

Houston, J. E., White, J. M., Feibelman, P. J., and Hamann, D. R., 1988, *Phys. Rev.* B, **38,** 12 164.

Huang, F., Kief, M. T., Mankey, G. J., and Willis, R. F., 1994, *Phys. Rev.* B, **49,** 3962.

Hug, H. J., Stiefel, B., Moser, A., Parashikov, I., Klicznik, A., Lipp, D., Güntherodt, H.-J., Bochi, G., Paul, D. I., and O'Handley, R. C., 1996, *J. appl. Phys.*, **79,** 5609.

Hwang, C., and Himpsel, F. J., 1995, *Phys. Rev.* B, **52,** 15 368.

Hybertsen, M. S., and Louie, S. G., 1986, *Phys. Rev.* B, **34,** 5390.

Hylton, T. L., Coffey, K. R., Parker, M. A., and Howard, J. K., 1993, *Science*, **261,** 1021.
Ibach, H., and Lüth, H., 1993, *Solid State Physics* (Berlin: Springer).
Iwasaki, H., Jonker, B. T., and Park, R. L., 1985, *Phys. Rev.* B, **32,** 643.
Jaccodine, R. J., 1963, *J. electrochem. Soc.*, **11,** 524.
Jaklevic, R. C., and Lambe, J., 1975, *Phys. Rev.* B, **12,** 4146.
Jalochowski, M., Bauer, E., Knoppe, H., and Lilienkamp, G., 1992a, *Phys. Rev.* B, **45,** 13 607.
Jalochowski, M., Hoffman, M., and Bauer, E., 1996, *Phys. Rev. Lett.*, **76,** 4227.
Jalochowski, M., Knopppe, H., Lilienkamp, G., and Bauer, E., 1992b, *Phys. Rev.* B, **46,** 4693.
Janak, J. F., 1977, *Phys. Rev.* B, **16,** 255.
Johnson, M., 1994, *J. appl. Phys.*, **75,** 6714.
Johnson, M. T., Coehoorn, R., de Vries, J. J., McGee, N. W. E., aan de Stegge, J., and Bloemen, P. J. H., 1992a, *Phys. Rev. Lett.*, **69,** 969.
Johnson, M. T., Purcell, S. T., McGee, N. W. E., Coehoorn, R., aan de Stegge, J., and Noving, W., 1992b, *Phys. Rev. Lett.*, **68,** 2688.
Jonker, B. T., Krebs, J. J., Prinz, G. A., and Qadri, S. B., 1987, *J. Cryst. Growth*, **81,** 524.
Jung, T. A., Mo, Y. W., and Himpsel, F. J., 1995a, *Phys. Rev. Lett.*, **74,** 1641.
Jung, T. A., Schlittler, R., Gimzewski, J. K., and Himpsel, F. J., 1995b, *Appl. Phys.* A, **61,** 467.
Jung, T. A., Schlitttler, R. R., Gimzewski, J. K., Tang, H., and Joachim, C., 1996, *Science*, **271,** 181.
Julliere, M., 1975, *Phys. Lett.* A, **54,** 225.
Kaplan, R., 1983, *J. vac. Sci. Technol.* A, **1,** 551.
Kastner, M., 1993, *Phys. Today*, January 24.
Katayama, T., Suzuki, Y., Hayashi, M., and Thiaville, A., 1993, *J. Magn. magn. Mater.*, **126,** 527.
Kawakami, R. K., Escorcia-Aparicio, E. J., and Qiu, Z. Q., 1996, *Phys. Rev. Lett.*, **77,** 2570.
Kent, A. D., Shaw, T. M., von Molnár, S., and Awshalom, D. D., 1993, *Science*, **262,** 1249.
Kern, K., Niehus, H., Schatz, A., Zeppenfeld, P., Goerge, J., and Comsa, G., 1991, *Phys. Rev. Lett.*, **67,** 855.
Ketchen, M. B., and Kirtley, J. R., 1995, *IEEE Trans. appl. Supercond.*, **5,** 2133.
Kevan, S. D., editor, 1992, *Angle-resolved Photoemission* (Amsterdam: Elsevier).
Kim, B., Andrews, A. B., Erskine, J. L., Kim, K. J., and Harmon, B. N., 1992, *Phys. Rev. Lett.*, **68,** 1931.
Kirilyuk, A., Rasing, Th., Mégy, R., and Beauvillain, P., 1996, *J. Appl. Phys.*, **79,** 5632.
Kirschner, J. M., Glöbl, M., Dose, V., and Scheidt, H., 1984, *Phys. Rev. Lett.*, **53,** 612.
Kisker, E., Schröder, A., Campagna, M., and Gudat, W., 1985, *Phys. Rev.* B, **31,** 329.
Klebanoff, L. E., Vuctora, R. H., Falicov, L. M., and Shirley, D. A., 1985, *Phys. Rev.* B, **32,** 1997.
Klots, T. D., Winter, B. J., Parks, E. K., and Riley, S. J., 1991, *J. chem. Phys.*, **95,** 8919.
Kodama, R. H., Berkowitz, A. E., McNiff, E. J., and Foner, S., 1996, *Phys. Rev. Lett.*, **77,** 394.
Kodama, R. H., Makhlouf, S. A., and Berkowitz, A. E., 1997, *Phys. Rev. Lett.*, **79,** 1393.
Koelling, D. D., 1994, *Phys. Rev.* B, **50,** 273.
Kohlhepp, J., Elmers, H. J., Cordes, S., and Gradmann, U., 1992, *Phys. Rev.* B, **45,** 12 287.
Koide, T., Shidara, T., Yamaguchi, K., Fujimori, A., Fukutani, H., Nakajima, N., Sugimoto, T., Katayama, T., and Suzuki, Y., 1996, *Phys. Rev.* B, **53,** 8219.
Körling, M., and Ergon, J., 1996, *Phys. Rev.* B, **54,** 8293.
Krams, P., Hillebrands, B., Güntherodt, G., and Oepen, H. P., 1994, *Phys. Rev.* B, **49,** 3633.

Krams, P., Lauks, F., Stamps, R. L., Hillebrands, B., and Güntherodt, G., 1992, *Phys. Rev. Lett.*, **69,** 3674.
Kryder, M. H., 1996, *Mater. Res. Soc. Bull.*, 17–60.
Kueny, A., Khan, M. R., Schuller, I. K., and Grimsditch, M., 1984, *Phys. Rev.* B, **29,** 2879.
Kunkel, R., Poelsema, B., Verheij, L. K., and Comsa, G., 1990, *Phys. Rev. Lett.*, **65,** 733.
Lagally, M., 1993, *Phys. Today*, November, 24.
Lairson, B. M., Visokay, M. R., Sinclair, R., Hagstrom, S., and Clemens, B. M., 1992, *Appl. Phys. Lett.*, **61,** 1390.
Lambeth, D. N., Velu, E. M. T., Bellesis, G. H., Lee, L. L., and Laughlin, D. E., 1996, *J. appl. Phys.*, **79,** 4496.
Landskron, H., Schmidt, G., Heinz, K., Müller, K., Stuhlmann, C., Beckers, U., Wuttig, M., and Ibach, H., 1991, *Surf. Sci.*, **256,** 115.
Lederman, M., Fredkin, D. R., O'Barr, R., Schultz, S., and Ozaki, M., 1994, *J. appl. Phys.*, **75,** 6217.
Lee, C. H., He, H., Lamelas, F., Vavra, W., Uher, C., and Clarke, R., 1989, *Phys. Rev. Lett.*, **62,** 653.
Levy, J., Nikitin, V., Cohen, A., Samarth, N., Garcia, R., and Awschalom, D., 1996, *Phys. Rev. Lett.*, **76,** 1948.
Li, D.-Q., Dowben, p., Ortega, J. E., and Himpsel, F. J., 1994a, *Phys. Rev.* B, **49,** 7734.
Li, D.-Q., Freitag, M., Pearson, J., Qiu, Z. Q., and Bader, S. D., 1994b, *Phys. Rev. Lett.*, **72,** 3112.
Li, D.-Q., Pearson, J., Bader, S. D., McIlroy, D. N., Waldfried, C., and Dowben, P., 1995a, *Phys. Rev.* B, **51,** 13 895.
Li, D.-Q., Pearson, J., Bader, S. D., Vescovo, E., Huang, D.-J., Johnson, P. D., and Heinrich, B., 1997a, *Phys. Rev. Lett.*, **78,** 1154.
Li, D.-Q., Pearson, J., Mattson, J. E., Bader, S. D., and Johnson, P. D., 1995b, *Phys. Rev.* B, **51,** 7195.
Li, J., Schneider, W.-D., and Berndt, R., 1997b, *Phys. Rev.* B, **56,** 7656.
Li, Y., and Baberschke, K., 1992, *Phys. Rev. Lett.*, **68,** 1208.
Li, C., Freeman, A. J., Jansen, H. J. F., and Fu, C. L. 1990, *Phys. Rev.* B, **42,** 5433.
Liebsch, A., 1979, *Phys. Rev. Lett.*, **43,** 1431.
Lindgren, S. Å., and Walldén, L., 1987, *Phys. Rev. Lett.*, **59,** 3003; 1988, *ibid.*, **61,** 2894.
Liou, S. H., Liu, Y., Malhotra, S. S., Yu, M., and Sellmyer, D. J., 1996, *J. appl. Phys.*, **79,** 5060.
Liu, K., Nagodawithana, K., Searson, P. C., and Chien, C. L., 1995, *Phys. Rev.* B, **51,** 381.
MacKay, J. F., Teichert, C., Savage, D. E., and Lagally, M. G., 1996, *Phys. Rev. Lett.*, **77,** 3925.
Majkrzak, C. F., Kwo, J., Hong, M., Yafet, Y., Gibbs, D., Chien, C. L., and Bohr, J., 1991, *Adv. Phys.*, **40,** 99.
Mallinson, J. C., 1987, *The Foundations of Magnetic Recording* (California: San Diego).
Mankey, G. J., Willis, R. F., and Himpsel, F. J., 1993a, *Phys. Rev.* B, **47,** 190; 1993b, *ibid.*, **48,** 10 284.
Mankey, G. J., Willis, R. F., Ortega, J. E., and Himpsel, F. J., 1994, *J. vac. Sci. Technol.*, **A12,** 2183.
Massalski, T. B., 1992, *Binary Alloy Phase Diagrams* (Metals Park, Ohio: American Society for Metals).
Mathon, J., Villeret, M., Muniz, R. B., d'Albuquerque e Castro, J., and Edwards, D. M., 1995, *Phys. Rev. Lett.*, **74,** 3696.
Matsui, S., and Mori, K., 1986, *J. vac. Sci. Technol.* B, **4,** 299.
McGuire, T. R., Krebs, J. J., and Prinz, G. A., 1984, *J. appl. Phys.*, **55,** 2505.
McWhan, D. B., 1994, *J. Synchrotron Radiat*, **1,** 83.
Mee, C. D., 1994, *The Physics of Magnetic Recording* (Amsterdam: North-Holland).
Mee, C. D., and Daniel, E. D., 1988, *Magnetic recording*, Vols. I–III (New York: McGraw-Hill).
Mermin, N. D., and Wagner, H., 1966, *Phys. Rev. Lett.*, **17,** 1133.
Meservey, R., and Tedrow, P. M., 1994, *Phys. Rep.*, **238,** 173.

Messmer, C., and Bilello, J. C., 1981, *J. appl. Phys.,* **52,** 4623.
Mezey, L. Z., and Giber, J., 1982, *Jpn. J. appl. Phys.*, **21,** 1569.
Miedema, A. R., de Châtel, P. F., and de Boer, F. R., 1980, *Physica*, **B100,** 1.
Miedema, A. R., and Dorleijn, J. W. F., 1980, *Surf. Sci.*, **95,** 447.
Miller, T., Samsavar, A., Franklin, G. E., and Chiang, T.-C., 1988, *Phys. Rev. Lett.*, **61,** 1404.
Mills, D. L., 1991, *J. Magn. magn. mater.*, **100,** 515.
Mirbt, S., Skriver, H. L., Aldén, M., and Johansson, B., 1993, *Solid St. Commun.*, **88,** 331.
Miyazaki, T., Oomori, T., Sato, F., and Ishio, S., 1994, *J. Magn. magn. Mater.*, **129,** L135.
Miyazaki, T., and Tezuka, N., 1995, *J. Magn. magn. Mater.*, **139,** L231.
Mo, Y. W., and Himpsel, F. J., 1994, *Phys. Rev.* B, **50,** 7868.
Mook, H. A., and Paul, D. McK., 1985, *Phys. Rev. Lett.*, **54,** 227.
Moodera, J. S., and Kinder, L. R., 1996, *J. appl. Phys.*, **79,** 4724.
Moodera, J. S., Kinder, L. R., Nowak, J., LeClair, P., and Merservey, R., 1996, *Appl. Phys. Lett.*, **69,** 708.
Moruzzi, V. L., Janak, J. F., and Williams, A. R., 1978, *Calculated Electronic Properties of Metals* (Oxford: Pergamon).
Moruzzi, V. L., and Marcus, P. M., 1992, *Handbook of Ferromagnetic Materials*, second edition, edited by K. Buschow (Amsterdam: Elsevier).
Moruzzi, V. L., Marcus, P. M., and Kübler, J., 1989, *Phys. Rev.* B, **39,** 6957.
Moruzzi, V. L., Marcus, P. M., Schwarz, K., and Mohn, P., 1986, *Phys. Rev.* B, **34,** 1784.
Mosdiel, A., Hyman, R. A., Zangwill, A., and Stiles, M. D., 1996, *Phys. Rev. Lett.*, **77,** 3653.
Mueller, M. A., Miller, T., and Chiang, T.-C., 1990, *Phys. Rev.* B, **41,** 5214.
Mukasa, K., Sueoka, K., Hasegawa, H., Tazuke, Y., and Hayakawa, K., 1995, *Mater. Sci. Engng*, **B31,** 69.
Mulhollan, G. A., Garrison, K., and Erskine, J. L., 1992, *Phys. Rev. Lett.*, **69,** 3240.
Müller, S., Bayer, P., Reischl, C., Heinz, K., Feldmann, B., Zillgen, H., and Wuttig, M., 1995, *Phys. Rev. Lett.*, **74,** 765.
Murray, C. B., Norris, D. J., and Bawendi, M. G., 1993, *J. Am. chem. Soc.*, **115,** 8706.
Namba, H., Nakanishi, N., Yamaguchi, T., and Kuroda, H., 1993, *Phys. Rev. Lett.*, **71,** 4027.
Néel, L., 1954, *J. Phys. Rad.,* **15,** 225.
New, R. M. H., Pease, R. F. W., and White, R. L., 1995a, *J. vac. Sci. Technol.* B, **12,** 3916; 1995b, *ibid.,* **13,** 1089.
Nguyen-Van-Dan, F., Sussian, M., Schuhl, A., and Galtier, P., 1997, *J. Appl. Phys.*, **81,** 4482
Nordström, L., Lang, P., Zeller, R., and Dederichs, P. H., 1995, *Europhys. Lett.*, **29,** 395.
Nordström, L., and Singh, D., 1996, *J. vac. Sci. Technol.* B, **14,** 3160.
Nötzel, R., Temmyo, J., and Tamamura, T., 1994, *Nature*, **369,** 131.
O'Barr, R., Yamamoto, S. Y., Schultz, S., Xu, W., and Scherer, 1997, *J. Appl. Phys.*, **81,** 4730.
O'Brien, W. L., Droubay, T., and Tonner, B. P., 1996, *Phys. Rev.* B, **54,** 9297.
O'Brien, W. L., and Tonner, B. P., 1995, *Phys. Rev.* B, **52,** 15 332.
O'Brien, W. L., Tonner, B. P., Harp, G. R., and Parkin, S. S. P., 1994, *J. appl. Phys.*, **76,** 6462.
Oepen, H. P., Berger, A., Schneider, C. M., Reul, T., and Kirschner, J., 1993, *J. Magn. Magn. Mater.*, **121,** 490.
Oepts, W., Gijs, M. A. M., Reinders, A., Jungblut, R. M., van Gansewinkel, R. M. J., and de Jonge, W. J. M., 1996, *Phys. Rev.* B, **53,** 14 024.
Ono, T., and Shinjo, T., 1995, *J. phys. Soc. Japan*, **64,** 363.
Onsager, L., 1944, *Phys. Rev.*, **65,** 117.
Orr, B. G., Jaeger, H. H., and Goldman, A. M., 1984, *Phys. Rev. Lett.*, **53,** 2046.

Ortega, J. E., and Himpsel, F. J., 1992, *Phys. Rev. Lett.*, **69,** 844; 1993, *Phys. Rev.* B, **47,** 16 441; 1994, *Appl. Phys. Lett.*, **64,** 121.
Ortega, J. E., Himpsel, F. J., Li, D.-Q., and Dowben, P. A., 1994, *Solid St. Commun.*, **91,** 807.
Ortega, J. E., Himpsel, F. J., Mankey, G. J., and Willis, R. F., 1993a, *Phys. Rev.* B, **47,** 1540; 1993b, *J. Appl. Phys.*, **73,** 5771; 1993c, *Mater. Res. Soc. Symp. Proc.*, **313,** 143.
Papaconstantopoulos, D. A., 1986, *Handbook of the Band Structure of Elemental Solids* (New York: Plenum).
Pappas, D. P., 1996, *J. vac. Sci. Technol.* B, **14,** 3203.
Parkin, S. S. P., 1991, *Phys. Rev. Lett.*, **67,** 3598; 1992, *Appl. Phys. Lett.*, **61,** 1358; 1993, *Phys. Rev. Lett.*, **71,** 1641.
Parkin, S. S. P., Chappert, C., and Herman, F., 1993, *Europhys. Lett.*, **24,** 71.
Parkin, S. S. P., Farrow, R. F. C., Marks, R. F., Cebollada, A., Harp, G. R., and Savoy, R. J., 1994a, *Phys. Rev. Lett.*, **72,** 3718; 1994b, *ibid.*, **73,** 1190.
Parkin, S. S. P., and Rabedau, T., 1996, *Appl. Phys. Lett.*, **68,** 1162.
Parkin, S. S. P., Bhadra, R., and Roche, K. P., 1991, *Phys. Rev. Lett.*, **66,** 2152.
Parkin, S. S. P., More, N., and Roche, K. P., 1990, *Phys. Rev. Lett.*, **64,** 2304.
Petrovykh, D. Y., Himpsel, F. J., and Jung, T., 1997, *Surf. Sci.* (submitted for publication).
Pettifor, D. G., 1980, *J. Magn. magn. Mater.*, **15–18,** 847.
Pfandzelter, R., Steierl, G., and Rau, C., 1995, *Phys. Rev. Lett.*, **74,** 3467.
Pierce, D. T., Scheinfein, M. R., Unguris, J., McClelland, J. J., and Celotta, R. J., 1989, *Mater. Res. Soc. Symp. Proc.*, **151,** 49.
Pippard, A. B., 1989, *Magnetoresistance in Metals* (Cambridge University Press).
Piraux, L., George, J. M., Despres, J. F., Leroy, C., Ferain, E., Legras, R., Ounadjela, K., and Fert, A., 1994, *Appl. Phys. Lett.*, **65,** 2482.
Pizzagalli, L., Freyss, M., Moraitis, G., Stoeffler, D., Demangeat, C., Dreyssé, H., Vega, A., Miethauer, S., and Bayreuther, G., 1997, *J. Appl. Phys.*, **81,** 4347.
Pizzini, S., Fontaine, A., Giorgetti, C., Dartyge, E., Bobo, J. F., Piecuch, M., and Baudelet, F., 1995, *Phys. Rev. Lett.*, **74,** 1470.
Plummer, E. W., and Eberhardt, W., 1982, *Adv. chem. Phys.*, **49,** 533.
Pratt, W. P., Jr., Lee, S.-F., Slaughter, J. M., Loloee, R., Schroeder, P. A., and Bass, J., 1991, *Phys. Rev. Lett.*, **66,** 3060.
Pratt, W. P., Jr, Lee, S.-F., Yang, Q., Holody, P., Loloee, R., Schroeder, P. A., and Bass, J., 1993, *J. appl. Phys.*, **73,** 54326.
Prinz, G. A., 1991, *J. Magn. magn. Mater.*, **100,** 469; 1995, *Phys. Today*, April, 58.
Prinz, G. A., and Hathaway, K., 1995, *Phys. Today*, April 24.
Prober, D. E., Feuer, M. D., and Giordano, N., 1980, *Appl. Phys. Lett.,* **37,** 94.
Proksch, R. B., Foss, S. F., and Dahlberg, E. D., 1994, *IEEE Trans. Magn.*, **30,** 4467.
Qiu, Z. Q., Pearson, J., and Bader, S. D., 1991, *Phys. Rev. Lett.,* **67,** 1646; 1992a, *Phys. Rev.* B, **46,** 8659.
Qiu, Z. Q., Pearson, J. Berger, A., and Bader, S. D., 1992b, *Phys. Rev. Lett.*, **68,** 1398.
Rader, O., Gudat, W., Carbone, C., Vescovo, E., Blügel, S., Kläsges, R., Eberhardt, W., Wuttig, M., Redinger, J., and Himpsel, F. J., 1997, *Phys. Rev.* B, **55,** 5404.
Rader, O., Vescovo, E., Redinger, J., Blügel, S., Carbone, C., Eberhardt, W., and Gudat, W., 1994, *Phys. Rev. Lett.*, **72,** 2247.
Rasing, Th., Groot Koerkamp, M., Koopmans, B., and van der Berg, H., 1996, *J. appl. Phys.*, **79,** 6181.
Raue, R., Hopster, H., and Clauberg, R., 1983, *Phys. Rev. Lett.*, **50,** 1623.
Rempfer, G. F., and Mauck, M. S., 1992, *Optik*, **92,** 3.
Richter, R., Gay, J. G., and Smith, J. R., *Phys. Rev. Lett.*, **54,** 2704.
Röder, H., Hahn, E., Brune, H., Bucher, J.-P., and Kern, K., 1993, *Nature*, **366,** 141.
Rosenfeld, G., Servaty, R., Teichert, C., Poelsema, B., and Comsa, G., 1993, *Phys. Rev. Lett.*, **71,** 895.
Ruckman, M. W., Joyce, J. J., and Weaver, J. H., 1986, *Phys. Rev.* B, **33,** 7029.
Rudolf, P., Sette, F., Tjeng, L. H., Meigs, G., and Chen, C. T., 1992, *J. Magn. magn. Mater.*, **109,** 109.

Runge, K., Nozaki, Y., Otani, Y., Miyajima, H., Pannetier, B., Matsuda, T., and Tonomura, A., 1996, *J. appl. Phys.*, **79,** 5075.
Samant, M. G., Stöhr, J., Parkin, S. S. P., Held, G. A., Hermsmeier, B. D., and Herman, F., 1994, *Phys. Rev. Lett.*, **72,** 1112.
Sánchez, O., García, J. M., Segovia, P., Alvarez, J., Vázquez de Parga, A. L., Ortega, J. E., Prietsch, M., and Miranda, R., 1995, *Phys. Rev.* B, **52,** 7894.
Sands, T., Palmstrom, C. J., Harbison, J. P., Keramidas, V. G., Tabatabaie, N., Cheeks, T. L., Ramesh, R., and Silberberg, Y., 1990, *Mater. Sci. Rep.*, **5,** 99.
Sano, K.-I., and Miyagawa, T., 1991, *Jpn. J. appl. phys.*, **30,** 1434.
Santoni, A., and Himpsel, F. J., 1991, *Phys. Rev.* B, **43,** 1305.
Schad, R., Potter, C. D., Belien, P., Verbanck, G., Moshchalkov, V. V., and Bruynseraede, Y., 1994, *Appl. Phys. Lett.*, **64,** 3500.
Scheinfein, M. R., Schmidt, K. E., Heim, K. R., and Hembree, G. G., 1996, *Phys. Rev. Lett.*, **76,** 1541.
Scheinfein, M. R., Unguris, J., Kelley, M. H., Pierce, D. T., and Celotta, R. J., 1990, *Rev. scient. Instrum.*, **61,** 2501; see also http://physics.nist.gov/Divisions/Div841/Gp3/epg_files/mag_recording_proj.html.
Schindler, W., Schneider, O., and Kirschner, J., 1997, *J. appl. Phys.*, **81,** 3915.
Schmailzl, P., Schmidt, K., Bayer, P., Döll, R., and Heinz, K., 1994, *Surf. Sci.*, **312,** 73.
Schmidt, F., Rave, W., and Hubert, A., 1985, *IEEE Trans. Magn.*, **21,** 1596.
Schmidt, A., and Schneider, T., 1992, *Z. Phys.* B, **87,** 265.
Schmitz-Hübsch, T., Oster, K., Radnik, J., and Wandelt, K., 1995, *Phys. Rev. Lett.*, **74,** 2595.
Schönhense, G., and Siegmann, H. C., 1993, *Ann In Phys.,* **2,** 465.
Schreyer, A., Ankner, J. F., Zeidler, Th., Zabel, H., Schäfer, M., Wolf, J. A., Grünberg, P., and Majkrzak, C. F., 1995, *Phys. Rev.* B, **52,** 16 066.
Schütz, G., Ebert, H., Fischer, P., Rüegg, S., and Zeper, W. B., 1992, *Mater. Res. Soc. Symp. Proc.*, **231,** 77.
Schütz, G., Fischer, P., Goering, E., Attenkofer, K., Alileos, D., and Rößl, W., 1997, *Synch. Rad. News*, **10,** 13.
Schulz, B., and Baberschke, K., 1994, *Phys. Rev.* B, **50,** 13 467.
Segovia, P., Michel, E. G., and Ortega, J. E., 1996, *Phys. Rev. Lett.*, **77,** 3455.
Sellmyer, D. J., Yu, M., Thomas, R. A., Liu, Y., and Kirby, R. D., 1998, *Proc. of the 10th Int. Conf. on Superlattices, Microstructures and Microdevices* (to be published).
Shinjo, T., 1991, *Surf. Sci. Rep.*, **12,** 49.
Shvets, I. V., Wiesendanger, R., Bürgler, D., Tarrach, G., Güntherodt, H.-J., and Coey, J. M. D., 1992, *J. appl. Phys.*, **71,** 5489.
Siegmann, H. C., 1992, *J. Phys. condens. Matter*, **4,** 8395.
Simonds, J. L., 1995, *Phys. Today*, April, 26.
Slater, J. C., and Koster, G. F., 1954, *Phys. Rev.*, **94,** 1498.
Slonczewski, J. C., 1993, *J. appl. Phys.*, **73,** 5957.
Smith, A. R., Chao, K.-J., Niu, Q., and Shih, C. K., 1996, *Science*, **273,** 226.
Smith, N. V., 1988a, *Phys. Rev.* B, **37,** 2874; 1988b, *Rep. Prog. Phys.*, **51,** 1227.
Smith, N. V., Brookes, N. B., Chang, Y., and Johnson, P. D., 1994, *Phys. Rev.* B, **49,** 332.
Smith, N. V., and Mattheiss, L. F., 1974, *Phys. Rev.* B, **9,** 1341.
Smith, N. V., Lässer, R., and Chiang, S., 1982, *Phys. Rev.* B, **25,** 793.
Speckmann, M., Oepen, H. P., and Ibach, H., 1995, *Phys. Rev. Lett.*, **75,** 2035.
Stauf, G. T., Driscoll, D. C., and Dowben, P. A., 1987, *Thin Solid Films*, **153,** 421.
Stearns, M. B., 1977, *J. Magn. magn. Mater.*, **5,** 167.
Steigerwald, D. A., Jacob, I., and Egelhoff, W. F., Jr, 1988, *Surf. Sci.,* **202,** 472.
Steiner, M. M., Albers, R. C., and Sham, L. J., 1992, *Phys. Rev.* B, **45,** 13 272.
Stiles, M. D., 1993, *Phys. Rev.* B, **48,** 7238; 1996, *J. appl. Phys.*, **79,** 5805.
Stöhr, J., 1995, *J. Electron Spectrosc.*, **75,** 253.
Stöhr, J., Stiles, M. D., Wu, Y., Hermsmeier, B. D., Samant, M. G., Harp, G. R., Koranda, S., Dunham, D., and Tonner, B. P., 1993, *Science*, **259,** 658.
Straub, M., Vollmer, R., and Kirschner, J., 1996, *Phys. Rev. Lett.*, **77,** 743.

Stroscio, J. A., Pierce, D. T., Davies, A., Celotta, R. J., and Weinert, M., 1995, *Phys. Rev. Lett.*, **75,** 2960.

Stroscio, J. A., Pierce, D. T., and Dragoset, R. A., 1993, *Phys. Rev. Lett.*, **70,** 3615; see also http://physics.nist.gov/Divisions/Div841/Gp3/epg_files/stm_images/5mlvstemp.gif.

Stumpf, R., and Scheffler, M., 1994, *Phys. Rev. Lett.*, **72,** 254.

Sun, J. Z., Krusin-Elbaum, L., Gupta, A., Xiao, G., Duncombe, P. R., Gallagher, W. J., and Parkin, S. S. P., 1997, *J. appl. Phys.*, **81,** 5343.

Tang, D. D., Wang, P. K., Speriosu, V. S., Le, S., and Kung, K. K., 1995, *IEEE Trans. Magn.*, **31,** 3206.

Tang, H., Weller, D., Walker, T. G., Scott, J. C., Chappert, C., Hopster, H., Pang, A. W., Dessau, D. S., and Pappas, D. P., 1993, *Phys. Rev. Lett.*, **71,** 444.

Tang, Z. X., Sorensen, C. M., Klabunde, K. J., and Hadjipanayis, 1991, *Phys. Rev. Lett.*, **67,** 3602.

Tersoff, J., Denier van der Gon, A. W., and Tromp, R. M., 1994, *Phys. Rev. Lett.*, **72,** 266.

Tersoff, J., Teichert, C., and Lagally, M. G., 1996, *Phys. Rev. Lett.*, **76,** 1675.

Thomas, R. E., 1970, *J. appl. Phys.*, **41,** 5330.

Thompson, D. A., Romankin, L. T., and Mayadas, A. F., 1975, *IEEE Trans. Magn.*, **11,** 1039.

Tober, E. D., Ynzunza, R. X., Westphal, C., and Fadley, C. S., 1996, *Phys. Rev.* B, **53,** 5444.

Tomaz, M. A., Ingram, D. C., Harp, G. R., Lederman, D., Mayo, E., and O'Brien, W. L., 1997a, *Phys. Rev.* B, **56,** 5474; 1997b, *J. vac. Sci. Technol.* (to be published).

Trouilloud, P. L., Petek, B., and Argyle, B. E., 1994, *IEEE Trans. Magn.*, **30,** 4494.

Tsang, C., Fontana, R. E., Lin, T., Heim, D. E., Speriosu, V. S., Gurney, B. A., and Williams, M. L., 1994, *IEEE Trans. Magn.*, **30,** 3801.

Turek, I., Becker, Ch., and Hafner, J., 1992, *J. Phys.: condens. Matter*, **4,** 7257.

Turner, A. M., Donoho, A. W., and Erskine, J. L., 1984, *Phys. Rev.* B, **29,** 2986.

Turtur, C., and Bayreuther, G., 1994, *Phys. Rev. Lett.*, **72,** 1557.

Tyson, W. R., and Miller, W. A., 1977, *Surf. Sci.*, **62,** 267.

Uhl, M., and Kübler, J., 1996, *Phys. Rev. Lett.*, **77,** 334.

Unguris, J., Celotta, R. J., and Pierce, D. T., 1991, *Phys. Rev. Lett.*, **67,** 140.

Valet, T., and Fert, A., 1993, *Phys. Rev.* B, **48,** 7099.

Van der Veen, J. F., Eastman, D. E., Bradshaw, A. M., and Holloway, S., 1981, *Solid St. Commun.*, **39,** 1301.

van der Vegt, H. A., van Pinxteren, H. M., Lohmeier, M., and Vlieg, E., 1992, *Phys. Rev. Lett.*, **68,** 3335.

Van Leeuwen, D. A., van Ruitenbeek, J. M., de Jongh, L. J., Ceriotti, A., Pcchioni, G., Häberlen, O. D., and Rösch, N., 1994, *Phys. Rev. Lett.*, **73,** 1432.

van Schilfgaarde, M., and Harrison, W. A., 1993, *Phys. Rev. Lett.*, **71,** 3870.

Vázquez de Parga, A. L., and Alvarado, S. F., 1994, *Phys. Rev. Lett.*, **72,** 3726.

Viernow, J., Lin, J.-L., Petrovykh, D. Y., Leibsle, F. M., Meu, F. K., and Himpsel, F. J., 1998, *Appl. Phys. Lett.* (submitted for publication).

Von Barth, U., and Hedin, L., 1972, *J. Phys.* C, **5,** 1629.

Wagner, H., 1979, *Physical and Chemical Properties of Stepped Surfaces*, Springer tracts in Modern Physics, Vol. 85 (Berlin: Springer), p. 151.

Wang, D.-S., Wu, R., and Freeman, A. J., 1994, *J. Magn. magn. Mater.*, **129,** 237.

Wang, L.-S., Wu, H., and Desai, S. R., 1996a, *Phys. Rev. Lett.*, **76,** 4853.

Wang, X. Y., Shen, X. J., Osgood, R. M., Haight, R., and Himpsel, F. J., 1996b, *Phys. Rev.* B, **53,** 15 738.

Weaver, J. H., 1986, *Phys. Today*, January, 24.

Weber, W., Back, C. H., Ramsperger, U., Vaterlaus, A., and Allenspach, R., 1995, *Phys. Rev.* B, **52,** 14 400.

Weber, W., Bischof, A., Allenspach, R., Würsch, Ch., Back, C. H., and Pescia, D., 1996, *Phys. Rev. Lett.*, **76,** 3424.

Weber, W., Kerkmann, D., Pescia, D., Wesner, D. A., and Güntherodt, G., 1990, *Phys. Rev. Lett.*, **65,** 2058.

Weber, W., Wesner, D. A., Hartmann, D., and Güntherodt, G., 1992, *Phys. Rev.* B, **46,** 6199.
Weinert, M., Hulbert, S. L., and Johnson, P. D., 1985, *Phys. Rev. Lett.*, **55,** 2055.
Weisbuch, C., and Vinter, B., 1991, *Quantum Semiconductor Structures* (San Diego, California: Academic Press).
Welipitiya, D., He, Y. L., Zhang, J., Oden, P. I., Thundat, T., Warmack, R. J., Gobulukoglu, I., Shan, S. Z., Sellmyer, D. J., and Dowben, P. A., 1996, *J. appl. Phys.*, **80,** 1867.
Weller, D., Alvarado, S. F., Gudat, W., Schröder, K., and Campagna, M., 1995, *Phys. Rev. Lett.*, **54,** 1555.
Wernsdorfer, W., Doudin, B., Mailly, D., Hasselbach, K., Benoit, A., Meier, J. Ansermet, J.-Ph., and Barbara, B., 1996, *Phys. Rev. Lett.*, **77**, 1873.
White, R. M., 1984, *Introduction to Magnetic Recording* (New York: IEEE).
Wiesendanger, R., Bode, M., Kleiber, M., Löhndorf, M., Pascal, R., Wadas, A., and Weiss, D., 1997, *J. Vac. Sci. Technol.* B, **15,** 1330.
Wiesendanger, R., and Güntherodt, H.-J., 1990, *Phys. Rev. Lett.*, **65,** 247.
Wiesendanger, R., Güntherodt, H.-J., Güntherodt, G., Gambino, R. J., and Ruf, R., 1990, *Phys. Rev. Lett.*, **65,** 247.
Wu, R., and Freeman, A. J., 1966, *J. appl. Phys.*, **79,** 6500.
Wu, R., Wang, D., and Freeman, A. J., 1994a, *J. appl. Phys.*, **75,** 5802.
Wu, S. C., Garrison, K., Begley, A. M., Jona, F., and Johnson, P. D., 1994b, *Phys. Rev.* B, **49,** 14 081.
Wu, S. Z., Schumann, F. O., Mankey, G. J., and Willis, R. F., 1996, *J. vac. Sci. Technol.*, **14,** 3189.
Würsch, Gh., Stamm, Ch., Egger, S., and Pescia, D., 1997 (to be published).
Wulfhekel, W., Knappmann, S., Gehring, B., and Oepen, H. P., 1994, *Phys. Rev.* B, **50,** 16 074.
Wuttig, M., Feldmann, B., Thomassen, J., May, F., Zillgen, H. Brodde, A., Hannemann, H., and Neddermeyer, H., 1993a, *Surf. Sci.*, **291,** 14.
Wuttig, M., Gauthier, Y., and Blügel, S., 1993b, *Phys. Rev. Lett.*, **70,** 3619.
Xiao, J. Q., Jiang, J. S., and Chien, C. L., 1992, *Phys. Rev. Lett.*, **68,** 3749.
Yang, C. Y., Johnson, K. H., Salahub, D. R., Kaspar, J., and Messmer, R. P., 1981, *Phys. Rev.* B, **24,** 5673.
Yeh, J. J., and Lindau, I., 1985, *At. Data nucl. Data Tables*, **32,** 1.
Zaera, F., 1991, *Surf. Sci.*, **255,** 280.
Zhang, Z., Hammel, P. C., and Wigen, P. E., 1996, *Appl. Phys. Lett.*, **68,** 2005.
Zhu, M. J., Bylander, D. M., and Kleinman, L., 1991, *Phys. Rev.* B, **43,** 4007.
Zhu, Q.-G., Yang, Y., Williams, E. D., and Park, R. L., 1987, *Phys. Rev. Lett.*, **59,** 835.